Observation of laminar-turbulent transition of a yield stress fluid in Hagen-Poiseuille flow

by

Bülent Güzel

B.A.Sc., Yildiz Technical University, 1995
M.A.Sc., Istanbul Technical University, 1997

A THESIS SUBMITTED IN PARTIAL FULFILMENT OF
THE REQUIREMENTS FOR THE DEGREE OF

Doctor of Philosophy

in

The Faculty of Graduate Studies

(Mechanical Engineering)

The University Of British Columbia

(Vancouver)

February, 2009

Abstract

The main focus of this work is to investigate experimentally the transition to turbulence of a yield stress shear thinning fluid in Hagen-Poiseuille flow. By combining direct high speed imaging of the flow structures with Laser Doppler Velocimetry (LDV), we provide a systematic description of the different flow regimes from laminar to fully turbulent. Each flow regime is characterized by measurements of the radial velocity, velocity fluctuations, and turbulence intensity profiles. In addition we estimate the autocorrelation, the probability distribution, and the structure functions in an attempt to further characterize transition. For all cases tested, our results indicate that transition occurs only when the Reynolds stresses of the flow equals or exceeds the yield stress of the fluid, i.e. the plug is broken before transition commences. Once in transition and when turbulent, the behavior of the yield stress fluid is somewhat similar to a (simpler) shear thinning fluid. We have also observed the shape of slugs during transition and find that their leading edges to be highly elongated and located off the central axis of the pipe, for the non-Newtonian fluids examined. Finally we present a new phenomenological approach for quantifying laminar-turbulent transition in pipe flow. This criterion is based on averaging a local Reynolds number to give Re_G. Our localised parameter shows strong radial variations that are maximal at approximately the radial positions where puffs first appear during the first stages of turbulent transition.

Table of Contents

Appendices

List of Tables

List of Figures

Acknowledgements

This work could not have been done without the support of many people. I would like to first express my appreciation to my supervisors Dr. Ian Frigaard and Dr. Mark Martinez for all their support, encouragement and guidance throughout this research. A special thanks to Teodor Burghelea and my other colleagues in the fluids lab. I would also like to thank Chérif Nouar for numerous fruitful discussions during visits both in Nancy & Vancouver during the course of this work. The financial support of the Natural Sciences and Engineering Research Council of Canada (NSERC) is gratefully acknowledged as is that of the Canada Foundation for Innovation, New Opportunities Programme.

Chapter 1

Introduction

The focus of this experimental study is an investigation of the transition to turbulence of a yield stress shear thinning fluid in Hagen-Poiseuille flow. The present work was motivated by both oil & gas and pulp & paper applications where control of the inherent processes requires knowledge of the flow state at different velocities. The fluids used in this study are (i) Newtonian (ii) shear thinning and (iii) shear thinning with a yield stress τ_y. With yield-stress fluids the axial profile in fully developed laminar flow is characterized by an un-yielded or plug zone. The radius of the plug zone is dictated by a balance between the frictional pressure drop and the yield stress of the fluid. One of the remaining open scientific questions with these fluids is the role of the plug during transition.

There is a demand from industrial applications to predict the Reynolds number Re ($Re = U_b D/\nu$ where U_b is the average or bulk velocity, D is the diameter of the pipe and ν is the kinematic viscosity) at which transition occurs, for a range of fluid types, so that different frictional pressure closures may be applied to piping network design calculations. One of the earliest attempts, and probably still the most popular for non-Newtonian fluids is that of Metzner and Reed. Perhaps the most obvious weakness with such phenomenological formulae is that turbulent transition occurs over a wide range of Reynolds numbers and not at a single number. For example in careful experiments Hof *et al.* [65] report retaining laminar flows in Newtonian fluids up to Re=24,000, whereas the common observation of transition initiating in pipe flows is at Re 2000. Thus, there is a difficulty with interpreting the predictions of phenomenological formulae, many of which were formulated before a detailed understanding of transitional phenomena has developed. Although such a predictive guideline is a worthy goal, and one

we address in this thesis, it is clear that a necessary process to this is a detailed study of transition, which we provide here.

The main objective of this work is to help elucidate the mechanism of transition from laminar to turbulent flow in shear thinning yield stress fluids. The work is experimental in which we characterize the flow state using high-speed imaging and by measuring the mean and fluctuating components of velocity using laser Doppler velocimetry. Here we measure the velocity profiles across the diameter of the pipe from slow to fully turbulent flows. In § 1.1, the pertinent literature is reviewed in which we consider the major works outlining transition in both Newtonian and non-Newtonian fluids and summarize the empirical correlations used to predict transition. In § 1.2, a brief summary of the literature is given and the objectives of the thesis are outlined. The experimental flow loop and the flow visualization system used are presented in § 2. In § 3, we present the results in two sections. In the first section we describe phenomenologically the behaviour of the fluids undergoing transition. In this subsection we characterize the flow field both using high speed video images and simple measurements of the fluctuations of the instantaneous velocity measurements. In the next section, the transition to turbulence using higher-order statistical methods is characterized. In § 4, we present a new definition of Re and demonstrate that transition occurs at a common Re for all fluids tested.

1.1 Literature review

Since Reynolds' experiment in 1883, Reynolds [112], a large number of experimental and theoretical studies have been conducted to characterize transition, but the mechanism of turbulence transition is still not fully understood. White [142] stated that "There is no theory of transition. After a century of research on the transition process,..., the mechanisms are still not completely understood.... A dramatic example of our limited knowledge is the fact that the original transition experiment (pipe flow) is still not well understood." The published studies can be divided into three main groups for transition to turbulent in pipe flows. The first one deals with

experimental activities. The second group includes the theoretical activities that aim to provide physical models for prediction of a critical threshold. The last group contains numerical investigations, mainly by using Reynolds-averaged Navier-Stokes solvers. But first, we review the early research on turbulence, then detail on the literature of transition.

1.1.1 Mixing length theory

Transition to turbulence may be explained with growth rates and instability amplification rates from basic linear stability theory, including nonlinear effects. But studying the developing instability and transition to turbulence is found to be more difficult than investigating turbulence as a state by many researchers. Turbulence is studied in two main trends (Roshko [113]). The first one is the search for models of the Reynolds Averaged Navier-Stokes (RANS) equations first derived by Reynolds, which address the mean-flow quantities. It is known that the turbulent flow is described by the unsteady form of the Navier-Stokes equations. And the second one is called statistical theory of turbulence first introduced by G. I. Taylor in 1930's, which seeks statistical descriptions of the turbulence itself, mainly through equations and relations for correlations of the velocity fluctuations. The most common one is Kolmogorov's concept of a 'universal inertial range' for a limited range of the correlations at small scales. He uses scaling and similarity arguments and introduces the 'fundamental' Kolmogorov constant.

In turbulent flow, we can define an effective viscosity as the sum of the molecular viscosity, μ and a turbulent viscosity, μ_t. The turbulent viscosity accounts for momentum transport by eddies. In need determining the turbulent viscosity, a model of turbulent transport is required. The first one was Prandtl's mixing length hypothesis. The theory of the mixing length was first introduced, taking analogy from the mean free-path of the gas theory by Prandtl [108]. Then several theories have been proposed by Taylor [131] and von Karman [73] for obtaining theoretically the mean velocity profile of turbulent pipe and channel flows. It has been used in turbulent modeling especially for external flows to obtain the closure equations of turbulence.

For turbulent pipe flows, mixing length theory led to the logarithmic law in the wall region. It is now known that instability waves, and resulting coherent structures, are dominant features of mixing layers in transition and in the fully developed turbulence.

Using the Boussinesq laminar flow analogy, the kinematic turbulent viscosity (also called eddy viscosity), ν_t can be expressed as the product of a velocity scale and a length scale. If the velocity scale is assumed to be proportional to the length scale and the velocity gradient, Prandtl's (1925) mixing length model is derived as $\nu_t = {l_m}^2|du/dy|$. Algebraic expressions are derived for the mixing length for internal and external flows. Mixing length model is also used to describe the Reynolds stresses by means of simple algebraic formulae for turbulent viscosity, μ_t. So Reynolds stresses are linked to the mean rate of deformation.

$$\tau_{ij} = -\rho\overline{u_i' u_j'} = \mu_t\left(\frac{dU_i}{dx_j} + \frac{dU_j}{dx_i}\right) \tag{1.1}$$

The turbulent viscosity (also called the Eddy viscosity), μ_t has the same unit as that of the molecular viscosity and is assumed to be isotropic. Most of the kinetic energy of turbulence is contained in the largest eddies and the turbulence length scale l is therefore characteristic of these eddies which interact with the mean flow. Therefore, mixing length theory links the characteristic velocity scale of the eddies with the mean flow properties. The turbulent viscosity is used to close the momentum equations in turbulent modeling. Hornby *et al.* [69] used Prandtl's concept, together with modifications such as that proposed by van Driest [35], and extended to obtain the wall damping factor in flow in a duct of constant cross section by considering the oscillation of the whole of the boundary. Van Driest (1951) proposed a damping function to slow down the growth of the turbulent stress in the vicinity of the wall. Hornby *et al.* [69] considered the damping influence of the whole of the boundary of the flow cross section and not just that of the near wall region for plane parallel flow and axisymmetric flow in a pipe and in an annulus.

On the base of Prandtl's postulate that the total shear stress in a turbu-

lent Newtonian fluid could be written as the sum of the laminar molecular shear and the turbulent shear stress contribution, Clapp [22] modified it to include non-Newtonian effects. Hecht [63] investigated the velocity profiles for non-Newtonian power law fluids and determined the friction factor for pipe flow at high Reynolds numbers. As in Newtonian case, the total shear stress is equated to the sum of the laminar power law stress and the turbulent stress based on the Prandtl mixing length as a function of power law index n. He used van Driests' model for variation of the mixing length near the wall to yield a continuous velocity and shear stress distribution for turbulent pipe flow. He found agreement with experiments if the proper values of power law index and mixing length parameter are used.

Modeling transition to turbulence with mixing length theory can be used for external flows. Transition is characterized with its starting and ending value of Reynolds numbers based on effective viscosity; it assumed to be started when the friction losses becomes larger than its laminar value for the same Reynolds number and ended when the friction is smaller than its turbulent value for the same Reynolds number. There are different types of mixing-length transition models. For the intermittency-based transition model, turbulent viscosity is computed, multiplied by the intermittency factor, and added to the laminar viscosity according to the turbulence intensity and pressure gradient. The formulation of the intermittency model in the Prandtl mixing length model is $\mu_t = \rho\gamma l^2|du/dy|$, $\nu_t = \gamma l^2|du/dy|$ where γ is the intermittency function. The most widely used intermittency models are developed by Abu-Ghannam & Shah [2] and Mayle [86]. The theory is based on that as the flow increased, the turbulent viscosity becomes significant, increasing the value of friction loss from a laminar value to a turbulent one. Crawford & Kays [23] modified van Driest transition model; the van Driest damping function constant in the mixing length is controlled to simulate how the sublayer thickness decreases as the flow moves from laminar state to turbulent state.

In Prandtl's mixing length model, it is assumed that the shear stress is constant and equal to the wall value (τ_w) and further that the viscous contribution was negligible. So it only calculates mean flow properties and

turbulent shear stress. None of the previous mixing-length or eddy-viscosity approaches takes into account the Reynolds-number dependency of the parameters of the mean velocity profiles (Buschmann & Gad-el-Hak [19]). And today this theory is ignored because it has too many assumptions and much better models are available.

1.1.2 Studies on Newtonian transition

Experimental studies

Understanding transition flow in yield stress fluids is difficult. Insight into this phenomena can be gained by first examining the simpler case of Hagen-Poiseuille flow with a Newtonian fluid. In laminar flow, fluid particles follow straight lines that are parallel to each other called streamlines. In turbulent flow different sizes of eddies are superimposed on the streamlines. Larger eddies carry the fluid particles across the streamlines and smaller eddies create stirring that causes diffusion. The onset of turbulence is not immediate. There is a process of instability that makes laminar flow a turbulent one. In this transitional zone, flow is neither laminar nor fully turbulent, and in which the observed pressure drops are intermediate between those for laminar and turbulent flow.

The detail of Newtonian transition is still under investigation. From the engineering perspective, it is generally accepted that transition can be predicted using one dimensionless parameter, the Reynolds number $Re = U_b D/\nu$ where U_b is the average velocity, D is the diameter of the pipe and ν is the kinematic viscosity. When the Re exceeds a critical value, even small disturbances, which always exist in a physical system, can cause instability and transition. From a mathematical perspective, although Hydrodynamic Stability Theory, Schmid *et al.* [121] is capable of predicting instability of some flow configurations (transient growth or amplification of small disturbances), it is unable to predict transition (i.e. a critical Reynolds number) for pipe flows because the flow is stable at all Reynolds numbers. So nonlinear analysis is a must to be able to have a predictive mechanism from mathematical analysis. Hydrodynamic Stability Theory will be discussed in

detail in next section. For a Newtonian fluid it is known that the Reynolds number above 2100 is generally accepted as the critical value of practical interest to transition.

There are a number of means to characterize the onset of transition. In the simplest case, the relation between pressure drop and velocity is also used to identify the flow regimes. The change from the laminar to the turbulent flow regime results in a large increase in the flow resistance. The functional relationships and physical flow patterns are fundamentally different for the two regimes. The Fanning friction factor; i.e. White [143], f, can be derived exactly for laminar flow and empirically for turbulent flow. The value of f in laminar pipe flows for Newtonian fluids is $f = \frac{64}{Re}$. Measuring the friction factor's departure from $64/Re$ is an effective way to detect the transition. In addition to this, characterization of the point of transition in experiments can also be based on the statistics of the flow properties, mainly velocity and pressure, because the motion of turbulent eddies, which are random cause fluctuation (e.g. $u(t) = \overline{u} + u'(t)$). Here, the root-mean-square (rms) of local velocity

$$u_{rms} = \sqrt{\overline{u'^2}} \tag{1.2}$$

is calculated to measure turbulence strength and

$$I = \frac{u_{rms}}{\overline{u}} \tag{1.3}$$

for turbulence intensity I. The observation of the velocity and the turbulence intensity at the centerline is a generally accepted method to detect transition for Newtonian fluids.

In addition there is a significant body of experimental work that has focused at flow structure in intermediate transitional regimes for Newtonian fluids. Wygnanski and coworkers (Wygnanski & Champagne [149], Wygnanski *et al.* [150]) found that flow disturbances evolve into two different turbulent states during transition: puffs and slugs. They observed and described the evolution of localized turbulent puffs and slugs in details such as their shape, the way they propagate, their velocity profiles and the turbulence intensities inside them. The puff is found when the Reynolds number is

	U_ℓ/U_b	U_t/U_b	Re	Structure
Wygnanski & Champagne [149]	0.92	0.86	2200	puff
Wygnanski & Champagne [149]	1.55	0.62	8000	slug
Teitgen [133]	1.40	0.73	2200	puff
Draad [31]	1.70	0.60	5800	slug
Shan *et al.* [124]	1.56	0.73	2200	puff
Shan *et al.* [124]	1.69	0.52	5000	slug
Mellibovsky & Meseguer [88]	1.57	0.68	3850	slug

Table 1.1: Reported literature values of the leading and trailing edge velocities of a puff or a slug in a flowing Newtonian fluid.

below $Re \sim 2700$ and the slug appears when the Reynolds number is above $Re \sim 3000$. Both the puff and slug are characterized by a change in the local velocity in which the flow conditions are essentially laminar outside the structure and turbulent inside. The puff and slug are distinguished from each other by the abruptness of the initial change between the laminar and turbulent states. It has been reported that for a puff, the velocity trace is saw-toothed whilst a slug has a square form on velocity-time readings. Since these classical studies, many authors have observed and measured puff and slug characteristics in Newtonian fluids. A summary of reported values of the leading U_ℓ and trailing U_t edge velocities of puffs and slugs are given in Table 1.1, scaled by the mean flow velocity U_b.

Further attempts to characterize transition experimentally include the studies of Bandyopadhyay [8], Toonder & Nieuwstadt [135], Eliahou *et al.* [37], Han *et al.* [55] & Hof *et al.* [65]. Bandyopadhyay [8], reports streamwise vortex patterns near the trailing edge of puffs and slugs. Darbyshire & Mullin [25], indicates that a critical amplitude of the disturbance is required to initiate transition and this value decreases with Re. Toonder & Nieuwstadt [135] performed LDV profile measurements of a turbulent pipe flow with water. They found that the u_{rms} near the wall is independent of Reynolds number. Eliahou *et al.* [37] investigated experimentally tran-

sitional pipe flow by introducing periodic perturbations from the wall and concluded that amplitude threshold is sensitive to disturbance's azimuthal structure. Han *et al.* [55] expanded on the work of Eliahou *et al.* [37] and advanced the argument that transition is related to the azimuthal distribution of the streamwise velocity disturbances and that transition starts with the appearance of spikes in the temporal traces of the velocity. In addition they found that there is a self-sustaining mechanism responsible for high-amplitude streaks and indicate that spikes not only propagate downstream but also propagate across the flow, approaching the pipe axis. Hof *et al.* [66] measured the velocity fields instantaneously over a cross-sectional slice of a puff and showed that uniformly distributed streaks exist around the pipe wall and slower streaks exist near the centreline in a puff. They show that the minimum amplitude of a perturbation required to cause transition scales as the inverse of the Reynolds number. There are of course many other experimental studies of Newtonian fluid transition.

Kanda & Yanagiya [75] repeated the Reynold's experiments and critical Reynolds number values obtained by previous researchers are summarized, focusing on bellmouth entrances and a straight pipe. It is seen that the critical Reynolds number value is of about 2030 when using a straight pipe and that with bellmouth entrances, it increases from 2030 to 12,000 and higher. They did their experiments with ten exchangeable pipe entrances; namely, a straight pipe, five different quadrant-arc rounds and four different bellmouth entrances. They observed that the transition occurs after the parabolic velocity profile becomes artificially distorted. Then, puffs and slugs are generated by the disturbances in the fully developed region. They stressed that the transition from laminar to turbulent flow occurs necessarily in the entrance region and concluded that an apparent cause of the transition is the contraction ratio of pipe entrances, particularly that of the small quadrant-arc rounds cut at the pipe inlet. And Reynolds' value of 2030 could be reproduced by a method similar to Reynolds' color-band method when using a straight pipe.

Theoretical studies

The gap between experimental and theoretical understanding of Newtonian shear transition is drawing ever closer. The mid-1990's saw a revival of interest in linear theories with the realisation that stable linear modes could undergo prolonged periods of (algebraic) growth before an eventual decay, and that these slowly varying solutions may themselves be unstable. Whilst early work looked for exact resonances, it was later appreciated that due to non-normality of the linearised Navier-Stokes operator, transient growth could occur for specific initial conditions without exact resonance; see Chapman [20], Reddy *et al.* [109], Trefethen *et al.* [136] for an overview of these developments. At the same time, self sustaining mechanisms were proposed by Waleffe and others, (Hamilton *et al.* [54], Waleffe [140]), by which energy from the mean flow could be fed back into streamwise vortices, thus resisting viscous decay. Self-sustained exact unstable solutions to the Navier-Stokes equations were found by Faisst & Eckhardt [44] and by Wedin & Kerswell [141]. Much current effort is focused at understanding the link between these self-sustained unstable solutions and observed transitional phenomena, such as intermittency, streaks, puffs and slugs; see e.g. Eckhardt *et al.* [38], Hof *et al.* [66, 67], Kerswell & Tutty [78].

Studying the regions of stability and instability and knowing which parameters will influence the behavior of the system give a theoretical perspective to understand the onset of instability and transition to turbulence for pipe flows.

Hydrodynamic stability theory

Hydrodynamic stability theory is concerned with the response of a laminar flow to a disturbance of small or moderate amplitude. Basically, if the flow returns to its original laminar state, we define the flow as stable, whereas, if the disturbance grows and causes the laminar flow to change into a different state, we define the flow as unstable. Instabilities often result in turbulent fluid motion. Stability theory deals with the mathematical analysis of the evolution of disturbances superposed on a laminar base flow.

The linear stability theory, based on the amplification of infinitesimally small perturbations, has wide range of applications in different fluid mechanics configurations. The idea is based on the assumption that the actual flow consists in the superposition of the considered basic flow, i.e. $U = U_b + u$, $P = P_b + p$, with $U_b(r,t)$ and $P_b(r,t)$ the velocity field and the pressure of the basic flow, respectively, and u and p the perturbation of the velocity and pressure, respectively. Although the Navier-Stokes equations are nonlinear, the amplitudes of u and p are assumed to be very small in comparison with the ones of the basic flow, which allows us to treat the system linearly by neglecting all nonlinear terms in u and p. A harmonic perturbation is introduced into the linearized Navier-Stokes equations leading to an eigenvalue problem posed as a system of partial differential equations with respect to the spatial coordinates. If not only the zero perturbation is a solution, but also a nonzero solution exists, it is referred to an eigenmode. If the nonzero solution increases with respect to time, the basic flow is said to be linearly unstable whereas if it decreases, the basic flow is said to be linearly stable. Only some of the eigenmodes depending on frequencies and wavelengths of the perturbation are amplified. Then, the mathematical form of the perturbation can be prescribed with the mean flow velocity acting as a coefficient.

The linear theory often assumes that the mean flow is quasiparallel. The eigenmodes predict long-term rather than short-term behaviour. The results of the eigenmodes (eigenvalues and eigenfunctions) depend only the Reynolds number and for large x values. Thus, Re is a constant and the whole set of eigenvalues, called a spectrum, is fixed. Trefethen *et al.* [136] summarized much of the work in this area, and stated that the classical analysis works only for flows subject to specific destabilizing forces such as Rayleigh-Benard convection and Taylor and Gortler vortices. But there is a poor agreement between theory and experiment for flows when the instability mechanism is viscous such as in pipe flows. Although a linear equation governing the evolution of disturbances is desirable, as the disturbance velocities grow above a few percent of the base flow, nonlinear effects become important and the linear equations no longer accurately predict the disturbance evolution. When taking into account the nonparallel effects on the

perturbation form leads to inconsistent results compared to the linear approach. Pipe flow is linearly stable at all Reynolds numbers by eigenvalue analysis (Drazin & Reid [34], Schmid & Henningson [120], Trefethen *et al.* [136]). Boberg & Brosa [15] showed that nonlinear studies confirm the nonlinear and three-dimensional nature of transition in pipe flow.

The non-linear effects that drive the transition process may be induced through a transient growth without involving any linear instability (Schmid & Henningson [120]). Although the linear equations have a limited region of validity, they are important in detecting physical growth mechanisms and identifying dominant disturbance types. In practice, pipe flows are unstable to small finite perturbation. Finite perturbations might come from the algebraic growth of an exponentially decaying linear stability. [The form of a linear perturbation as a function of space and time is satisfied by an exponential solution:

$$\Psi = \Psi_0 e^{i(\omega t - kx)} \tag{1.4}$$

which is used as an indication of that the flow is stable or not.] In Eq. (1.4), Ψ stands either for the pressure p or the velocity u. Ψ_0 is the amplitude of the original perturbation, k is the complex wave number, and ω is the complex frequency. The growth rate of the perturbation is given by the negative imaginary part of the complex frequency. Then the rate of growth is determined by plotting the amplitude of the disturbance as it propagates into the pipe, against time.

Transient growth is a linear process that relies on the non-orthogonality between modes resulting in a growth of disturbance energy even when all modes decay. So this transient growth mechanism may be used to explain transition because experimentally, the energy of perturbation experiences substantial growth. In practical applications where the initial disturbance amplitudes are large enough, the transient growth can reach the level necessary to trigger non-linear effects. This is a new theory/perspective developed in late 1980's, e.g. Bamieh & Dahleh [7], Boberg & Brosa [15], Mellibovsky & Meseguer [87], Schmid *et al.* [121], Trefethen *et al.* [136, 137] & others.

These studies showed that the effect of transient growth which plays a

major role in the stability of classical pipe flow may explain the mechanism of transition. Trefethen *et al.* [136] used two basic numerical techniques for linear transient analysis. The first one uses the classical eigenmodes to calculate an explicit transient pseudo-mode. A flow perturbation, capable of significant transient growth, at time $t = 0$ is the pseudo-mode. Then this pseudo-mode typically attains an amplification factor G_{max} proportional to the Reynolds number, before decaying exponentially as $t \to \infty$. The second technique uses the pseudo-spectrum of the linear system, not the eigenspectrum. Physically; the pseudo-spectrum indicates the transient response of the system to an arbitrary continuous-time perturbation signal.

Drazin & Reid [34] and Schmid & Henningson [120] determined the critical Reynolds number as the maximum Reynolds number at which the disturbance energy in the system monotonically decreases. But this critical Reynolds number is much lower than that by experiments. In practice, it is well known for pipe flows that the transition from laminar to turbulent is not immediate and it first starts somewhere in the entry region and then spreads out and propagates from this position. So the starting point and the mechanism of transition and the critical Reynolds number in pipe flows are still the questions to be answered.

As numerical solutions to the governing Navier-Stokes equations, traveling waves has been studied by Wedin & Kerswell [141]. They found that around r/R=0.6 is the critical location for transition in Newtonian pipe flows. They also suggested that this corresponds to where the fast streaks of traveling waves reach from the wall. The solution of traveling waves has been confirmed by Hof *et al.* [66] in their experiments.

Computational studies

Analysis of transition by means of theoretical methods still needs more work to characterize the onset of turbulence and intermittency, therefore some researchers turn to simulation methods as an alternative approach to study transition. Large eddy simulations (LES) and direct numerical simulations (DNS) methods are generally used to solve the Navier-Stokes equations for

pipe flows, although in LES the smallest scales are modeled, whereas in a DNS all scales are resolved and no turbulence modeling is applied.

Shan *et al.* [123] studied a DNS of transition from laminar to turbulent flow excited by wall disturbances in a cylindrical pipe. The wall disturbances are imposed by means of blowing and suction through the pipe wall with two different cases; periodic suction/blowing (PSB) and random suction/blowing (RSB). They investigated the dependence of the transition time on the suction/blowing amplitudes and the Reynolds number. For the case of PSB the pipe flow appears to remain stable for an axisymmetric distribution of the disturbance even for large amplitude of the blowing/suction, whereas, unstable for a non-axisymmetric distribution of blowing/suction. The critical value of the amplitude decreases with increasing Reynolds number. The results for the RSB resemble those obtained for the non-axisymmetric PSB except that the disturbance seems to develop more quickly.

Later Shan *et al.* [124] performed a direct numerical simulation of a puff and a slug structure in a transitional pipe flow by using a spectral element method. The puff or slug structure is triggered by imposing a localized velocity disturbance on the flow for a small period of time. After this excitation the disturbance is transported downstream and develops into either a puff or slug. They concluded that the leading edge and trailing edge of both a puff and a slug travel with a constant velocity equal to the bulk velocity. They found that the turbulence within the slug is quite close to the structure of a fully developed turbulent pipe flow and the influence of the initial disturbance can be neglected for the development of puffs and slugs. They also found that the growth of the disturbance energy decreases with decreasing Reynolds number and it decays after having reached a maximum value when Reynolds number smaller than the value of 2200. By looking at the structures of puffs and slugs they found that the slug seems to travel at a speed close to the bulk velocity concluding that a slug is a material property of the flow. On the other hand, a puff travels more wave-like fashion. They conclude that helical particle motions exist in the trailing-edge region. Other DNS work on developing puffs and slugs in transitional flows are done by Nikitin [93], Priymak & Miyazaki [107] and Reuter & Rempfer [111].

Obtaining the critical Reynolds number using stability theory or computational methods has been objective of transitional research (Ben-Dov & Cohen [10]). Using the effect of the radial pressure gradient, Kanda [74] developed a macro model which provides a minimum critical Reynolds number for laminar-turbulent transition in pipe flows on the basis of the results of their experiments. His calculated critical Reynolds number is 2200 when the number of radial grid points is 101. In the entrance region, the velocity profile changes from a uniform distribution at the pipe inlet to a parabolic one in the fully developed region. His model is based on the normal wall strength ($-\partial p/\partial dr$ at r=R). This normal wall strength causes the difference in the radial direction and accelerates fluid particles in the central core. The occurrence of the transition depends on the acceleration power. The magnitude of the required non-dimensional acceleration power is 0.785, which is derived from the difference in kinetic energy between the flow at the inlet and that in the fully developed region.

1.1.3 Studies on non-Newtonian transition

In assessing the literature on non-Newtonian fluid transition, it is important to be specific about the types of fluid that one wishes to study. For example, there is a relatively large literature on drag-reducing polymers, see e.g. Draad *et al.* [33] and the review articles by Berman [12] and White & Mungal [144]. Frequently, in such studies, non-Newtonian features can be interpreted as a small deviation from the Newtonian behaviour, in particular where the drag reduction is achieved via viscoelastic additives. For the fluids we consider, viscometric non-Newtonian effects are a dominant feature of the base laminar flow and we avoid fluids in which visco-elasticity is very significant. Our focus is thus on generalised Newtonian fluids. Simplistically, these are fluids in which the shear stress depends on the strain rate through an effective viscosity η which is a function only of the second invariant ($\dot{\gamma}$) of the strain rate tensor:

$$\tau_{ij} = \eta(\dot{\gamma})\dot{\gamma}_{ij}. \tag{1.5}$$

These fluids generally represent those in which shear rheology dominates. Many industrial fluids fall into this class, at least as a first order description. Well known rheological models include the Carreau-Yasuda, Cross, Casson, Bingham, power law, Ellis and Herschel-Bulkley models. The two main features of such fluids are shear-thinning behaviour, (in which the effective viscosity η decreases with $\dot{\gamma}$), and the possible existence of a yield stress, (a threshold in τ below which $\dot{\gamma} = 0$). Having said this, it is of course impossible to eliminate entirely other rheological effects in using real fluids. Xanthan is known to exhibit elastic effects in addition to its shear-thinning behaviour, (and shows drag reducing properties, see e.g. Escudier *et al.* [40]). Carbopol is often used as an experimental fluid for yield stress-shear thinning behaviour, but at low shear structural thixotropic effects can be quite visible. Other "model" lab fluids, such as Laponite suspensions, are also strongly thixotropic.

There are many studies of these types of fluids in pipe flow. For example, Metzner & Reed [90] considered a range of experimental data in establishing correlations for frictional pressure losses. Similarly, Hanks & Pratt [58] present results for yield stress fluids. See also texts such as Govier & Aziz [52] for an overview of this type of closure model and applications. In the petroleum industry, non-Newtonian pipe flow experiments are commonplace and conducted in order to continually evolve the accuracy of hydraulic predictions, e.g. Shah & Sutton [122], Willingham & Shah [147], or in response to new fluid types that are being pumped, e.g. Guo *et al.* [53]. In the mining industry, homogeneous slurries are often modelled as viscoplastic shear-thinning fluids, numerous experimental studies of different flow regimes have been carried out, e.g. Abbas & Crowe [1], Turian *et al.* [138], and transitional flow predictions have been developed which are popular within that industry, e.g. Slatter [125], Slatter & Wasp [126], Wilson & Thomas [145, 146]. Many of the approaches we have referenced above are targeted at accurate prediction of frictional pressure losses, with transition simply being considered as the intermediate step between fully laminar and turbulent flows. Thus, these do not study in a direct way the phenomena present in the transitional regime.

In shear-thinning non-Newtonian fluids the change in friction factor is generally much less abrupt on passing through transition, see e.g. various fluids tested in Escudier *et al.* [40], Metzner & Reed [90]. Thus, although still frequently used, and attractive since easily measurable in hydraulic situations, the accuracy of the friction factor method is certainly diminished. Other common detection methods for Newtonian fluids are based on observations of centreline velocity (as there is a large shift between laminar and turbulent profiles), or the rms velocity fluctuation.

Experimental studies

Park *et al.* [97] conducted LDA measurements for both laminar and turbulent flow of an oil-based transparent slurry with visco-plastic behaviour. They report that, due to the yield stress, there was very little difference between turbulent and laminar velocity profiles, hence detecting transition via the centreline velocity was ineffective. They advocated use of the turbulent intensity close to the wall, e.g. at 80% of the radius, which is also adopted by Escudier *et al.* [40]. On the other hand, Peixinho [99], Peixinho *et al.* [100] do manage to identify transition from centreline velocity data, although the detection is clearer for the fluids used other than Carbopol.

Wojs [148] measures friction factors in laminar, transition and turbulent flows and draws a moody diagram for some polymer solutions. He concludes that polymer additives extend and shift the transition region to higher Reynolds number values. The length of the transitional flow range increases with the solution concentration and molecular weight of the polymer.

Brand *et al.* [18] conduct an experimental study on a series of spacer and model fluids used in the cementing of oil and gas wells and compare their experimental results with different phenomenological criteria. Their conclusion is that critical Reynolds number increases with increasing yield value or power-law index, n. Only Mishra and Tripathi's and Slatter's criteria show this dependency. And Mishra and Tripathi's critical Reynolds number prediction gives the best result. These criterion will be discussed in

detail in the next section.

Flow asymmetries in the mean velocity profiles were first reported by Escudier & Presti [39], who studied the flow of Laponite suspensions in laminar, transitional and fully turbulent flows. They report asymmetry in the range $Re \in [1300, 3000]$. However, under all flow conditions they find that thixotropic effects are observable and the fluid is rarely at its equilibrium shear rheology, except in a very thin wall layer. This clouded any clear interpretation of the asymmetries. Peixinho [99] conducted pipe and annular flow experiments for carboxymethyl cellulose and carbopol solutions. In the transitional regime Peixinho [99] did not report observing flow asymmetries, although these were apparently evident and are reported later in Peixinho *et al.* [100].

Peixinho *et al.* [100] suggest that for yield stress fluids transition takes place essentially in 2 stages. In the first stage the turbulence intensity is at laminar levels on the pipe centreline whilst larger nearer the wall. It is unclear whether or not the plug is broken or intact, but it is suggested that due to the large fluctuations in effective viscosity, flow instabilities generated near the wall could be damped nearer the centre of the pipe. The aspect of flow asymmetry in transition is returned to by Escudier *et al.* [42]. These authors summarize the work of Escudier & Presti [39], Peixinho *et al.* [100] and a third independent study, in all of which asymmetry was observed in the mean velocity profiles. The authors discuss the possible effect of the Coriolis force on flow asymmetry, (following Draad & Nieuwstadt [32]), concluding that for the more viscous non-Newtonian fluids the Ekman number is simply too large for this to be a viable explanation. Other possible sources of experimental influence are also examined, with the conclusion that the asymmetry has fluid mechanics origins and is not due to imperfections in either the apparatus or measurement technique.

Theoretical studies

Questions arise related to the theoretical side of the problem, where there have been a number of studies of shear instability in flows of visco-plastic flu-

ids, typically for Bingham fluids. Frigaard *et al.* [46] studied 2-dimensional instabilities of plane channel Poiseuille flow, providing the correct formulation of the stability problem and linearisation at the yield surface, but considered odd and even perturbations separately which is questionable for this flow. A recent study by Nouar *et al.* [96], who implemented the correct conditions at the yield surface, suggests that plane Poiseuille flow is linearly stable at all Re, as is Hagen-Poiseuille flow. Thus, the transitional flow problem is similar in this respect to that for a Newtonian fluid. Three-dimensional linear instabilities have been studied in Frigaard & Nouar [47] and transient growth phenomena in Nouar *et al.* [96]. A key feature of the linear stability studies is that the plug region remains unyielded for linear perturbations. This fact can lead to interesting mathematical anomalies. For example, Métivier *et al.* [89] consider the distinguished asymptotic limit of linear stability with small yield stress, (vanishing slower than the linear perturbation), which corresponds to a rigid sheet in the centre of a plane channel and is linearly stable. They suggest that the passage to the Newtonian limit of a yield stress fluid is ill-defined insofar as questions of stability are concerned. These features reinforce the fundamental interest in plug behaviour during transition, i.e. based on the linear theory the flow is believed to be stable for all Re, but this linear theory itself is based on the continued existence of the plug region.

Apart from the linear analysis, fully nonlinear (energy) stability results are derived in Nouar & Frigaard [95]. As with the Newtonian fluid energy stability results these are very conservative. For yield stress fluids the nonlinearity of the problem is not simply in the inertial terms, but also in the shear stress and in the existence of unyielded plug regions, which are defined in a nonlocal fashion even for simple flows. This means that the gap between linear and nonlinear theories and between theoretical prediction and experimental evidence is much wider than with Newtonian fluids. Some effort to close this gap has been forthcoming in the form of computational work.

Computational studies

Rudman & Blackburn [114] studied turbulent pipe flows using LES and found that it is difficult to simulate pipe flows with LES. DNS study has been performed on drag deduction in polymer solutions (shear-thinning effects neglected) in turbulent flow (Sureskumar *et al.* [130], Angelis*et al.* [3] and Toonder & Nieuwstadt [135]). Rudman *et al.* [116] performed a DNS study of the weakly turbulent flow of a power law (shear-thinning) fluid and a Herschel-Bulkley (yield stress + shear-thinning) fluid using a spectral element-Fourier method. For the power-law fluid, as the flow index becomes smaller for the same Reynolds number, the flow deviates further from the Newtonian profile and the results suggest that transition is delayed. As a result, predicted friction factors fall above those in the literature, but below the Newtonian values when a comparison is undertaken on the basis of the Metzner-Reed Reynolds number. They concluded that using DNS for non-Newtonian fluids will remain a difficult task because of the difficulty in approximating a measured rheology over a very wide range of shear rates using any of the simple generalised Newtonian rheology models.

Later Rudman & Blackburn [117] did similar study for the same fluids using a spectral element-Fourier method (SEM) for Direct Numerical Simulation (DNS) and compared their results at the same generalised Reynolds number. They showed that the yield stress significantly dampens turbulence intensities in the core of the flow with larger, weaker turbulent structures compared to ones in Newtonian flows and smaller friction factors at a fixed generalized Reynolds number. So the addition of a yield stress to a power law fluid weakens the structures, driving the flow more toward the transitional regime. They also showed that pipe flow of yield stress fluids make the transition to turbulence via intermittency and turbulent events like the slugs and puffs observed in Newtonian flow. They did a simulation of a Carreau-Yasuda fluid as well. It showed similar behaviour to the Herschel-Bulkley results; the Carreau-Yasuda flow was transitional at similar Reynolds number. They proved that DNS has the potential to enable the effect of different rheological parameters to be correctly quantified and understood.

1.1.4 Review of different transitional criteria for transition of generalized Newtonian fluids

Beyond these few detailed studies of the flow structures in yield stress fluids, little is known about transition. At this point we turn our attention to a large body of work which focuses on empirical correlations used for engineering design purposes. Included in these correlations are estimates of when transition occurs.

Hedstrom [64] developed criteria for yield stress fluids, postulating that transition occurs at the point of intersection of the laminar and turbulent friction factor curves. Hedström argued that for a fully turbulent flow the effect of the yield stress is negligible and therefore used the well known Nikuradse relation for the turbulent friction factor in the pipe. More commonly this approach is known as the intersection method.

Metzner & Reed [90] and Dodge & Metzner [29] used the Fanning friction factor f as their stability parameter. A range of data from pipe flow experiments with different non-Newtonian fluids indicated that the data deviated from the laminar flow curve, at approximately the same ratio of viscous shear to inertial forces as do Newtonian fluid data in smooth pipes, i.e. $f \approx 0.008$. They therefore proposed that for all time independent non-Newtonian fluids flowing in pipes, transition would also take place when f drops to a critical value $f = f_c = 0.0076$. As well as the transition criteria, the Metzner-Reed Reynolds number, Re_{MR}, is in common usage. This is defined in such a way that in laminar flow, the friction factor relation is identical to that obtained for laminar pipe flow; e.g. for power law fluids:

$$Re_{MR} = \frac{8U_b^2\rho}{\kappa'\left(\frac{8U_b}{D}\right)^{n'}} : \qquad \kappa' = \kappa\left[\frac{1+3n}{4n}\right]^n, \quad n' = n. \tag{1.6}$$

The Reynolds number defined by Metzner and Reed has been generalised, by Kozicki *et al.* [81], to apply to laminar flows of purely viscous non-Newtonian fluids through ducts of arbitrary cross section. This concept was extended to the Bingham model by Govier & Aziz [52] and can be

straightforwardly generalised to any purely viscous non-Newtonian fluids, by assuming transition takes place at $f_c = 0.0076$, independent of the duct geometry or precise fluid. This generality has made the Metzner-Reed approach popular and it is is widely used. It is worth mentioning that the strength in the work comes from the convincing fitting of frictional pressure data for different polymeric fluids, see e.g. Dodge & Metzner [29], rather than a detailed examination of the transition criterion.

Pilehvari *et al.* [104], Reed & Pilehvari [110], extended this type of friction factor approach to a range of fluids having application in the Oil & Gas industry, and include wall roughness effects. In their work, which is typical of many other modifications, they focus principally on prediction of frictional pressures. Transition is defined as an intersection of laminar and turbulent friction factor curves. This may thus be viewed as a combination of the Hedström and Metzner-Reed approach.

Since the laminar and turbulent friction factors can be fitted to experimental data points and then extrapolated towards transition, it is clear that the friction factor approaches above have an inherent robustness to them. However, they are intellectually unsatisfactory in that there is essentially no hypothesis made about the mechanism for transition. A number of approaches have evolved that attempt to balance stabilizing and destabilizing effects on the flow, setting a criterion based on when this balance exceeds some critical value. Two identical predictions of transitional Reynolds numbers have been made by Ryan & Johnson [118] and by Hanks [56, 57], Hanks & Pratt [58], Hanks [59, 60, 61], Hanks & Ricks [62]. What is interesting is that these two predictions are arrived at using different approaches.

Ryan & Johnson [118] suggested using the ratio of input energy to energy dissipation for a fluid element as the stability parameter. They examine the situations in which the energy of a disturbance increases or decreases with time, considering the energy equation for a linear two-dimensional disturbance. The rate of increase of kinetic energy is equal to the difference between the rate at which energy is converted from the basic flow to the disturbance, via a Reynolds shear stress term. A ratio ζ is formed between the rate of increase and the rate at which energy is dissipated. The ratio ζ varies

with radial position and thus their approach can be thought of as a *local* approach. It is assumed that transitional instabilities will first appear at the radial position where ζ is maximal, for all purely viscous non-Newtonian fluids. Further, it is assumed that instability occurs when this maximal value of ζ exceeds a critical number, ζ_{crit}, regardless of the exact fluid type. The critical number ζ_{crit} is defined from the transition of a Newtonian flow and is given by $\zeta_{crit} = 808$.

Hanks derives exactly the same criterion as Ryan and Johnson. However, his reasoning is different and more direct. Hanks identifies the key mechanism leading to transitional instability as being rotational momentum transfer. Hanks introduces a parameter, ζ_H, which is almost identical to that of Ryan and Johnson. However, for Hanks ζ_H represents a balance between the rate of change of angular momentum of a deforming fluid element and its rate of loss of momentum due to frictional drag. Hanks' ratio ζ_H is exactly twice that of Ryan and Johnson. Hanks assumes that his transition criterion does not depend on the constitutive equation, for purely viscous fluids, or on the geometry of flow. The value of $\zeta_{H,crit}$, where the laminar motion becomes unstable, was determined to be 404 when the theory was applied to axial isothermal Newtonian flow in tubes.

A related approach followed more recently is due to Desouky & Al-Awad [28]. They consider transition to occur when the turbulent shear stress exceeds the laminar shear stress. Although a balance approach, the balance seems to revolve around a comparison of friction factors, for which the Metzner-Reed Reynolds number is used. Thus, it is similar to the friction factor approaches discussed above.

In a slightly different balance approach, Mishra & Tripathi [91] postulate that the important factors governing transition to turbulence are the mean kinetic energy and the wall shear stress. The onset of turbulence is assumed to occur at the same critical ratio of these quantities for all purely viscous non-Newtonian fluids. This ratio is fitted from its value for Newtonian fluid transition in a pipe. Whereas the above approaches are local, this approach considers a more global balance.

Thomas & Wilson [134], Wilson & Thomas [145] developed a new analy-

sis for the turbulent flow of non-Newtonian fluids based on viscous sub-layer thickening. They analyzed the near-wall structure of the velocity field in a smooth wall pipe flow for power-law suspensions and Bingham plastics, and reported that the viscous sub-layer for these non-Newtonian turbulent flows is generally thicker than for the equivalent Newtonian flows. This resulted in a much lower turbulent friction factor for the non-Newtonian fluids when compared to a Newtonian fluid. In latter work, they extended their analysis to include the effect of surface roughness for laminar-turbulent transition for Bingham plastics (Wilson & Thomas [146]). Here, they showed that there is a direct relationship between yield stress and the transition velocity, and the conditions at transition depend only on the Hedström number,He.

A recent approach popular in the mining industry, is due to Slatter & co-workers, Slatter [125]. He treats the unyielded region as a solid body which has no effect on the stability of flow. Therefore, only the flow of the sheared fluid in the *annulus*, between pipe wall and unyielded plug, is considered. Slatter defines a Reynolds number based on the effective viscosity of the annular flow, i.e. using the hydraulic diameter of the annulus and an effective rate of strain. Slightly later, Slatter & Wasp [126], propose a correlation for the critical Reynolds number, based on different ranges of Hedström number.

It is interesting that although there are numerous comparative studies of pressure drop closure relations, there are few that compare criteria of transition. In one such study, Nouar & Frigaard [95], predictive criteria were plotted for five of the above methods, all for the case of Bingham fluids. These predictions are calibrated to return the same values for Newtonian fluids. It was shown that at moderate values of the Bingham number, B, (indicating the relative importance of the yield stress to viscous stresses), there was a significant divergence in the predictions of transitional Re. At larger Bingham numbers it was also shown that the asymptotic limits of these predictions exhibit very different asymptotic behaviour. It was concluded that in the large B limit, only the prediction of Hanks did not violate theoretical constraints.

The two dimensionless parameters mentioned above are the Bingham

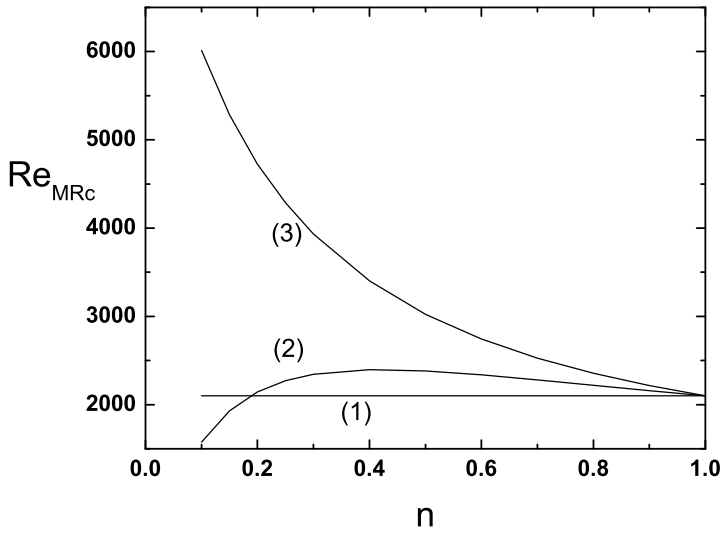

Figure 1.1: Critical Metzner-Reed Reynolds number as a function of power-law index, n. Comparison between (1) Metzner and Reed criterion, (2) Hanks criterion and (3) a criterion based on $Re_G = 2100$

number, B, and the Hedström number, He, which are defined by

$$B = \frac{\tau_y R}{U_b \mu_p} \qquad\qquad He = ReB \tag{1.7}$$

Here, R the pipe radius, U_b the mean axial velocity, μ_p the plastic viscosity and τ_y the yield stress.

In Fig. 1.1 we compare transitional values (in terms of Re_{MR}) for the Metzner-Reed criterion, the Ryan & Johnson/Hanks criterion and a criterion to be discussed later that states $Re_G = 2100$. We observe that for varying n the criteria give quite different predictions of transition.

1.1.5 Review of predictive models for Newtonian and non-Newtonian fluids

While linear stability analysis could be useful to predict when a flow becomes unstable by defining a threshold, it can't describe the evolution of unstable modes above the threshold. Weakly nonlinear theories are used in order to study further development of instability (Drazin & Reid [34], Stewartson &

Stuart [129]). One of the most common amplitude evolution equation is the Ginzburg-Landau equation derived from the Navier-Stokes equations. Because of its relatively simplicity, this equation has wide range of applications in fluid mechanics for spatio-temporal dynamics of complex flows (Aranson & Kramer [4]).

Deissler [27] studies the time-dependent generalized Ginzburg-Landau equation under conditions when it is convectively (spatially) unstable. In the presence of infinitesimal disturbance, this system exhibits a selective spatial amplification of noise resulting in spatially growing waves. These waves in turn result in the formation of a dynamic structure that leads to instability.

Bohr *et al.* [17] use the complex Ginzburg-Landau equation. The convective instability and local dynamical instability combine to give the sudden eruption of localized patches of turbulence. Their idea is a convective exponent, a Lyapunov exponent, associated with a convective velocity. While normally small disturbances are damped out by system, convective stability introduces instability into the system.

Fowler & Howell [45] propose a phenomenological model which explains the difference of flow resistance in laminar and turbulent flow in a quantative way through a hysteretic transition characterized by a disturbance amplitude variable that satisfies a natural type of evolution equation. Their model predicts oscillations similar to those, which occur in intermittency in pipe flow, and naturally predicts disturbances having the characteristics of puffs and slugs.

1.1.6 Summary

With such a range of phenomenological predictions available and an enduring interest in advancing new criteria, we should question where the difficulties arise in specifying transition. It appears to us that the difficulties may be grouped into 3 distinct categories: (i) transition is not a well-defined phenomena; (ii) the complexities of different fluids are not well understood and accounted for; (iii) detection of transition in a flow is difficult.

Regarding the first of these, although transitional Re for Newtonian fluids are typically quoted at $Re \approx 2100$, values between 1760 and 2300 are routinely reported, see e.g. Darbyshire & Mullin [25], Kerswel [77]. In especially constructed apparatus it has been possible to achieve stable laminar flows at Re in the 20000-60000 range, see Draad *et al.* [33], Hof [68]. Theoretically the transition is subcritical and believed linearly stable at all Re. Thus, these high Re stable flows are essentially giving a measure of the quality of the experimental flow loop in eliminating noise. Clearly, the common engineering perspective that "transition" (meaning the end of the laminar regime) will occur at a given Re is flawed, even for a Newtonian fluid.

The second difficulty really concerns the fact that generalised Newtonian fluid models are almost always an approximation to a more complex rheological behaviour, which may include elements of visco-elasticity, thixotropy or multi-phase effects. Many fluids exhibit a similar laminar velocity profile in shear flow, but are otherwise distinct. It is notable that new criteria often are developed focused at one particular industrial setting, where inadequacies in prediction have been exposed. There is little *a priori* reason why a prediction of transition in say a dilute polymer solution should be valid also for, e.g. a homogeneous slurry (multi-phase) or a pulp suspension. We feel it is necessary to focus more clearly on the type of fluid and to incorporate a detailed understanding of the transitional flow into any prediction.

Regarding the third difficulty, we note that for many shear-thinning fluids, sharp changes in the frictional pressure (Moody diagram) are suppressed, so there is no easily identifiable "transition point". Equally, rapid changes in the turbulence intensity do not necessarily occur first at the centerline. Thus, the common ways of detecting transition for Newtonian fluids are less effective.

Finally we find that the literature characterizing transition in these fluids are relatively unexplored in comparison to its Newtonian counterpart. We feel that a fundamental understanding of the mechanism is required before attempting to develop empirical correlations used for design purposes.

1.2 Research objectives

As outlined in the literature review, these are a number of motivations for this study:

(i) Fluids of shear-thinning type with a yield stress abound in industrial settings, as well as some natural ones. Our particular motivation here comes from both the petroleum industry and the pulp and paper industry, where design/control of the inherent processes often requires knowledge of the flow state at different velocities. Similar fluid types and ranges of flows occur in food processing, polymer flows and in the transport of homogeneous mined slurries. Although many of these industrial fluid exhibit more complex behaviour, (e.g. thixotropy, visco-elasticity, etc), as noted by Bird *et al.* [14], the shear-dependent rheology is often the dominant feature.

(ii) There is a demand from industrial application to predict the Reynolds number, ($Re = UD/\nu$, where U is the average velocity, D is the diameter of the pipe and ν is the kinematic viscosity), or other bulk flow parameter, at which transition occurs, for a range of fluid types, so that different frictional pressure closures may be applied to hydraulics calculations above/below this limit. There is a difficulty with interpreting the predictions of phenomenological formulae, many of which we note were either formulated before a detailed understanding of transitional phenomena has developed. Although such a predictive *guideline* is a worthy goal, and one we address in this thesis, it is clear that a necessary precursor to this is a detailed study of transition phenomena, which we provide here.

(iii) A third and most important motivation for our study is scientific. Since Reynolds' famous experiment (Reynolds [112]), transition in pipe flows has been an enduring *unsolved* problem in Newtonian fluid mechanics. It is thus natural that there have been far fewer studies of non-Newtonian fluids in this regime, either experimental or numerical/theoretical. However, those studies that have been conducted for shear-thinning visco-plastic fluids leave unanswered a large number of intriguing questions.

With this in mind, the specific objectives in this work are:

(a) to experimentally characterize the role of the plug during transition.

This has been attempted in previous works (Peixinho [99], Peixinho *et al.* [100]) however the dimensions of the pipe were too small to detect the plug unambiguously near transition.

(b) to characterize systematically the differences between the flow structure in Newtonian and non-Newtonian fluids and in an attempt to elucidate a mechanism for transition.

(c) to develop a clear understanding of when the flow is fully turbulent and to define a criteria which can be used for engineering purposes.

Chapter 2

Experimental setup and procedures

All results reported are from tests performed in a 10 m long flow loop with an inner diameter of 50.8 mm. The setup is illustrated schematically in Figure 2.1. The flow is generated by a variable-frequency driven screw pump fed to a carbon steel inlet reservoir $\mathbf{R_1}$ of approximately 120 L capacity to an outlet reservoir $\mathbf{R_2}$ of the same capacity. The pump can provide a maximum flow rate of $\approx 22\ l/s$, which is equivalent to a maximal mean flow velocity of $\approx 10\ m/s$. Two honeycomb sections are placed inside the reservoir $\mathbf{R_1}$ before the tube inlet in order to suppress any swirl or other fluid entry effects. We used a borda style entry condition in which the pipe extended approximately 50 cm into the tank. Two honeycomb elements were inserted into this section. The fluid reservoir $\mathbf{R_2}$ is pressurized to damp mechanical vibrations induced by the pump motor and a flexible hose is used between the pump and reservoir in order to diminish flow pulsations. The flow channel is constructed of 16 identical sections, 61 cm in length each, joined with flanges and aligned horizontally with the aid of a laser.

The test section of the pipe (placed at about 5.5 m downstream) is fitted with a "fish tank", **FT**,which consists of a rectangular transparent acrylic box filled with an index-matched fluid (glycerol) in order to minimize the effects of refraction. Velocity measurements are made by using a laser doppler velocimetry (LDV) system from TSI instruments (www.tsi.com). The LDV comprises a 400 mW argon-ion laser (wavelength $457 - 514\ nm$), a 2-component probe (**PB**) housing the transmitting and receiving optics, a color separator and a burst spectrum analyzer, **BSA**. The probe is mounted

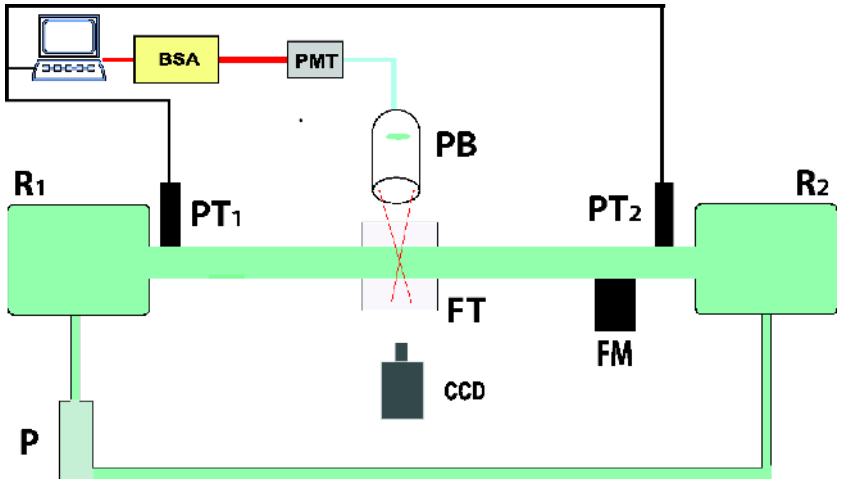

Figure 2.1: Schematic view of the experimental setup: $\mathbf{R_{1,2}}$ - fluid reservoirs, **P** - pump, **FM** - flow meter, $\mathbf{PT_{1,2}}$ - pressure transducers, **FT** - fish tank, **CCD** - digital camera, **PB** - laser Doppler velocimetry probe, **PMT** - photomultiplier, **BSA** - burst spectrum analyzer.

on a three-axis translational stage with a spatial resolution of 10 μm. The working fluids are seeded with silver coated hollow glass spheres, 10 μm in diameter, in order to enhance the LDV signal. The LDV optical parameters are as follows:

1. the probe beam diameter is 2.82 mm
2. the beam separation at its front lens is 50 mm
3. the focal length of receiving lens is 362.6 mm
4. the diameter of the measurement volume is 0.0858 mm (measured in air).

Two pressure transducers ($\mathbf{PT_{1,2}}$) are located near the inlet and outlet of the flow channel (Model 210, Series C from www.gp50.com). These are bonded strain gauge transducers with internal signal conditioning to provide a Vdc output signal in direct proportion to the input pressure. The accuracy of each transducer is 0.2% of the full scale and they were calibrated with an

externally mounted pressure gauge. Pressure readings were averaged over 150 s and used to estimate the radius of the plug, see Equation 3.4. Flow rates were estimated using two methods: (i) using an electromagnetic flow meter (**FM**) installed near the outlet reservoir, see Fig. 2.1; (ii) by numerically integrating the measured axial velocity profiles. The latter estimate is used to calculate the relevant flow parameters reported through our study.

Before proceeding it is instructive to estimate if the flow is fully developed at this measurement location. The case to consider is that of a laminar flow of a Newtonian fluid as it is widely known that the entry length for turbulent flows (Doherty *et al.* [30], Laufer [70], Nikuradse [94], Perry *et al.* [103]) and for flows with non-Newtonian fluids (Bogue [16], Chen [21], Soto *et al.* [128], Bewersdorff [13], Froishteter *et al.* [50]) is smaller. Poole *et al.* [106] modified the recently proposed correlation for Newtonian fluid flows by Durst *et al.* [36] for inelastic non-Newtonian fluids obeying the power-law model and proposed a unified correlation for the entry length, which is valid in the range $0.4 < \mathrm{n} < 1.5$ for the three different definitions of the Reynolds number. They argued that depending on the Reynolds number definition used, different conclusions can be drawn regarding the effect of power-law index on the entry length. Use of the $Re_M R$ allows the development length at high Reynolds numbers to collapse onto a single curve (i.e., independent of the power-law index n). For the laminar case, Durst *et al.* [36] reports that it is widely accepted that the entry length Le/D scales with Re/30; there is however a wide variation in this estimate (see Durst *et al.* [36], Poole *et al.* [106]). With this, at Re =3000 the entry length in our apparatus is roughly Le/D=100. This is significantly shorter than the position of our measurement point, i.e. $\mathrm{Le/D} = 108$. In addition to satisfying this criterion, we examined a second criterion to establish if the flow was fully developed. Like Durst *et al.* [36]and Poole *et al.* [106], we examined the measured centerline velocity and compared this to an estimated velocity using the pressure drop and viscosity of the fluid. We found that for all cases tested there was less than a 1% deviation from these results.

The experimental procedure consisted of the following steps:

1. Each fluid tested was mixed *in situ* by circulating the fluids through the flow channel for $5-6$ hours. The test fluid was then allowed to rest for $4-5$ days so that any entrained air bubbles may be dissipated. A fluid sample was then obtained from the reservoir tank and used for subsequent rheological evaluation.

2. During each run, the temperature of the fluid varied by less than one Celcius degree. No active measures were made to control temperature in this experiment. At the start of an experimental sequence, the desired flowrate was set and the flow loop was then run for a period of time until the temperature stabilized. Once stabilized data acquisition commenced. In this case we record both the volumetric flowrate and instantaneous pressure at a sampling rate of 500 Hz.

3. The velocity profile was measured stepwise across the diameter of the pipe in 1.25 mm increments. At each radial position, the flow was sampled for approximately 150 s at an average rate of 1000 Hz. This data was also used to estimate the local strain rate $\dot{\gamma}$. To do so the derivative was estimated by using a second-order finite difference scheme with a step size of 1.25 mm (2.5% percent of the diameter of the pipe) between adjacent nodes. The time-average value at each nodal point was estimated from approximately one-hundred thousand readings; the coefficient of variation was much less than one percent. Given this large number of data points, the difference between the averages of velocity between adjacent points were statistically significant and the error on this time average derivative is low.

4. At the end of the traverse a fluid sample was obtained, the flowrate increased and the measurement traverse repeated.

All the fluids used in our experiments were transparent, allowing both LDV flow investigation and direct high-speed flow imaging. In total 11 different fluids were tested. The experimental limits such as the mean velocities, concentrations and the corresponding generalised Reynolds numbers, (denoted Re_G), for all the fluids we have tested are summarized in Table 2.1.

Fluid	*Concentration* (wt %)	Velocity U_b (m/s)	Re_G
Glycerin	80	0.37 - 1.49	731 - 4442
Glycerin	65	0.06 - 1.95	342 - 14180
Xanthan	0.05	0.17	1984
Xanthan	0.1	0.38 - 2.02	1701 - 24746
Xanthan	0.2	0.46 - 2.59	451 - 5070
Xanthan	0.2	0.28 - 3.75	352 - 11272
Carbopol	0.05 (6.7 pH)	0.14 - 1.49	356 - 10960
Carbopol	0.08 (7.1 pH)	0.39 - 2.92	170 - 5134
Carbopol	0.10 (6.9 pH)	0.31 - 3.50	42 - 3309
Carbopol	0.10 (6.6 pH)	0.11 - 4.59	6 - 6032
Carbopol	0.15 (6.8 pH)	0.13 - 4.84	2.7 - 2953

Table 2.1: A summary of the experimental conditions tested. For each fluid, at least 7 different bulk velocities were chosen to cover the range indicated in the table.

The values given for each fluid represent the minimum flow rate (fully laminar regime) and the maximum flow rate (fully developed turbulent regime) conditions. The Reynolds number may be defined in a number of ways for non-Newtonian fluids. We have defined a generalised Reynolds number by:

$$Re_G = \frac{4\rho}{R}\int_0^R \frac{\bar{u}(r)}{\eta(\dot{\gamma}(r))} r dr. \tag{2.1}$$

where ρ and η are the density and effective viscosity of the fluid. The latter depends on the strain-rate of the base flow, $\dot{\gamma}(r)$, which is calculated locally from the mean axial velocity. For a Newtonian fluid, $Re_G = Re$, and algebraic relations between Re_G and other commonly used non-Newtonian Reynolds numbers may be easily derived. For laminar flows some simple algebraic manipulations yield the expression:

$$Re_G = \frac{4\rho u_c^2}{R|p_x|}. \tag{2.2}$$

We note here that both Xanthan and Carbopol solutions may exhibit elasticity at low shear rates, but for the ranges of flow rates considered in our experiments, it is the shear-rheology that dominates. As a result, in this work the Xanthan solutions used are modeled as power-law fluids:[1]

$$\tau = \kappa\dot{\gamma}^n; \quad \eta = \kappa\dot{\gamma}^{n-1}. \tag{2.3}$$

The yield stress fluid, Carbopol, is characterized as a Herschel-Bulkley fluid:

$$\tau = \tau_y + \kappa\dot{\gamma}^n; \quad \eta = \tau_y\dot{\gamma}^{-1} + \kappa\dot{\gamma}^{n-1} : \quad \tau > \tau_y. \tag{2.4}$$

The parameters τ_y, κ and n are commonly referred to as the fluid yield stress, consistency and shear-thinning (power-law) index, respectively.

The shear rheology of the samples were measured for each fluid sample at the same temperatures as the fluids in the flow loop (see Escudier *et al.* [40]). The viscosity dependence of Xanthan solutions with temperature has been investigated by several authors (see Valdez *et al.* [139]). Viscosity can be higher or lower, or does not vary with the increase of temperature, depending on the shear rate. Valdez *et al.* [139] has found that viscosity varies about 1-3% in a wide range of temperature for Xanthan solutions. Park & Irvine [98] did the viscosity measurements of four Carbopol solutions at various temperatures and found that, while the viscosities of the 3500 and 5000 wppm of Carbopol 934 solutions decreased with increasing temperature at a rate of about $1\%/^0C$, the viscosities of the 7500 and 10000 wppm solutions increased with increasing temperature. Similar measurements for 2% Carbopol 934 solutions were done by Lu & Jun [85], giving the decreasing rate of less than $1\%/^0C$ for viscosity with increasing temperature. Later Escudier *et al.* [41] stated that for small temperature differences the viscosity can be assumed to vary linearly with temperature in a similar way to that of water ($3\%/^0C$).

For pipe flows the radial temperature gradient is generally much higher than the axial temperature gradient. Gasljevic *et al.* [51] obtained the

[1] Although the flow curve for Xanthan can be better fitted by the Carreau-Yasuda model or the Cross model, the power-law model is preferred for its simplicity in calculations.

temperature profiles in turbulent pipe flows for polymers and surfactant solutions in a stainless steel tube of 19.95 mm ID. Their measurements are done at relatively high Reynolds numbers, between 10 000 and 90 000. They controlled the wall heat flux to maintain a wall-to-bulk temperature difference about 2^0C for most tests. With this temperature difference, the effect of the radial temperature variation on the fluid viscosity was not more than 4% for average test conditions. When the wall-to-bulk temperature difference is about 1.6^0C, the corresponding wall heat flux is $755W/m^2$. Considering the $0.2W/mK$ of thermal conductivity of acrylic, this amount of wall heat flux would occur in much higher air to fluid temperature difference in our setup (order of 100^0C). So we didn't expect any significant radial temperature gradients in our experiments. Moreover, in turbulent flows, most of the temperature difference between the wall and the fluid takes place close to the wall, although somewhat less so for drag-reducing than Newtonian flows (Gasljevic *et al.* [51]).

Rheological measurements were performed on a controlled-stress rheometer (CVOR 200, from Bohlin, now Malvern Instruments) with a 1° 40 mm cone and plate geometry and 25 mm vane tool. A standard v25 (four blades, vane length 42 mm) vane geometry (www.malvern.co.uk) was employed in these tests and the yield stress was determined by a stress ramp method (Nguyen *et al.* [92]). The vane tool was used for measurements of the yield stress because wall slip effects are known to be absent for this geometry (see Barnes & Nguyen [9]). Pernell *et al.* [102] determined yield stress for protein foams by using vane geometry. They used four different height-to-diameter ratios of the vanes and showed that using different vane geometries give the same yield stress values. Saak *et al.* [119] investigated the influence of wall slip on the shear yield stress and modulus of cement paste using a rotational rheometer with smooth-walled concentric cylinders and a vane. Their results showed that the concentric cylinders suffer from slip during yield stress measurements due to the formation of a water-rich layer at the walls of the cylinders. The use of a vane eliminates slip since shearing occurs within the material. The data for the vane and concentric cylinders are in excellent agreement at stresses below the yield point. For the viscosity

measurements in a high shear rate range (which corresponds to most of our experimental domain) the cone and plate geometry was used. Escudier *et al.* [41] performed a detailed uncertainty analysis for the double-concentric gap geometry. They found that for $\dot{\gamma} > 1s^{-1}$ the total uncertainty is about 2%. For the cone-and-plate and parallel-plate geometries at high shear rates, the same values of total uncertainty apply because in that range the uncertainty is dominated by the angular speed contribution which is independent of the geometry used. The empirical constants describing the rheology were determined by comparison to both this rheogram *and* to the laminar velocity profiles measured in the pipe. Degradation is apparent in the rheological properties of the structured fluids. Table 2.2 details the change in rheology after every flow rate for 0.1% carbopol.

Finally, it is widely known that a weakness of both the power law and Herschel-Bulkley models is that there is no high-shear limiting viscosity. Thus, parameter-fitting from the flow curve can give different results depending on the range of strain rates used for the fit. Here we fit model parameters from the fluid samples taken before each experiment and use flow curve data that covers the approximate range investigated in the experiment. Figure 2.2 provides an illustration of how using different strain rate ranges, for the same fluid, can result in different parametric fits for the same Xanthan solution. Tables of fitted parameters for each experiment reported are given in appendix §B. The parameters fitted obviously have no influence on the results reported here; these are included for completeness and as an aid to future comparisons with computational and theoretical approaches.

Experimental uncertainties caused by small imperfections of the pipe, temperature gradients in the room or degradation of the tested fluids generally have a smaller effect on the calculated Re_G than using incorrect rheological parameters. By "incorrect", we mean either that the parameter fit is made from data covering the wrong range of strain rates, or that the fluid sample is taken from an unyielded/stationary zone in the end reservoirs (as opposed to the yielded parts), or that care is not taken to cross-check the rheological data against the pipe flow velocity profile (in laminar regime

only).

The largest errors almost certainly arise in the yield stress. In reality, yielding behaviour is observed over a range of stresses and specifying a single yield stress value is simply a fitting parameter. This range is estimated by using the stress ramp method with vane rheometer measurements. For any given yield stress fitting the other rheological parameters to the flowcurve data is a robust procedure. Having determined ranges of rheological parameters we then compare normalized velocity profiles from the LDV measurements with those calculated from the rheological model, (which are dimensionlessly parameterized by n and r_p), to determine the final parameters.

Evidently, many different errors contribute to the value of Re_G. A reasonable error estimate for Re_G is obtained by comparing the Re_G that is calculated from the rheological parameters, constitutive law and velocity profile, i.e. equation (2.1), with that computed from the pressure drop and centreline velocity, i.e. equation (2.2). For different concentrations of Carbopol, the difference between these two Re_G calculated for the same flows is 1-2% at smaller Reynolds numbers and increases to 10-15% at higher Reynolds numbers close to transition. It is interesting to note that at low shear values, where errors in yield stress dominate, the contributions to Re_G in calculating the integrand in (2.1) are smallest, due to the large effective viscosity. The Re_G calculated with pressure drop underestimates the true value of Re_G because the entrance pressure losses are included. For comparison, the difference between these two values of Re_G for glycerin is about 1-5% for laminar flows.

Note that as velocity profiles become turbulent, due to nonlinearity in the constitutive laws, the effective viscosity of the averaged velocity profile may not be an accurate measure of viscous effects in the flow and a discrepancy between (2.1) and (2.2) is inevitable. More concisely, deriving (2.2) relies on a constitutive law relating the averaged velocity profile (via an effective viscosity) to the mean shear stresses and hence pressure drop. The constitutive relation is not known for the turbulent flow. This same difficulty arises with other commonly used generalised Newtonian fluid Reynolds

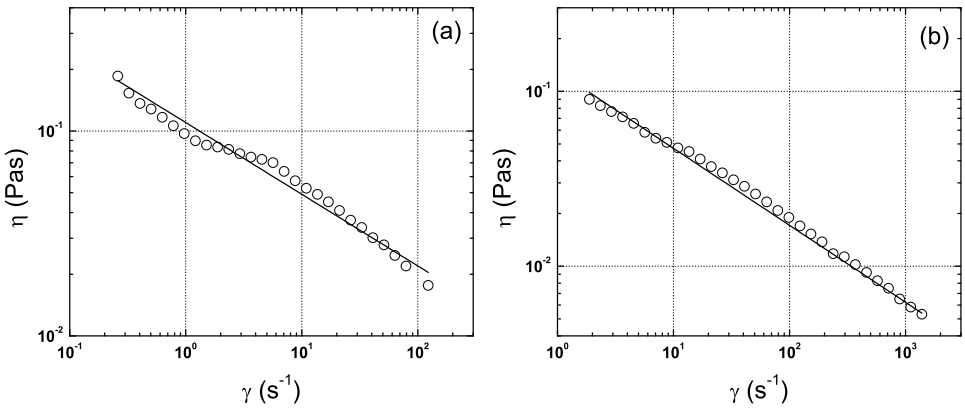

Figure 2.2: Rheograms for 0.2% Xanthan gum solution, described by the power-law model: (a) $\kappa = 0.11\ Pa.s^n,\ n = 0.65$ (b) $\kappa = 0.13\ Pa.s^n\ , n = 0.56$

numbers, which are typically based on the laminar flow characteristics, e.g. the Metzner-Reed Reynolds number.

As with Re_G, we can either evaluate r_p directly from the rheology and velocity profile fit, (as we have used in the figures and tables presented below), or we can use the yield stress and measured pressure drop. Since both methods are vulnerable to errors in the yield stress, the level of precision using either estimate is comparable. However, r_p calculated from the pressure drop underestimates the true value because the entry length losses are included in the pressure drop measurement. Values of r_p are about 5-20% lower than those calculated from the rheology and velocity profile fit.

2.1 Verification of the setup

Pressure transducers and the flow meter were calibrated before starting the experiments. A digital pressure calibration device is used to calibrate the transducers, by applying certain pressure values between 0 and 200 psi and comparing them with the device readings. Then the voltage output of the transducers is adjusted accordingly. The flow meter is calibrated with a digital weight scale while water is the running fluid.

$U(m/s)$	$\dot{\gamma}(s^{-1})$	$\tau_y(Pa)$	$K(Pa.s^n)$	n	Re_G
0.11202	$0.1-24$	2	2.05	0.36	5.5
0.4622	$0.1-87$	1.5	2.01	0.40	67
1.2076	$1-220$	1.4	1.59	0.43	378
2.0461	$5-414$	1.3	1.20	0.48	937
2.3218	$5-472$	1.2	0.92	0.53	1160
3.1146	$5-657$	1	0.65	0.60	1735
3.9005	$5-1261$	0.6	0.35	0.65	2920
4.3967	$5-1559$	0.4	0.20	0.70	4488

Table 2.2: Flow conditions and Herschel-Bulkley parameters for 0.1% Carbopol

Buoyancy arising from ambient temperature gradients or inhomogeneity in density due to solid particles could lead asymmetry in pipe flows (Lin & Ebadian [83]). To verify the setup, we first ran experiments with water and glycerin as Newtonian references. We made sure that we measure symmetrical velocity profiles from laminar to turbulent and obtained the critical Reynolds number as ~ 2100 for our setup in Newtonian transition. The velocity profiles for Newtonian fluids can be seen in Appendix B.

Chapter 3

Results

The results presented in § 3 and in § 4 have been documented in the following publications:

1. B. Güzel, T. I. Burghelea , I.A. Frigaard, D.M. Martinez, 2009, "Observation of laminar-turbulent transition of a yield stress fluid in Hagen-Poiseuille flow ", Journal of Fluid Mechanics.

2. B. Güzel, I.A. Frigaard, D.M. Martinez, 2009, "Predicting laminar-turbulent transition in Poiseuille pipe flow for non-Newtonian fluids", Chem. Eng. Science, 64, pp.254-264.

We are presenting in this chapter a synopsis of the most relevant experimental results. The figures for each flow rate of the all tested fluids and the related LDV readings can be found in the appendices.

3.1 Characterizing transition

Before proceeding to the main findings, it is instructive to first examine representative velocity profiles for all fluids and flow states measured. To this end, we plot the time-averaged velocity profiles as a function of Re_G, see Figure 3.1. At each radial position, over one-hundred thousand instantaneous velocity measurements were used in the ensemble average and the confidence interval for each point is very small. It should be noted that the results have been made dimensionless by scaling the ensemble average with the centerline velocity u_c. Under laminar conditions, that is with $Re_G < 1700$, the fully developed laminar profiles are included in these graphs as the solid lines. These laminar profiles were constructed with the corresponding rheological parameters for each Reynolds number. This was performed in order to ascertain the validity of our results. For the higher flowrates, we present cases

for both transitional and turbulent flows. Dashed lines are drawn to highlight an apparent asymmetry in the measurements. The dashed lines were constructed by averaging the data at equivalent radial positions on either side of the central axis. The asymmetry is apparent for the non-Newtonian cases and disappears once full turbulence is achieved. It is worth noting that the asymmetry is systematic, i.e. these data were taken from time-averaged data and the asymmetry is consistently in the same part of the pipe for the same fluid. This is highlighted in Figures 3.2 and 3.3 where experimental conditions are replicated resulting in a similar bias in the result. It should be noted in the figures that the asymmetry show no directional dependence. The profiles in this case may be skewed in either direction. This persistence runs contrary to the intuitive notion that transitional flow structures, when ensemble averaged over a suitably long time, should occur with no azimuthal bias. A similar asymmetry has been reported by other groups in their experiments, see e.g. Escudier & Presti [39], Escudier *et al.* [42], Peixinho *et al.* [100]. Our initial reaction to the asymmetry was to look for and eliminate any directional bias in the apparatus or in the flow visualization. However, even after extensive precautions the asymmetry still persists. A similar result is observed in the radial profiles of the local RMS of the velocity fluctuation for the non-Newtonian fluids. A representative case is given in Figure 3.4 for a 0.2% Xanthan gum solution. One can notice from Figures 3.2(a) and 3.4 that the peak asymmetry in u_{rms} profiles is on the opposite side to the asymmetry seen in mean velocity profiles.

Figure 3.5 plots the evolution of the turbulent intensity with Re_G, both at the centreline and at radial positions $r/R = \pm 0.75$. Other radial positions could have been displayed, but we chose to show these three as it clearly defines the phenomena that we wish to discuss. To begin, the first observation that can be made is that for Newtonian fluids, (see Figure 3.5a), in the laminar regime we see a decay in turbulent intensity as flow rate is increased. This decay is due to having approximately the same magnitude of noise in the system while increasing mean velocity. This is valid for all of the experiments. On transition there is a sharp change in turbulent intensity that occurs across the pipe section simultaneously, i.e. at the same Re_G.

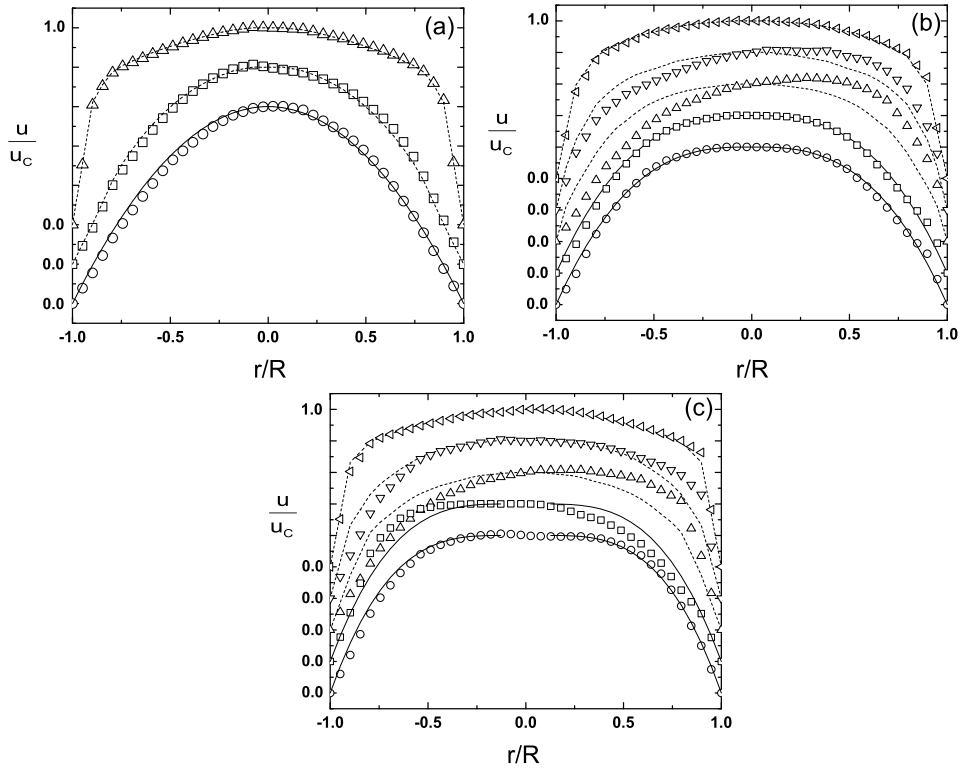

Figure 3.1: The time averaged velocity profiles for the three different fluids tested. (a) 65% Glycerin at Re_G=633(◯), 2573(□) and 10531(△); (b) 0.2% Xanthan gum at Re_G=809(◯), 1185(□), 2244(△), 2542(▽) and 3513(◁); and (c) 0.15% Carbopol at Re_G=561(◯), 1120(□), 1750(△), 1804(▽) and 2953 (◁)

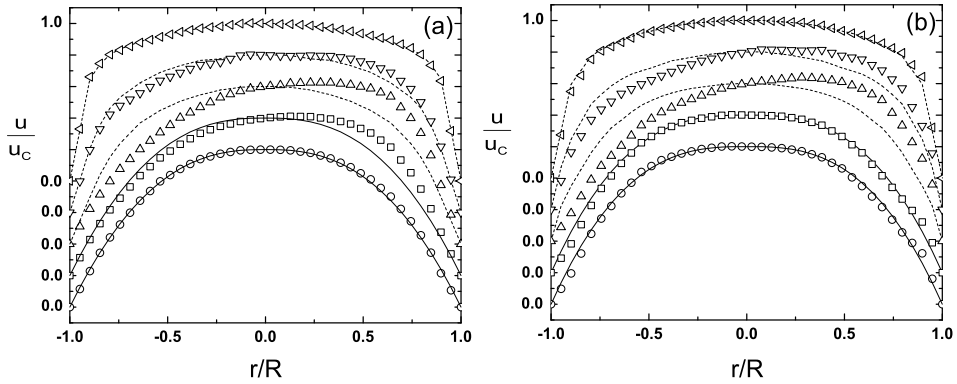

Figure 3.2: The time averaged velocity profiles for 0.2% Xanthan gum. These data are from replicate tests obtained from similar experimental conditions (a) Re_G=858(◯), 1218(□), 1900(△), 2363(▽) and 3244(◁) (b) Re_G=809(◯), 1185(□), 2244(△), 2542(▽) and 3513(◁)

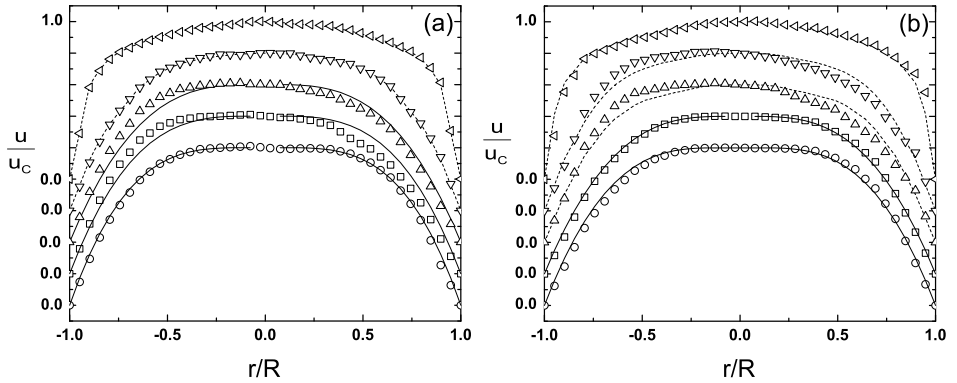

Figure 3.3: The time averaged velocity profiles for 0.1% Carbopol. These data are from replicate tests obtained from similar experimental conditions. (a) Re_G=378(◯), 937(□), 1160(△), 1735(▽) and 2920(◁) (b) Re_G=397(◯), 914(□), 2001(△), 2238(▽) and 2612(◁).

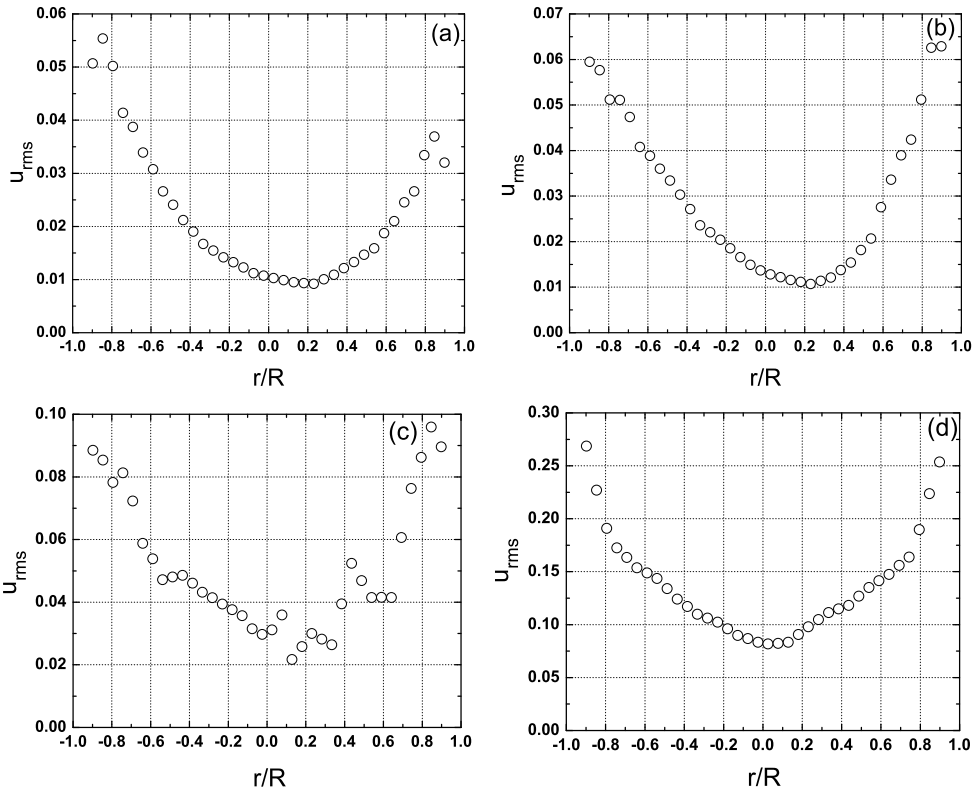

Figure 3.4: Local RMS Velocity Profiles for 0.2% Xanthan Gum; (a) at Re_G=858, (b) at Re_G=1218, (c) at Re_G=1900, (d) at Re_G=3244

After a rapid increase through transition the turbulent intensity relaxes as we enter the fully turbulent regime. For the structured fluids, transition does not involve a simultaneous and sharp increase in turbulent intensity, across the pipe radius. Instead in Figures 3.5b & c we observe that the turbulent intensity begins to increase at $r/R = \pm 0.75$, at markedly lower Reynolds numbers than at the centreline. A pattern that we noticed that is generally found for the structured fluids tested is that the slope of the curve near transition was rarely negative. This observation will be confirmed below through direct visual observation of turbulent puffs through high speed imaging. In this study it was difficult to classify the turbulent spot as either a puff or a slug. This is not a unique finding as other research groups without active disturbance control mechanisms report similar findings (Rudman *et al.* [116]). As a result in the subsequent text we use the term puff and slug synonymously. A simplistic explanation for this different behavior is that the effective viscosity is usually significantly larger close to the centreline for shear-thinning fluids in laminar flow.

Apart from measuring the axial velocity, we also visualized the flow via seeding particles and a two-colored art dye, for which the color changes with the orientation of particles. This enables qualitative evaluation of the flow, i.e. the particles in turbulent structures are a different color than the ones in laminar regimes. The images are then processed and some features of the turbulent spots (puff/slug) are derived from these images. The recording station is placed at about 7.6 m downstream. Our imaging system consisted of a Mega Speed MS70K type high speed video camera (504×504 pixel spatial resolution with a maximum framing rate of 5200 frames per second) mounted with a 25 mm lens. A typical sequence of images are shown in Figure 3.6 for 0.1% Xanthan. This is a representative figure which was recorded at 400 frames per second. The flow in this case proceeds from left to right. In Figure 3.6(a)-(k), a turbulent puff is passing the point of observation causing mixing of the tracer particles. This results in a grainy image due to the change in mean orientation, i.e. reflectance, of the tracer particles. In Figure 3.6(k), the trailing edge of the puff is observed, and the flow is once again laminar after the puff has passed. A second example from

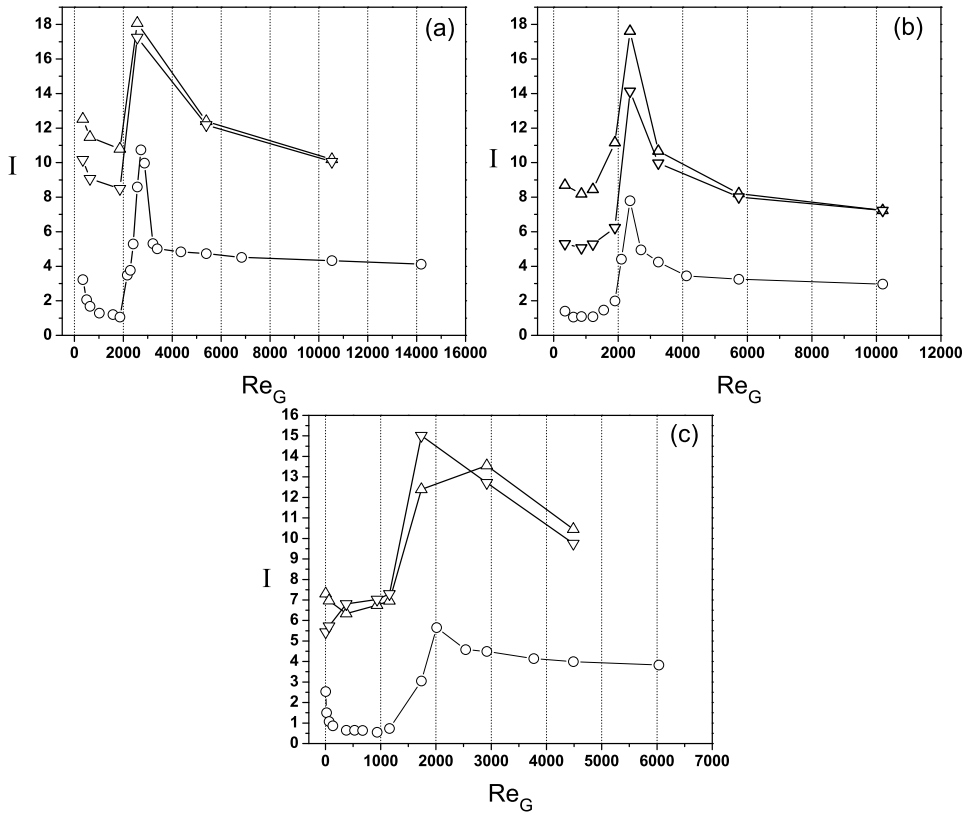

Figure 3.5: Turbulence Intensity at r/R=0 (–○–), r/R=-0.75 (–△–) and r/R=0.75 (–▽–) for (a) 65% glycerin, (b) 0.2% Xanthan gum, (c) 0.1% Carbopol

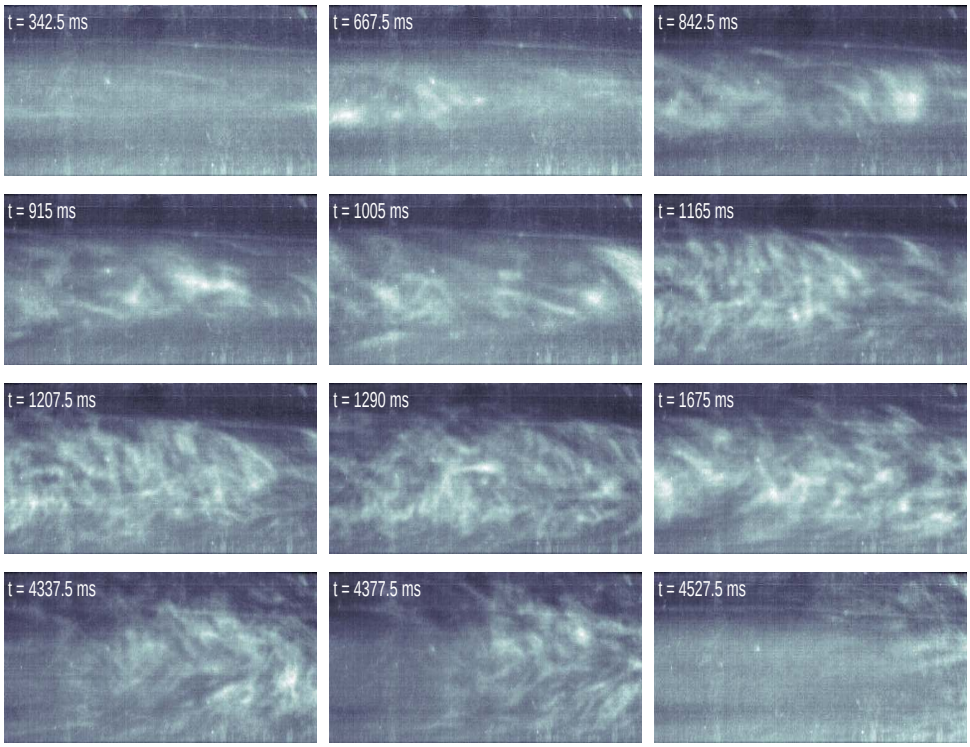

Figure 3.6: Instant puff images taken for 0.1% Xanthan at $Re_G = 2236$ at different time instants.

a Carbopol puff is illustrated in Figure 3.8.

With these images we attempted to characterize the size and velocity of the leading and trailing edges of the puff by an object tracking method. We have also produced space-time plots of the images. Here the images are filtered and the variation of grey-scale intensity at one axial position is reported as a function of time, see Figures 3.10-3.16. What is clear in this sequence of images is that an asymmetry is evident in the Carbopol example. The leading edge of the puff is elongated, in comparison to the Newtonian case, and is located near the wall.

In Table 3.1, we report typical sizes and velocities of puff from these images. For each fluid, around $2 - 4$ puffs are analyzed to produce Table 3.1. With regards to the velocities we report separately the velocities of

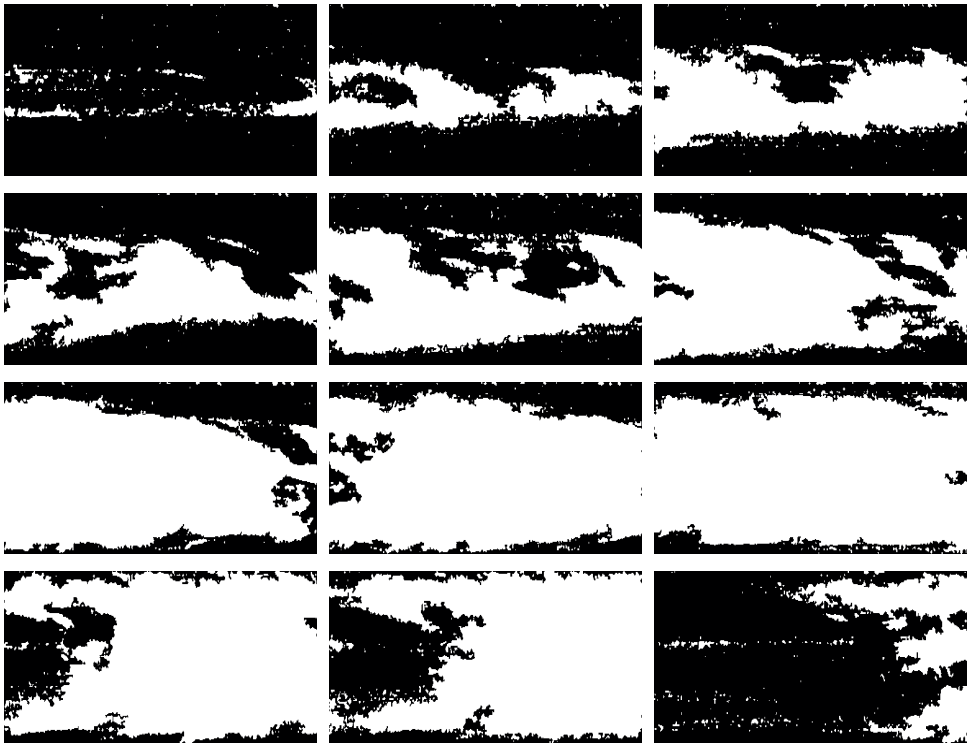

Figure 3.7: Filtered versions of the images in Figure 3.6 for xanthan (%0.1)

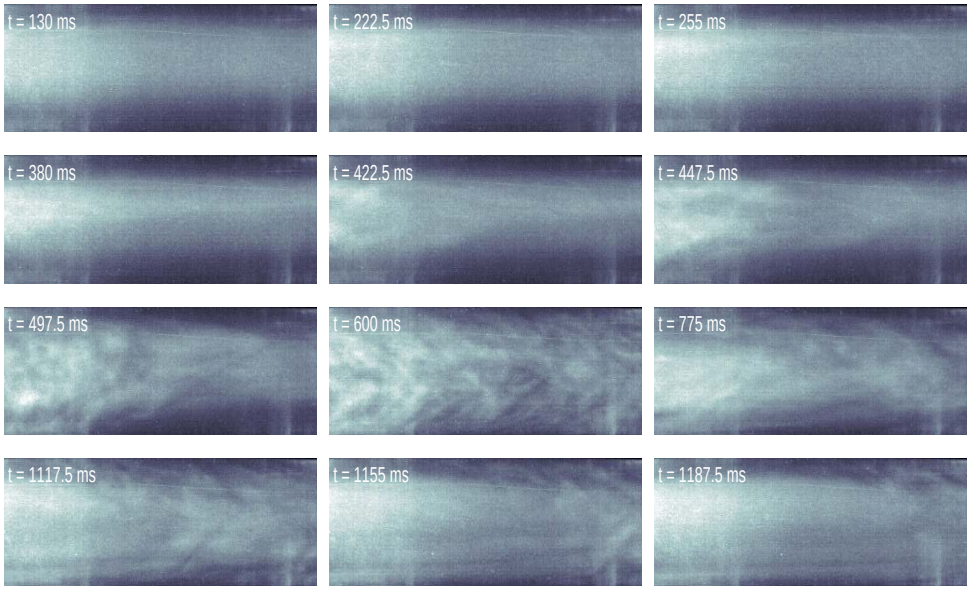

Figure 3.8: Instant puff images taken for 0.075% Carbopol at $Re_G = 1850$ at different time instants.

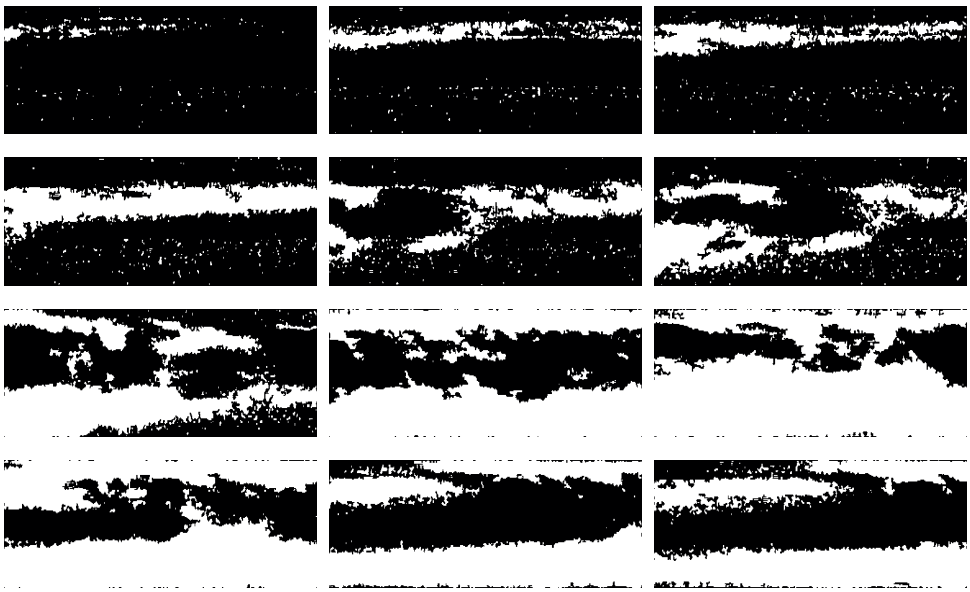

Figure 3.9: Filtered versions of the images in Figure 3.8 for 0.075% Carbopol

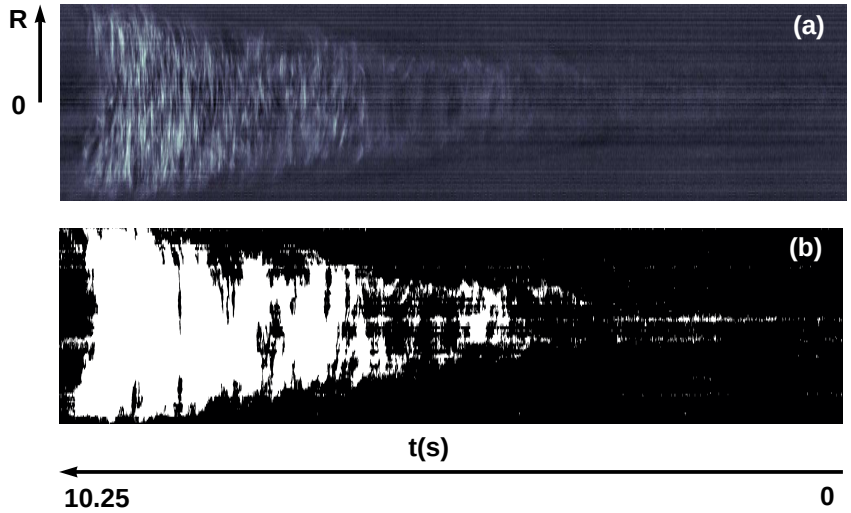

Figure 3.10: Space-time plot for %0.65 Glycerin at $Re_G = 2183$: (a) obtained from raw flow images (b) obtained from filtered, background subtracted and binarized images. The puff length is $\sim 4.35m$. The image sequence consisted of 4100 frames.

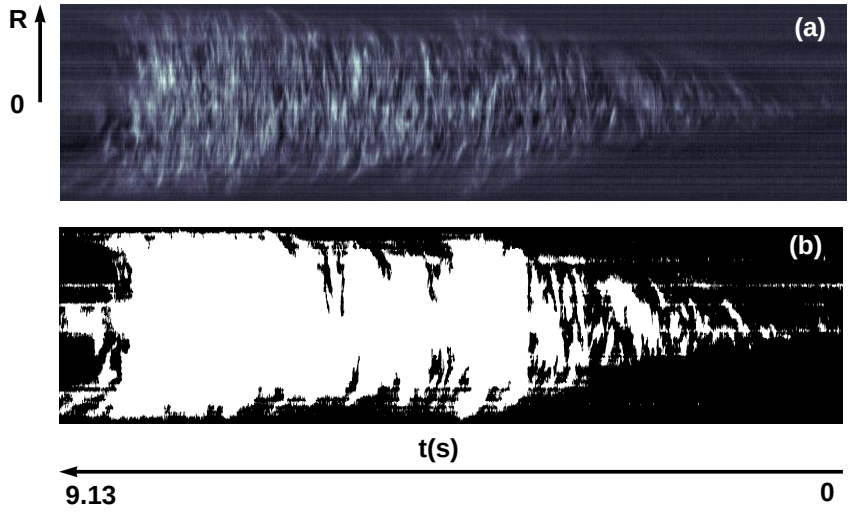

Figure 3.11: Space-time plot for %0.05 Xanthan at $Re_G = 1984$: (a) obtained from raw flow images (b) obtained from filtered, background subtracted and binarized images. The puff length is $\sim 2.5m$. The image sequence consisted of 3650 frames.

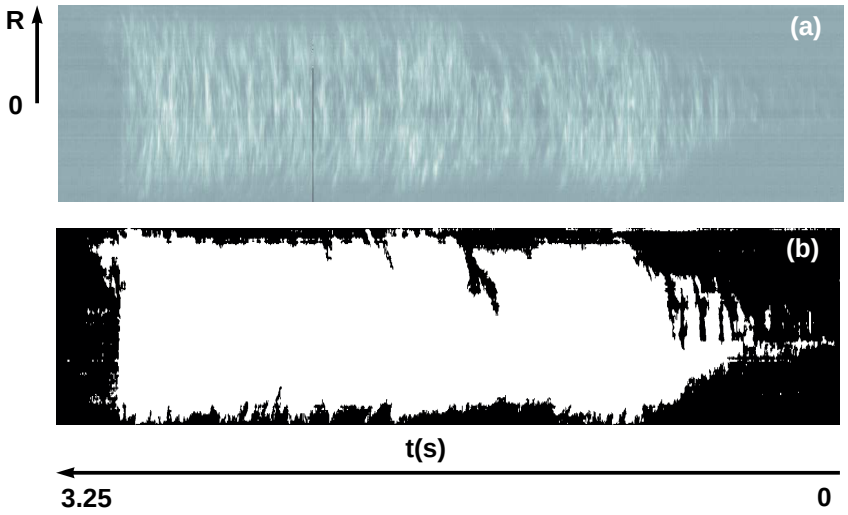

Figure 3.12: Space-time plot for %0.1 Xanthan at $Re_G = 2236$: (a) obtained from raw flow images (b) obtained from filtered, background subtracted and binarized images. The puff length is $\sim 2.63m$. The image sequence consisted of 1300 frames.

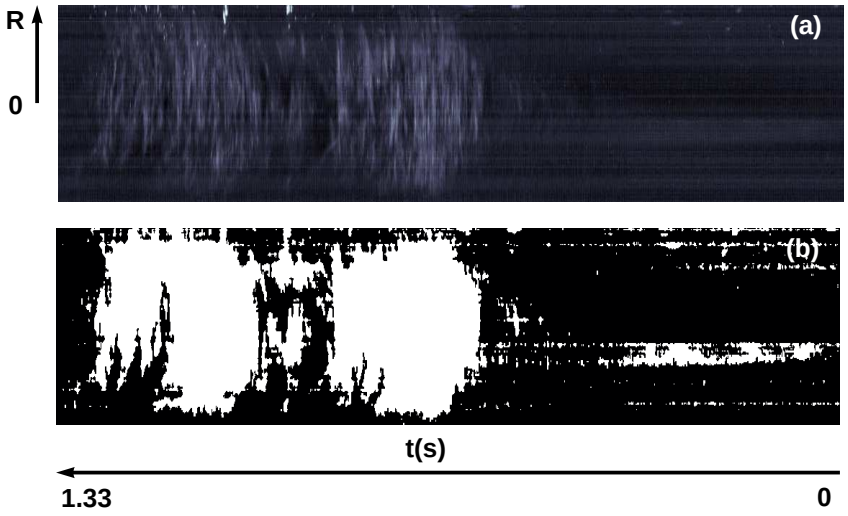

Figure 3.13: Space-time plot for %0.2 Xanthan at $Re_G = 1940$: (a) obtained from raw flow images (b) obtained from filtered, background subtracted and binarized images. The puff length is $\sim 2.37m$. The image sequence consisted of 530 frames. Note that there is a coherent structure here

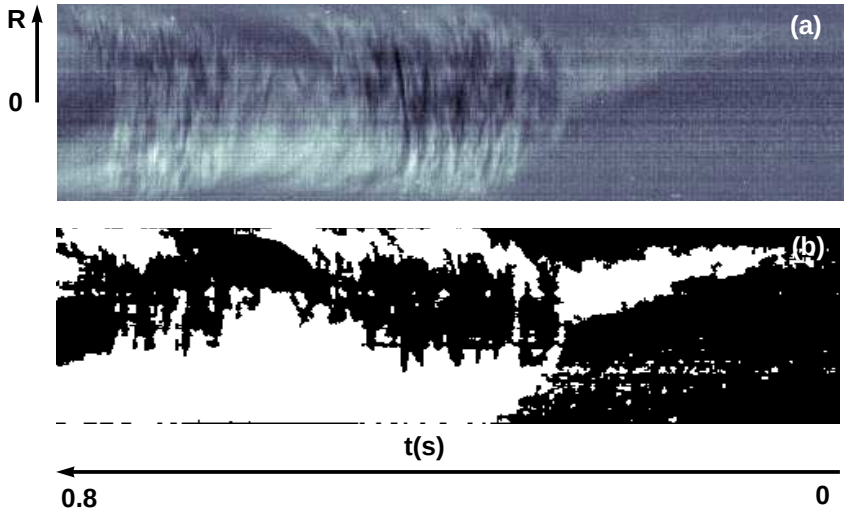

Figure 3.14: Space-time plot for %0.075 Carbopol at $Re_G = 1850$: (a) obtained from raw flow images (b) obtained from filtered, background subtracted and binarized images. The puff length is $\sim 1.69m$. The image sequence consisted of 320 frames.

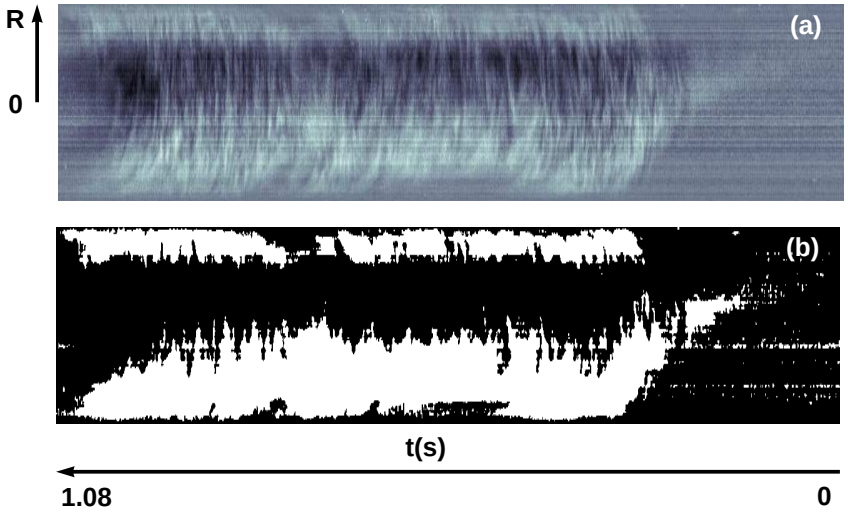

Figure 3.15: Space-time plot for %0.05 Carbopol at $Re_G = 2256$: (a) obtained from raw flow images (b) obtained from filtered, background subtracted and binarized images. The puff length is $\sim 1.39m$. The image sequence consisted of 430 frames.

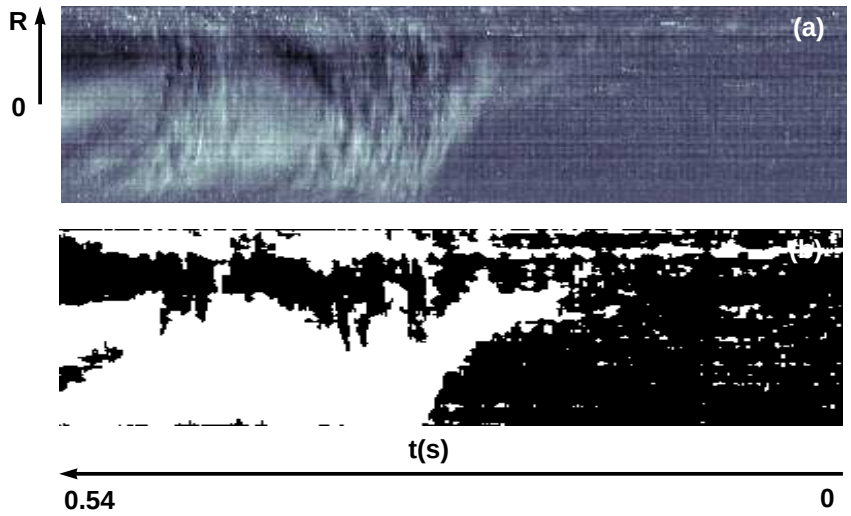

Figure 3.16: Space-time plot for %0.1 Carbopol at $Re_G = 2195$: (a) obtained from raw flow images (b) obtained from filtered, background subtracted and binarized images. The puff length is $\sim 1.64m$. The image sequence consisted of 215 frames.

the leading and the trailing edges. These are measured in three different locations on the edges, namely at $r/R = 0$ and $r/R = \pm 0.75$. The fourth column in Table 3.1 represents the centerline velocity in laminar regime just before the first puff is seen. What is evident from the data is that our estimates of the leading edge velocities for the non-Newtonian fluids are quite comparable to those measured for Glycerin, as well as to those measured for Newtonian fluids by other investigators, (see the summary in Table 1.1). In contrast, the trailing edge velocities for the non-Newtonian fluid appear to be significantly faster than for Newtonian fluids. One possible interpretation of this is that the leading edge propagates by the same mechanism in all these fluids, i.e. controlled by spreading of turbulence structures within the puff, whereas the trailing edge is affected by relaminarisation, and hence the fluid rheology. Regardless of the correctness of this interpretation, the data suggest that puffs in the non-Newtonian fluids will spread axially at a significantly slower rate than in Newtonian fluids. Another observation noted for the Carbopol solutions is that the elongation of the leading edge

Fluid	*Concent.* (wt %)	U_b (m/s)	u_c/U_b	Re_G	U_l/U_b	U_t/U_b	ℓ_{puff}/D
Glycerin	0.65	0.247	2	2143	1.73	0.76	86
Glycerin	0.65	0.252	2	2183	1.77	0.74	86
Glycerin	0.65	0.272	2	2357	1.73	0.74	88
Xanthan	0.05	0.165	1.98	1984	1.77	1.18	49
Xanthan	0.10	0.501	1.92	2236	1.73	1.17	52
Xanthan	0.20	1.185	1.72	1940	1.62	1.18	47
Carbopol	0.05	0.927	1.78	2092	1.56	1.14	30
Carbopol	0.05	0.968	1.78	2256	1.57	1.20	28
Carbopol	0.08	1.514	1.73	1850	1.59	1.22	33
Carbopol	0.08	1.576	1.73	2045	1.61	1.22	32
Carbopol	0.10	2.184	1.69	2038	1.54	1.20	35
Carbopol	0.10	2.266	1.69	2195	1.54	1.22	32

Table 3.1: Puff/Slug characteristics for Glycerin, Xanthan and Carbopol solutions. In this Table we define U_l as the velocity of the leading edge and U_t as the velocity of the trailing edge

gets smaller with decreasing concentrations of Carbopol, i.e. the tip that we see in Figure 3.14 is both reduced and closer to the centreline. It is also worth commenting that since the velocity profiles of shear-thinning fluids are *flatter* than Newtonian profiles, the difference between laminar and fully turbulent centreline velocities is reduced. Hence use of centreline velocity measurements to identify puff/slug occurrence does not give the same distinct "signatures" as for Newtonian fluids. Therefore, rather than distinguishing between puff and slug, we simply use the term puff. Finally we comment that although we have made estimates of puff size, it is difficult to interpret these as it is highly dependent on the location of its origin and the time to the observation point - this is highly variable. We report these values here for completeness.

To summarize our observations, we measured the axial velocity as a function of radial position using LDV of three different classes of fluids under going Hagen-Poiseuille flow. We find that for the non-Newtonian fluids tested there is a persistent asymmetry in the velocity profiles present during

transition. This asymmetry is also seen in RMS profiles. Symmetrical flows were found for both laminar and fully-turbulent cases. These observations were confirmed using high speed imaging. No physical explanation is given at this point. We do, however, attempt to quantify transition more precisely by presenting a more indepth statistical analysis of these results. We do so in the following subsection

3.2 Statistics of weak turbulence

Landau & Lifschitz [82] indicate that turbulent flows are traditionally characterized by random fluid motion in a broad range of temporal and spatial scales. In this section we attempt to characterize these scales using a number of different statistical measures given by Frisch [49]. By doing so we attempt to further characterize the differences in the behaviors of these three classes of fluids during transition.

To begin with, the first statistical measure we use is an autocorrelation function $C(\tau)$ defined by:

$$C(\tau) = \frac{< u(t)u(t+\tau) >_\tau}{u_{rms}^2} \tag{3.1}$$

and determined using the LDV data. This parameter is a measure of the time over which $u(t)$ is correlated with itself. In other words, $C(\tau)$ is bounded by unity as τ approaches zero and zero as $\tau \to \infty$, because a process becomes uncorrelated with itself after a long time. We report the autocorrelation function as a function of Re_G and the radial position in the pipe. Representative results of this curve for the 3 fluids are given in Figures 3.17-3.19. Before we proceed to interpret these figures we must spend some time explaining how the data is represented. Each figure is given as three panels, i.e. at three different radial positions. Within each panel four data sets are presented representing four different Reynolds numbers. The data series labeled (1) and (2) represent laminar flow while (3) is in transition and (4) in turbulence. With regards to (1), which is at the lowest Re_G, in each of the panels the velocity signal is probably dominated by high frequency noise

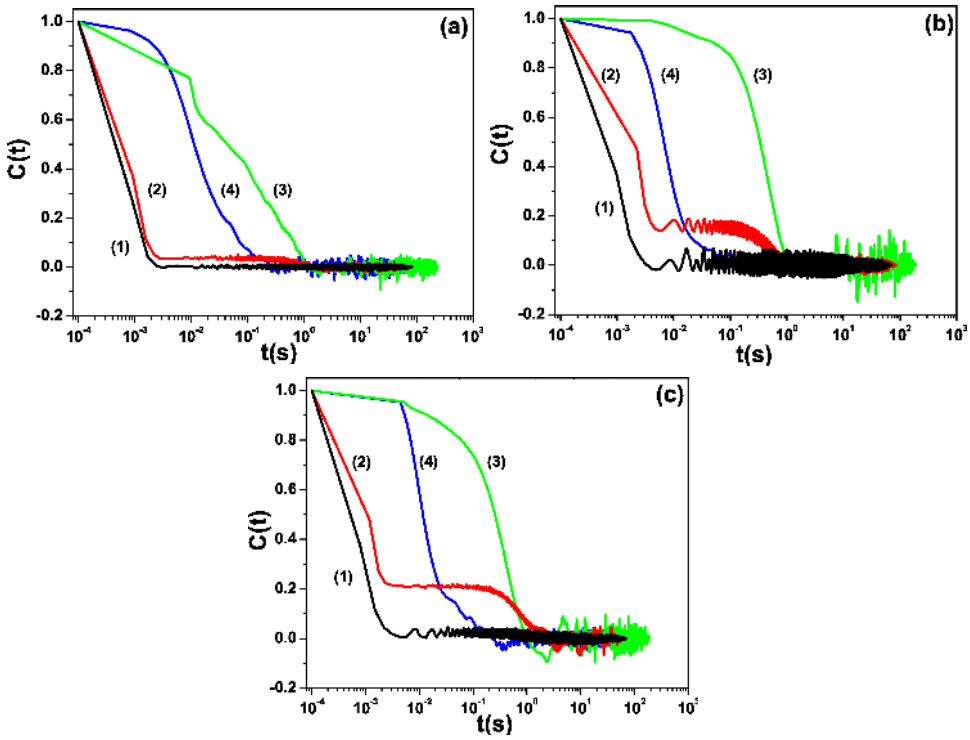

Figure 3.17: Correlation Functions for 80% glycerin solution at three different radial positions(a) $r/R = -0.75$, (b) $r/R = 0$ and (c) $r/R = 0.75$. The data sets are: (**1**) $Re = 1174$, (**2**) $Re = 1737$, (**3**) $Re = 2201$, (**4**) $Re = 3546$.

which results in a fast decay of $C(\tau)$ with a characteristic decay time which we find to be of the order of the inverse data rate of the signal. Proceeding through (4) we find the fully turbulent state characterised by rapid decay of the autocorrelation to the noise level.

A striking difference is found in curve (2) in comparison to the other curves. We observe that there are plateaus in these curves, for some radial positions for each of the fluids, e.g. at $C(\tau) \sim 0.4$ for both $r/R = \pm 0.75$ in the case of the Carbopol solution. Although this data was obtained in a region which we define as laminar, it is clear that there are some weakly correlated structures at this position in the pipe. For the Newtonian fluid, the plateau in the autocorrelation is at a lower value than for the non-

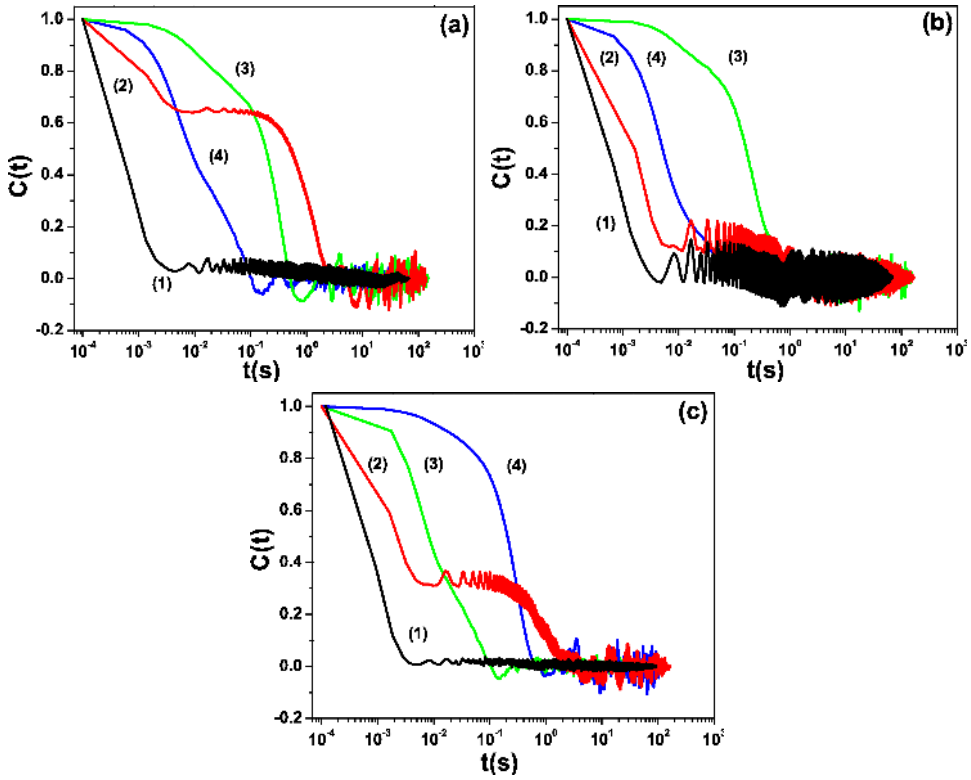

Figure 3.18: Correlation Functions for 0.2% Xanthan solution at three different radial positions:(a) $r/R = -0.75$, (b) $r/R = 0$ and (c) $r/R = 0.75$. The data sets are: (**1**) $Re_G = 858$, (**2**) $Re_G = 1218$, (**3**) $Re_G = 2363$, (**4**) $Re_G = 5736$.

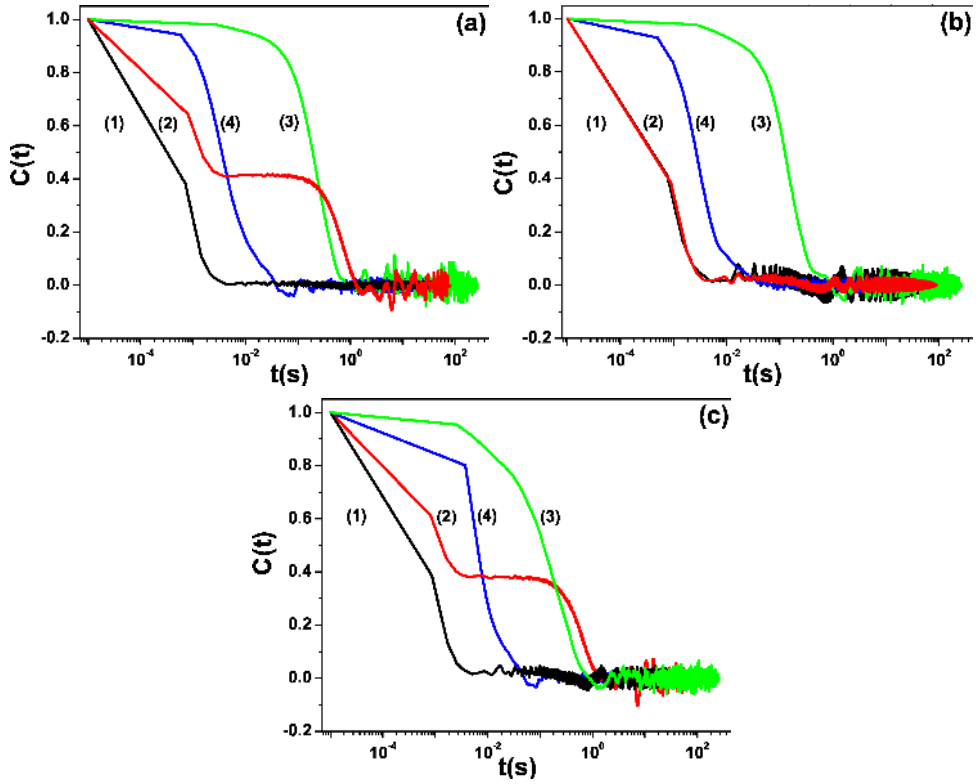

Figure 3.19: Correlation Functions for 0.1% solution Carbopol at three different radial positions (a) r/R=-0.75, (b) r/R=0 and (c) r/R=0.75. The data sets are: (**1**) Re_G = 397, (**2**) Re_G = 914, (**3**) Re_G = 2238, (**4**) Re_G = 3309.

Newtonian fluids and is visible also at the centreline. For the non-Newtonian fluids the plateau is strongly attenuated at the centreline, but evident at the radial positions $r/R = \pm 0.75$. Using Taylor's frozen flow hypothesis (Taylor [132]) we may estimate the axial length-scale of these structures to be $\sim 10^{-1}\, m$, being longer for the Newtonian fluids than for the non-Newtonian fluids. This is significantly lower than the size of the puffs and slugs we report in Table 3.1. We comment also that asymmetry is observed in many of the autocorrelations curves.

The second statistical measure we examined is the probability distribution of the velocity fluctuations. Again we report these results at three different radial positions for a number of Re_G, see Figure 3.20. Like the autocorrelation, we present the data in three panels representing the different radial positions: at each radial position a number of different Re_G numbers are displayed. Each data set (roughly 10^5 velocity events were accounted for in the statistics) is normalized by the maximum count and plotted against the reduced variable, $[u(t) - \bar{U}]/u_{rms}$. Clearly, there is no statistical difference in these probability distributions when compared at different Re_G at similar radial positions, or at different radial positions and with similar Re_G. This finding holds for all classes of fluids tested.

Although intermittent flow behavior is observed during our experiments in both pre-transitional and fully developed turbulent regimes, the physics underlying the two phenomena is substantially different: whereas in the first case it is probably due to the emergence and dynamics of large scale flow structures the second case remains an open problem in fluid dynamics. In order to get a flavor of how Non-Newtonian fluid rheology influences the emergence and magnitude of intermittency, we focus on higher order statistical flow properties for each of the three fluids under study, corresponding to the largest value of Re investigated.

At this point we turn our attention to the main findings in this section, an examination of the intermittency of transitional flow. An intriguing and partially understood feature of inertial turbulent flows is the emergence of intermittency which, simplistically speaking, manifests itself by "rare" velocity bursts. In the case when a complex fluid is used, it is even less

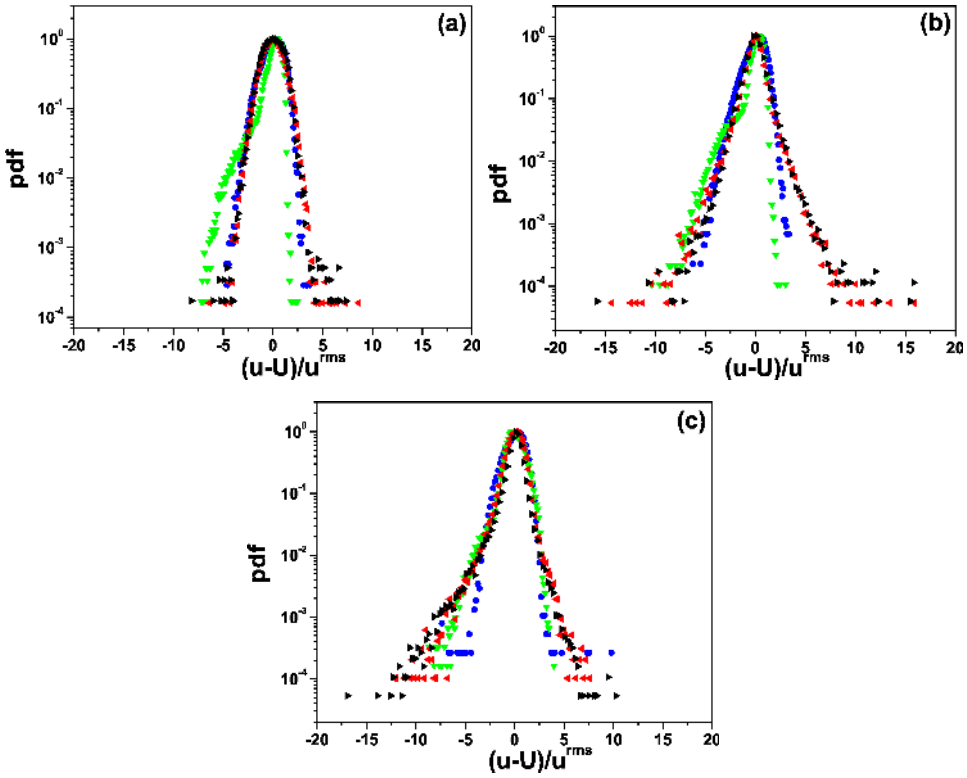

Figure 3.20: Velocity statistics for 0.1% Carbopol solution at three different radial positions (a) $r/R = -0.75$, (b)$r/R = 0$ and (c)$r/R = 0.75$. The symbols are: right triangles (▶) -$Re_G = 397$, left triangles (◀)- $Re_G = 914$,up triangles (▼) - $Re_G = 2238$, circles(●) - $Re_G = 3309$.

well understood how the non-Newtonian fluid rheology influences this phenomenon. Although the signature of this effect is somewhat visible in the tails of the probability distribution functions displayed in Figure 3.20, a more systematic analysis requires the calculation of the velocity structure functions ξ_k, defined by

$$\xi_k(t) = \left\langle |u(\tau + t) - u(\tau)|^k \right\rangle_\tau , \tag{3.2}$$

as given by both [84] and [49]. In a fully developed and homogeneous turbulent flow, the Kolmogorov theory in which intermittency effects are not accounted for predicts

$$\frac{\xi_k}{\xi_3} = \frac{k}{3} \tag{3.3}$$

Thus, the magnitude of the intermittent effects can be quantified by the deviations from the Kolmogorov scaling. In the Newtonian case and in a fully developed turbulent regime the intermittency is highest away from the centerline (see Fig. 3.21) whereas in the non-Newtonian case, the intermittency level is similar at each of the radial positions we have investigated. This finding suggests that in the transitional regime, the yield stress fluid behaves simply as a shear thinning fluid and the effect of the plug at this point should therefore be considered as negligible. Care must be taken when interpreting this figure as we are not in fully turbulent flow. The Kolmogorov scaling is included in this figure for illustrative purposes. The message of this figure is that the structured fluids, according to this statistical measure, behave similarly in transition.

This finding suggests that in the transitional regime, the yield stress fluid behaves simply as a shear thinning fluid and the effect of the plug at this point should be considered negligible. This results from the fact that the size of the plug is below our detection limit.

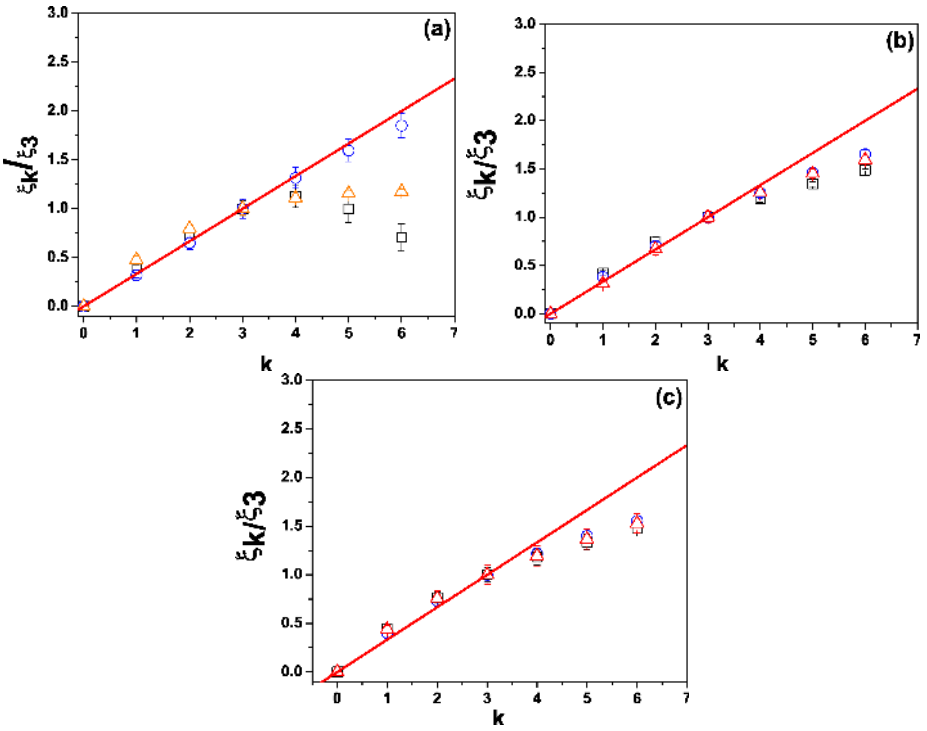

Figure 3.21: Deviations from the Komolgorov scalings for (a) 80% Glycerin at $Re = 3456$, (b) 0.2% Xanthan at $Re = 3513$, and (c) 0.1% Carbopol at $Re = 2612$. The data is displayed at three different radial positions: □-r/R=-0.75, ◯-r/R=0 and △-r/R=0.75.

3.3 Characterizing the plug during transition

For yield stress fluids the role of the plug region in retarding transition is largely unknown. If one interprets the yield stress fluid to be fully rigid below the yield stress then the laminar flow is analogous to that with the plug replaced by a solid cylinder moving at the appropriate speed. Presumably, since the effective viscosity becomes infinite at the yield surface the flow should be locally stabilized. Two different scenarios may be postulated at transition: (i) transition may occur in the yielded annulus around the plug, leaving intact the plug region; (ii) transition is retarded until the plug region thins to such an extent that the Reynolds stresses (in the annular region) can exceed the yield stress.

Scenario (i) is that described in Peixinho [99], Peixinho *et al.* [100], where during the first stage of transition the turbulence intensity level on the centreline is reported as being similar to laminar levels. This is also the scenario assumed explicitly in some phenomenological theories of transition, e.g. Slatter [125] treats the plug as a rigid body in developing his formula for transition.

In Figure 3.22 we present the ratio of averaged Reynolds stress at the centerline (where the level of velocity fluctuations is minimum) to the yield stress, as a function of the generalized Reynolds number, Re_G, for the 4 different Carbopol concentrations that we have used. The filled symbols in Figure 3.22 mark the lowest value of Re_G for which puffs or slugs were detected in the experiments, for each of the different concentrations of Carbopol.

We can observe that the mean Reynolds stress exceeds the yield stress in each case.[2] This suggests to us that the second explanation above is the more plausible, i.e. the plug has broken when transition starts. This is further reinforced by the results of the previous section on the structure functions, i.e. at these transitional/weak turbulent Reynolds numbers we have observed very similar intermittency characteristics with Carbopol, right

[2]This remains true even if we subtract the laminar flow fluctuations from the Reynolds stresses, interpreting them as instrumental noise.

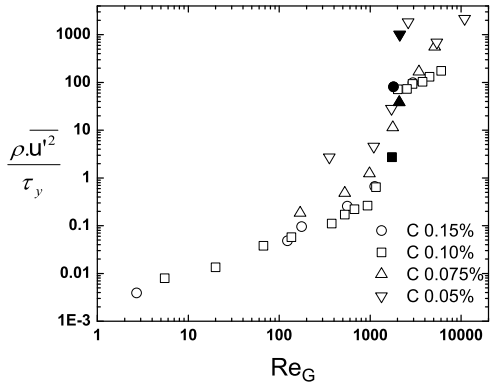

Figure 3.22: Axial Reynolds stresses normalized by yield stress for four different concentration levels of Carbopol. The filled symbols indicate points where the flow becomes transitional, with puffs/slugs first observed

across the pipe radius, as with Xanthan, where there is no yield stress. We should also comment that for the concentrations of Carbopol that we have used, if we calculate the (laminar) un-yielded plug diameters using

$$\frac{r_p}{R} = \frac{2L\tau_y}{R\Delta P} \tag{3.4}$$

where L is the length of the pipe, for the largest flow rates for which puffs or slugs are not detected, see Figure 3.23, these plug diameters are at most of order 2 mm. Thus, we do not anyway have a *strong* plug close to transition.

There is no contradiction with the data from Peixinho [99], Peixinho *et al.* [100], simply with its interpretation. Even with this thinning and break-up of the plug, in the Reynolds number range preceding transition flow instabilities are not sustained. Peixinho *et al.* [100] report measuring low frequency oscillations away from the central region. Such low frequency forcing, presumably with slow axial variation could easily be responsible for slow extensional straining that yields the true plug of the base flow into a pseudo-plug. This type of psuedo-plug also occurs for example in thin film flows, (Balmforth & Craster [5]), and in channels of slowly varying width, (Frigaard & Ryan [48]). In such flows the velocity remains asymptotically

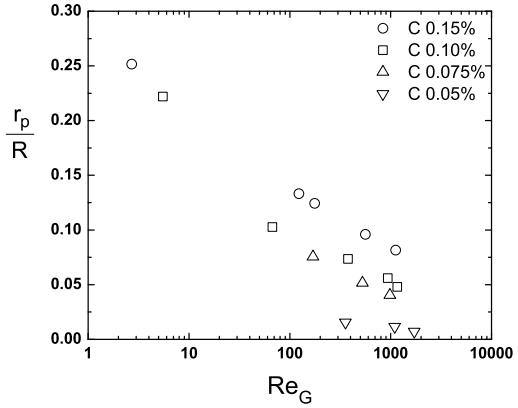

Figure 3.23: Plug radius normalized by pipe radius for four different concentration levels of carbopol

close to the base flow solutions while shear and extensional stresses combine to maintain the pseudo-plug at just above the yield stress. Such flows are laminar but yielded and the psuedo-plug is characterised by large effective viscosity, which would presumably give similar characteristics to the base laminar flow in controlling fluctuation level, as reported in Peixinho [99], Peixinho *et al.* [100]. From our measurements of the velocity profiles, the mean velocity remains plug-like in the centre of the pipe in this upper range of laminar Reynolds numbers and it is simply not possible to discern whether what is observed is a true plug or not.

Evidently the ideal situation would be to visualise transition within a plug region of significant size in comparison to the pipe. Interestingly, this was the intention of our experiments. Our study was started after discussions with C. Nouar about ongoing experiments at LEMTA, Nancy, that were later reported in Peixinho [99], Peixinho *et al.* [100]. These were conducted in a 30 mm pipe at lower speeds, and for the flow rates at which transition occurred the plug region had radius of the order of 1 mm: too small to detect if broken or not. This prompted our interest in the role of the plug during transition, and we therefore designed our experiments at a larger scale so that we could potentially achieve transition with higher yield stress fluids, in larger diameter pipes and at higher speeds, hopefully also with a larger plug

radius at transition. We were apparently defeated in this objective, as the small values of r_p/R in Figure 3.23 indicate. Together with the experiments in Peixinho [99], Peixinho *et al.* [100], our results contribute to the evidence that the plug region must thin to such an extent that the Reynolds stresses can break it, before transition commences.

Chapter 4

Predicting transition

In the previous section we presented a comprehensive comparative study, characterizing the flow of different non-Newtonian fluids in the transitional flow range. The 3 main observations of this study, relevant to prediction of transition are as follows.

- For the complex fluids studied, transition occurs essentially in 2 stages, as also noted by Peixinho *et al.* [100]. The early stage transition is not visible on the pipe axis, where velocity fluctuations remain at approximately laminar levels. Closer to the wall there is a significant increase in turbulent intensity levels. In the second stage of transition there is rapid increase in turbulent intensity at all radial positions.

- Common with other studies, e.g. Escudier *et al.* [42], Peixinho *et al.* [100], some asymmetry is observed in the velocity profiles during transition.

- For yield stress fluids, even though the measured velocity profiles appear to be approximately plug-like at transition, levels of turbulent kinetic energy within the central region of the flow exceed the yield stress value, i.e. the plug is broken before transition occurs.

The first of these observations implies that any simplified predictive method should be based upon essentially local quantities, that vary radially, since for different fluids the position where disturbances first arise may be different.

The second of these observations at first caused some consternation and led to extensive re-calibration and testing of our apparatus, even though observed by other groups. We now believe that the asymmetry observed

is a genuine effect, and is probably a direct observation of coherent traveling wave structures, as are being studied extensively for Newtonian fluid transition by Kerswell and co-workers, Kerswell & Tutty [76], i.e. these are the non-Newtonian analogue, see also recent work by Nouar and co-workers, Esmael & Nouar [43].

The third observation above tends to discount the basis of phenomenological theories such as that of Slatter, Slatter [125], although their predictions may still be reasonable. More succinctly, the premise that the plug region is intact and acts as a rigid solid in the flow, appears from our experiments to be false.

The basis of our criterion consists in defining a local Reynolds number, $Re_{G,l}(r)$ as follows:

$$Re_{G,l}(r) = \frac{\rho u(r) D}{\mu(r)}, \tag{4.1}$$

where $u(r)$ is the axial velocity and $\mu(r)$ is the local viscosity, which depends on r via the rate of strain, $\dot{\gamma}(r)$, ρ is the fluid density and D is the pipe diameter. There are many different ways of interpreting this ratio. Multiplying top and bottom by the velocity gradient leads to the ratio of the gradient of the translational kinetic energy to a representative shear stress gradient. This interpretation of the local Reynolds number is close to the balance parameters postulated by Hanks and by Ryan & Johnson, Hanks [56], Ryan & Johnson [118]. Alternatively we can consider the balance in terms of energy transfer and dissipation.

In flows of shear-thinning fluids we may expect that $u(r) \to 0$ at the wall and $\mu(r) \to \infty$ at the axis. Therefore, $Re_{G,l}(r) = 0$ both at the axis and the wall, with a maximum attained somewhere within the pipe. Unlike Hanks and Ryan & Johnson, we do not consider that transition is defined by the maximal value of $Re_{G,l}(r)$ exceeding a critical parameter, although it is clear that $Re_{G,l}(r)$ will be strongly localised. Instead we suppose that local imbalances in $Re_{G,l}(r)$ will be dissipated across the pipe cross-section. A more appropriate measure for this imbalance is therefore the mean value

of $Re_{G,l}(r)$:

$$Re_G = \frac{2}{R^2}\int_0^R Re_{G,l}(r) r dr, \tag{4.2}$$

where $R = D/2$, the pipe radius.

Evaluation of the averaged Reynolds number is straightforward:

$$Re_G = \frac{4\rho}{R}\int_0^R \frac{u(r)}{\mu(r)} r dr = \frac{4\rho}{R}\int_0^R \frac{u(r)u'(r)}{\tau_{xr}(r)} r dr = \frac{4\rho u_c^2}{R|p_x|}, \tag{4.3}$$

where u_c is the centreline velocity, i.e. for laminar flows we require only the algebraic relationship between the maximal velocity and the frictional pressure gradient. It is also interesting to note that for laminar flows, in which the rheology may be uncertain, u_c and the pressure drop are both easily measurable quantities in a flow loop.

The Darcy friction factor that we use later is defined as follows:

$$f = \frac{8\tau_w}{\rho U_b^2} = \frac{2D|p_x|}{\rho U_b^2}, \tag{4.4}$$

where U is the mean axial velocity. Therefore, we have that

$$Re_G = \frac{16u_c^2}{fU_b^2}. \tag{4.5}$$

For example, for a Newtonian fluid in laminar flow, where we have $u_c = 2U_b$, the local and averaged Reynolds numbers are the same and we recover: $f = 64/Re_G$, as expected.

An alternative interpretation of Re_G is as the radial-average of the quantity $\zeta_G(r) = 2Re_{G,l}(r)r/R$. This dimensionless quantity is directly proportional to that considered by Hanks and by Ryan & Johnson. For a given fluid model and velocity profile it is possible to calculate the radial position at which the integrand $\zeta_G(r) = 2Re_{G,l}(r)r/R$ is maximal and evaluate this maximal value. Thus essentially, our Reynolds number is an averaged version of the Hanks expression, averaged across the radius.

4.1 Application of the Re_G criterion

In this section we demonstrate the utility of this new definition of Re, i.e. equation 4.3, by applying it to the three different classes of fluids studied.

Example 1: Newtonian fluids

For Newtonian fluids, algebraic calculation of the new Reynolds number is straightforward. The velocity is given by

$$u(r) = u_c \left[1 - \left(\frac{r}{R}\right)^2\right] \tag{4.6}$$

where $u_c = 2U_b$, the viscosity is constant and therefore:

$$Re_G = \frac{2}{R^2}\int_0^R \frac{\rho u(r) D}{\mu} r dr = \frac{\rho U_b D}{\mu}. \tag{4.7}$$

Thus, Re_G simplifies to the usual Newtonian Reynolds number for pipe flow, based on the mean velocity and pipe diameter. The local quantity $\zeta_G(r)$ is given by

$$\zeta_G(r) = 2Re_{G,l}(r)\frac{r}{R} = 2\frac{\rho u_c D}{\mu}\frac{r}{R}\left[1 - \left(\frac{r}{R}\right)^2\right] \tag{4.8}$$

The position where $\zeta_G(r)$ is maximum is at:

$$\frac{r}{R} = \frac{1}{\sqrt{3}}, \tag{4.9}$$

which gives maximal value $\zeta_{G,max} \approx 1.54 Re_G$.

Apart from the above calculations, from our LDV measurements of fluid velocity variations in the radial direction, we are able to directly evaluate both $\zeta_G(r)$ and Re_G from the mean velocity profile, i.e. we use local measurements of the mean velocity to define the quantities in $\zeta_G(r)$, and then integrate numerically across the pipe to give Re_G.

As a reference Newtonian fluid we used Glycerin. Figure 4.1 shows example radial profiles of normalised velocity, normalised shear rate, $Re_{G,l}(r)$ and $\zeta_G(r)$ for Glycerin at $Re_G = 2573$. We may observe a slight asym-

$U_b(m/s)$	$\dot{\gamma}(s^{-1})$	$\mu(Pa.s^n)$	Re_G
0.0564	$0.1-8$	0.0096	342
0.1045	$0.2-15$	0.0096	633
0.2943	$0.7-43$	0.0092	1860
0.3894	$0.7-60$	0.0088	2573
0.7791	$2-232$	0.0084	5393
1.4489	$2-482$	0.0082	10531

Table 4.1: Flow Conditions for 65% Glycerin.

metry at transition, as discussed in Escudier *et al.* [42], Esmael & Nouar [43], Peixinho *et al.* [100]. In Fig. 4.1d we can see that $\zeta_G(r)$, calculated from the transitional regime measurements, does indeed exhibit maxima close to the predicted critical position. Table 4.1 gives the flow conditions under which Glycerin was pumped. Note that the viscosity variation in Table 4.1 is due to the temperature increase caused by pumping.

In Fig. 4.2 we examine what happens during transition to both the maximal value of $\zeta_G(r)$ and the critical radial position where $\zeta_G(r)$ achieves its maximum. The analytical expressions for these are given above. To construct this figure we have taken measured mean velocity profiles (symmetrized across the channel), then numerically evaluated these two quantities from the data. Fig. 4.2a shows a comparison between the measured values of critical position of the maximal $\zeta_G(r)$, scaled with Re_G/R, and the analytical prediction. Fig. 4.2b shows a comparison of the measured values of maximal $\zeta_G(r)$ and those predicted analytically. In both figures the solid lines give the values calculated from the laminar flow analytical expressions. In both figures the filled symbols denote experimental values of Re_G for which puffs and slugs were first observed in our experiments. One can notice that there is a deviation from the laminar prediction when transition starts.

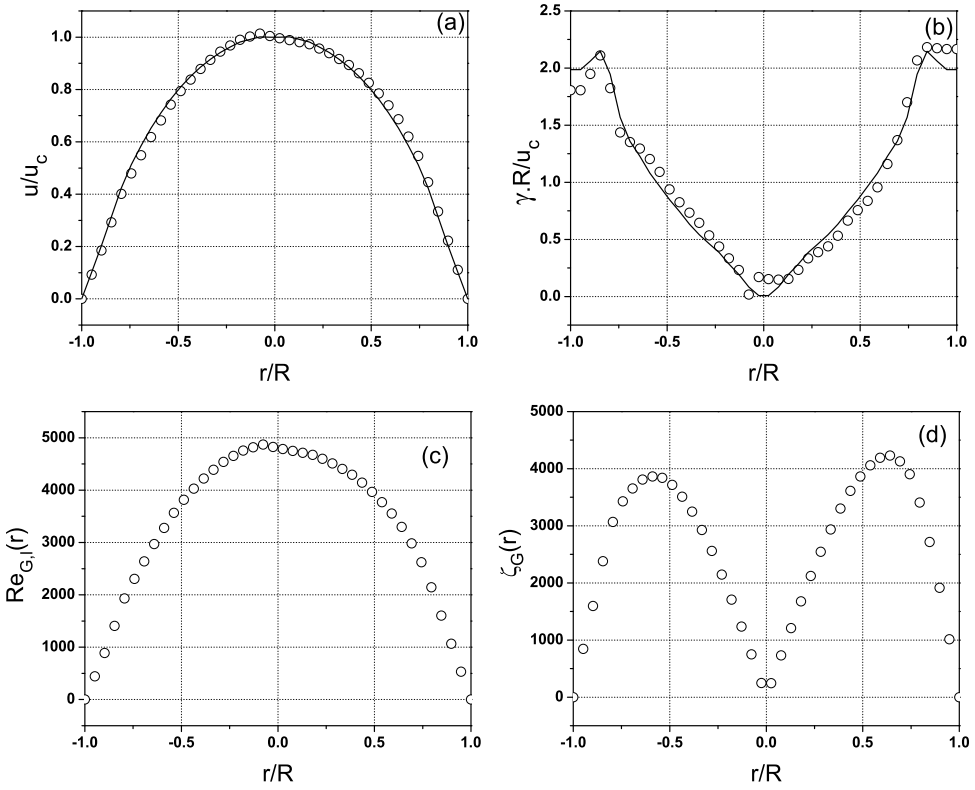

Figure 4.1: a) Mean axial velocity profile for 65% Glycerin (with average data line) at $Re_G = 2573$; (b) Mean shear-rate profile; (c) Reynolds number ($Re_{G,l}(r)$) profile; (d) $\zeta_G(r)$ profile.

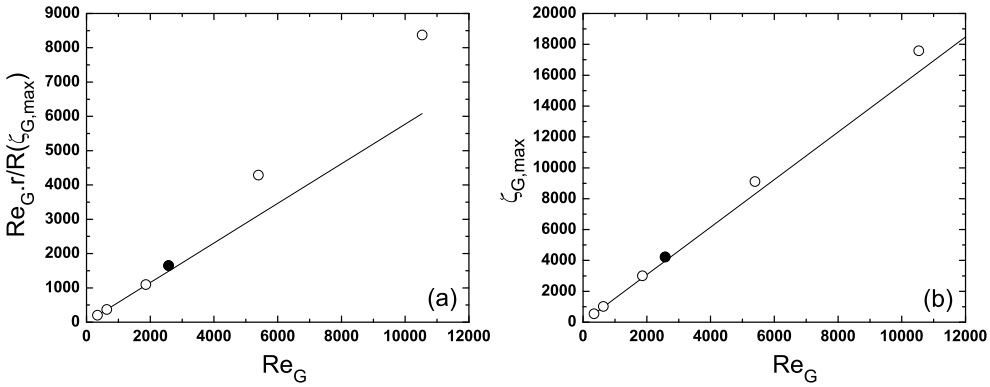

Figure 4.2: a) $Re_G.r/R$ vs. Re_G evaluated at the position r where ζ_G is maximal. (b) $\zeta_{G,max}$ vs. Re_G for 65% Glycerin (solid curves represent theoretical predictions from laminar flow). The filled symbols indicate points where the flow has become transitional, with puffs and slugs appearing.

Example 2: Shear-thinning fluids

Over a given range of shear rates, Xanthan solutions are reasonably well modeled by the power law fluid model, with constitutive law:

$$\tau_{ij} = \kappa \dot{\gamma}^{n-1} \dot{\gamma}_{ij}, \tag{4.10}$$

Here κ is the fluid consistency and n is the power law index. Using this we easily find the Hagen-Poiseuille solution:

$$u(r) = u_c \left[1 - \left(\frac{r}{R} \right)^{m+1} \right], \tag{4.11}$$

where $m = 1/n$, and the radial variation in effective viscosity:

$$\mu(r) = \kappa \left[u_c \left(\frac{n+1}{n} \right) \left(\frac{r^m}{R^{m+1}} \right) \right]^{n-1}. \tag{4.12}$$

The ratio of centreline speed to mean speed of the flow, u_c/U_b is given by:

$$\frac{u_c}{U_b} = \frac{(m+3)}{(m+1)}, \tag{4.13}$$

and we have:

$$Re_G = \frac{2\rho U_b^{2-n} R^n}{\kappa(m+1)^2}\left[\frac{1}{m+3}\right]^{n-2}. \tag{4.14}$$

The localised quantity, $\zeta_G(r)$ is maximised where

$$\frac{r}{R} = \left(\frac{1}{n+2}\right)^{\frac{n}{n+1}}, \tag{4.15}$$

which leads to a maximal value

$$\zeta_{G,max} = 2Re_G \frac{(n+1)^2}{n(n+2)}\left(\frac{1}{n+2}\right)^{\frac{1}{n+1}}. \tag{4.16}$$

We may also calculate the laminar Darcy friction factor f:

$$f = \frac{16}{Re_G}\left[\frac{1+3n}{n+1}\right]^2, \tag{4.17}$$

from which the relationship to the Metzner-Reed Reynolds number, Re_{MR} is easily deduced:

$$\frac{Re_G}{Re_{MR}} = \frac{1}{4}\left[\frac{1+3n}{n+1}\right]^2. \tag{4.18}$$

Regarding experimental verification, Table 4.2 shows the fluid conditions for 0.2% Xanthan from laminar to turbulent regime. The rheological parameters are fitted to fluid samples taken from the flow loop, at each flow rate. The range of shear rates used for the rheological characterisation corresponds to that observed in the flow loop and the flow curves are also measured at the same temperature as the fluid in the flow loop, to account for frictional heating effects. Apart from the effects of temperature and of data fitting from different ranges, Xanthan solutions tend to slightly degrade due to continued pumping and recirculation in the loop. Thus, the rheological constants are different for different experiments. Figure 2.2 gives an example of how different rheological parameters can be found for the same fluid when different ranges of shear rates are used.

Figure 4.3 shows radial profiles of normalised velocity, normalised shear rate, $Re_{G,l}(r)$ and $\zeta_G(r)$ for a 0.2% Xanthan gum ($\kappa = 0.11,\ n = 0.65$)

$U_b(m/s)$	$\dot{\gamma}(s^{-1})$	$\kappa(Pa.s^n)$	n	Re_G
0.2776	$0.2 - 46$	0.11	0.65	352
0.5396	$0.5 - 90$	0.11	0.65	858
0.7163	$0.7 - 137$	0.11	0.65	1218
0.9413	$1 - 224$	0.14	0.56	1900
1.1224	$1 - 270$	0.135	0.56	2363
1.4850	$2 - 501$	0.13	0.56	3244
2.2756	$2 - 835$	0.13	0.56	5736
3.4615	$3 - 1311$	0.13	0.56	10197

Table 4.2: Flow Conditions and rheological parameters for 0.2% Xanthan gum.

during the first stage of transition. We again observe a slight asymmetry in the flow and in Fig. 4.3d we see that the maximal values of $\zeta_G(r)$, have maxima close to the predicted critical positions.

As before, we examine what happens during transition to both the maximal value of $\zeta_G(r)$ and the critical radial position where $\zeta_G(r)$ achieves its maximum. Figure 4.4a shows a comparison between the measured values of critical position of the maximal $\zeta_G(r)$, scaled with Re_G/R, and the analytical prediction. Figure 4.4b shows a comparison of the measured values of maximal $\zeta_G(r)$ and those predicted analytically. The solid lines are the calculated variations from the laminar flow equations and the filled symbols indicate that puffs and slugs were first observed in the experiment at this value of Re_G. In both figures, there is again a deviation from the laminar line when transition starts. The slight inconsistency between the experimental points at transition is due to the size of the incremental steps taken to measure velocity during the experiments, ($1.25mm$ increment between the measuring points).

Example 3: Yield-stress fluids

Our final experiments were conducted using aqueous solutions of Carbopol 940. Over a restricted shear rate range this may be described by the

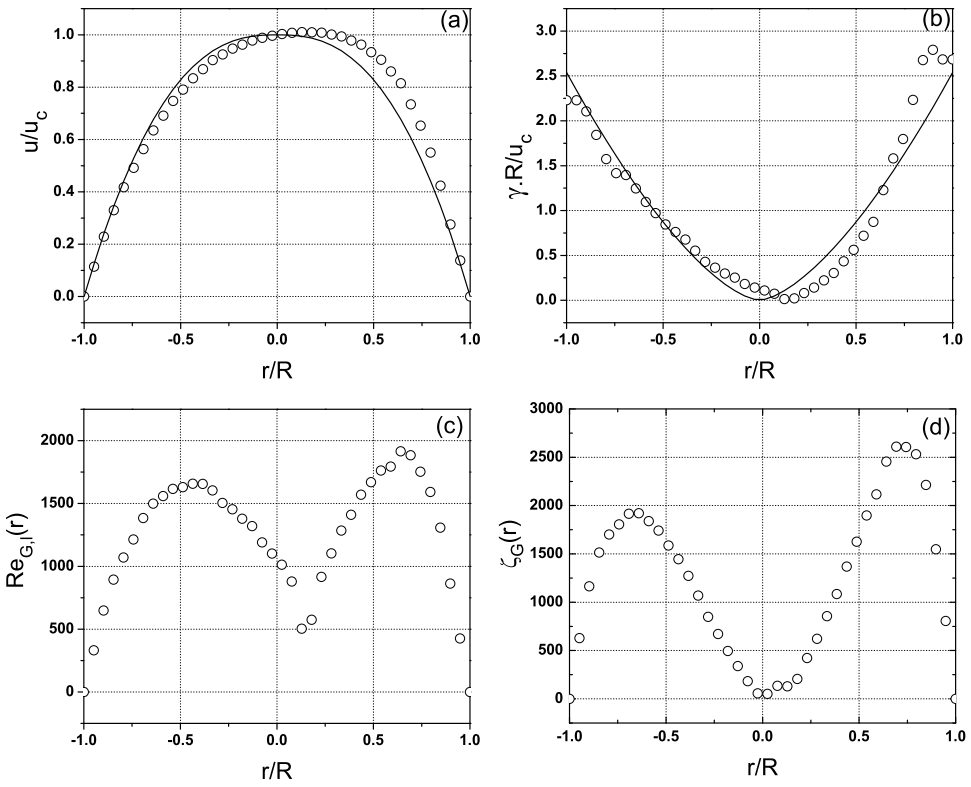

Figure 4.3: a) Mean axial velocity profile for 0.2% Xanthan gum (with laminar profile - solid line) at Re_G=1218, (b) Mean shear-rate profile, (c) Reynolds number ($Re_{G,l}(r)$) profile; (d) $\zeta_G(r)$ profile.

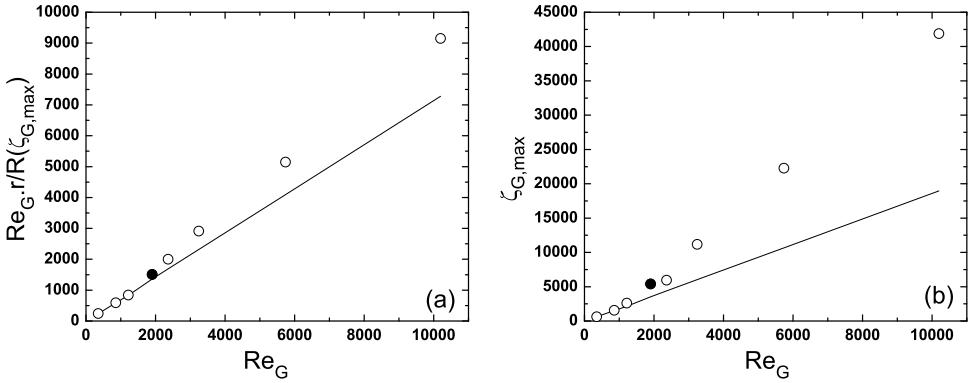

Figure 4.4: a) $Re_G.r/R$ vs. Re_G evaluated at the position r where ζ_G is maximal. (b) $\zeta_{G,max}$ vs. Re_G for 0.2% Xanthan (solid curves represent theoretical predictions made from the laminar flow). The filled symbols indicate points where the flow has become transitional, with puffs and slugs appearing

Herschel-Bulkley fluid model, with constitutive laws:

$$\begin{aligned} \tau_{ij} &= \left[\frac{\tau_y}{\dot{\gamma}} + \kappa(\dot{\gamma})^{n-1}\right]\dot{\gamma}_{ij} \quad \Leftrightarrow \quad \tau > \tau_y, \\ \dot{\gamma}_{ij} &= 0, \quad \Leftrightarrow \quad \tau \leq \tau_y. \end{aligned}$$

The parameter τ_y is referred to as the yield stress. The Poiseuille solution is fully described in terms of the dimensionless yield surface position, $\xi \in [0, 1)$, as follows.

$$u(r) = \begin{cases} u_c & r \in [0, r_p] \\ u_c\left[1 - \left(\dfrac{r - r_p}{R - r_p}\right)^{m+1}\right] & r \in (r_p, R] \end{cases} \tag{4.19}$$

where $r_p = \xi R$ and $m = 1/n$. The dimensionless plug position ξ is the zero of the Buckingham polynomial:

$$0 = \xi^m - B(1-\xi)^{m+1}\left[\frac{(1-\xi)^2}{m+3} + \frac{2\xi(1-\xi)}{m+2} + \frac{\xi^2}{m+1},\right] \tag{4.20}$$

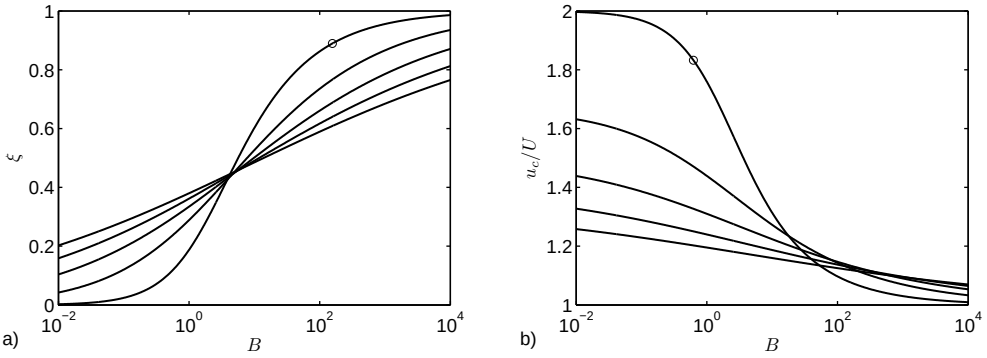

Figure 4.5: a) Variation in the dimensionless plug position $\xi(B, m)$ with B for $m = 1,\ 2,\ 3,\ 4,\ 5$; b) variation in the ratio of centreline (plug) speed to mean speed of the flow, u_c/U_b, with B for $m = 1,\ 2,\ 3,\ 4,\ 5$. Here $m = 1/n$ and the curve for $m = 1$ is marked with a $\circ$.

that lies in the interval $[0, 1)$. Here B is the Bingham number, defined by:

$$B = \left[\frac{\tau_y}{K}\right]^m \frac{R}{U_b}. \tag{4.21}$$

The function $\xi(B, m)$ is computed numerically, see Fig. 4.5a, in a straightforward way. The ratio of centreline (plug) speed to mean speed of the flow, u_c/U_b is given by:

$$\frac{u_c}{U_b} = \frac{(m+2)(m+3)}{2\xi^2 + 2(m+1)\xi + (m+2)(m+1)}, \tag{4.22}$$

see Fig. 4.5b.

From this, after some algebraic manipulation, we have

$$Re_G = \frac{2\rho U_b^{2-n} R^n}{K(m+1)^2}(1-\xi)^{1+n}\left[\frac{(1-\xi)^2}{m+3} + \frac{2\xi(1-\xi)}{m+2} + \frac{\xi^2}{m+1}\right]^{n-2}. \tag{4.23}$$

The localised quantity, $\zeta_G = 2rRe_{G,l}/R$ is maximised where

$$\frac{r}{R} = \xi + (1-\xi)\left(\frac{1}{n+2}\right)^{\frac{n}{n+1}} \tag{4.24}$$

which leads to a maximal value

$$\zeta_{G,max} = \frac{2Re_G}{(1-\xi)}\frac{(n+1)^2}{n(n+2)}\left(\frac{1}{n+2}\right)^{\frac{1}{n+1}}. \tag{4.25}$$

The laminar Darcy friction factor is:

$$f = \frac{16}{Re_G}\left[\frac{(m+2)(m+3)}{2\xi^2+2(m+1)\xi+(m+2)(m+1)}\right]^2, \tag{4.26}$$

from which the relation with Re_{MR} is found:

$$\frac{Re_G}{Re_{MR}} = \frac{1}{4}\left[\frac{(m+2)(m+3)}{2\xi^2+2(m+1)\xi+(m+2)(m+1)}\right]^2, \tag{4.27}$$

which simplifies to the power law and Newtonian expressions when $\tau_y = 0$, $n = 1$, respectively.

It is interesting to note that for the high flow rates and pressure drops that are required to achieve transition with yield stress fluids, the dimensionless plug position typically satisfies $\xi \ll 1$ at transition, so that the above expressions are very close to the power law expressions of the previous section, to which they reduce at $\xi = 0$.

As a yield stress fluid we have conducted experiments with neutralised solutions of Carbopol 940 at various concentrations. The preparation procedure for our experiments is described in § 2, and further characteristics of this fluid are described in Curran *et al.* [24], Kim *et al.* [79]. Table 4.3 shows the fluid conditions for 0.1% Carbopol solution pumped from laminar to turbulent regime. Figure 4.6 shows a sample of the rheological parameter fitting for 0.1% Carbopol. As with the Xanthan solutions, fluid degradation, viscous heating and sensitivity of rheological parameter fitting to shear rate range, all make it necessary to sample the fluid in the flow loop for each flow rate experiment.

Figure 4.7 shows radial profiles of normalised velocity, normalised shear rate, $Re_{G,l}(r)$ and $\zeta_G(r)$ for a 0.1% Carbopol ($\tau_y = 1.3\ Pa$, $\kappa = 1.2\ Pa.s^n$, $n = 0.48$) during the first stage of transition.

Figure 4.8a shows a comparison between the measured values of critical

$U_b(m/s)$	$\dot{\gamma}(s^{-1})$	$\tau_y(Pa)$	$\kappa(Pa.s^n)$	n	$r_p(mm)$	Re_G
0.11202	$0.1-24$	2	2.05	0.36	5.55	5.5
0.4622	$0.1-87$	1.5	2.01	0.40	2.57	67
1.2076	$1-220$	1.4	1.59	0.43	1.84	378
2.0461	$5-414$	1.3	1.20	0.48	1.40	937
2.3218	$5-472$	1.2	0.92	0.53	1.20	1160
3.1146	$5-657$	1	0.65	0.60	–	1735
3.9005	$5-1261$	0.6	0.35	0.65	–	2920
4.3967	$5-1559$	0.4	0.20	0.70	–	4488

Table 4.3: Flow Conditions and rheological parameters for 0.1% Carbopol.

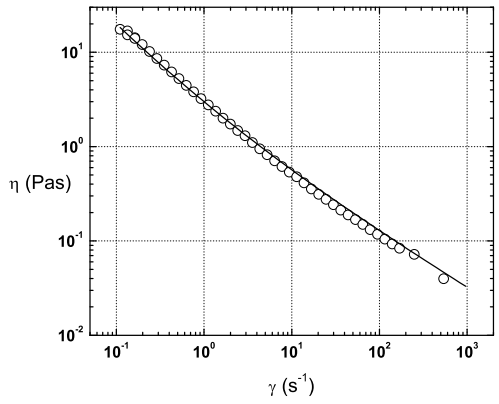

Figure 4.6: Flow curve for 0.1% Carbopol 940, fitted by the Herschel-Bulkley model, $\tau_y = 1.4\ Pa$, $\kappa = 1.59\ Pa.s^n$, $n = 0.43$

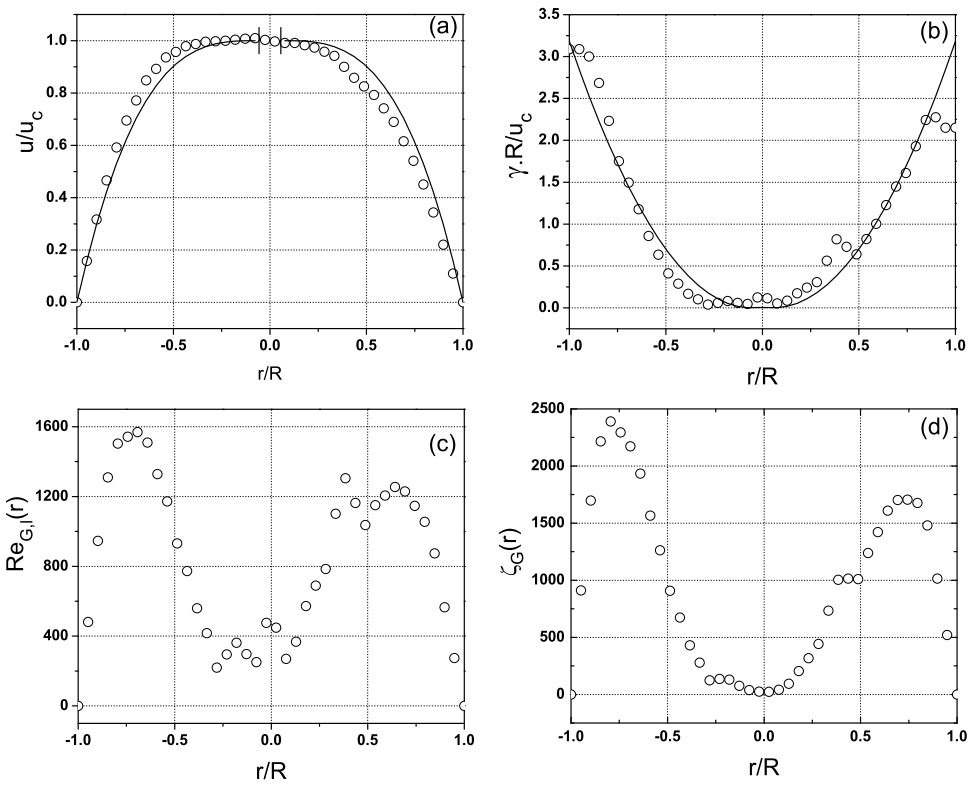

Figure 4.7: a) Mean axial velocity profile for 0.1% Carbopol (with laminar profile - solid line) at Re_G=937, (b) Mean shear-rate profile, (c) Reynolds number ($Re_{G,l}(r)$) profile; (d) $\zeta_G(r)$ profile.

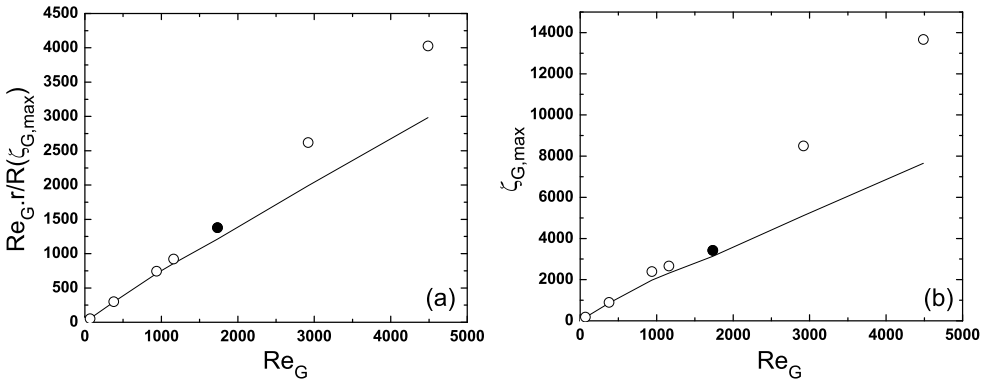

Figure 4.8: a) $Re_G.r/R$ vs. Re_G evaluated at the position r where ζ_G is maximal. (b) $\zeta_{G,max}$ vs. Re_G for 0.1% Carbopol (solid curves represent theoretical laminar curves). The filled symbols indicate points where the flow has become transitional, with puffs and slugs appearing.

position of the maximal $\zeta_G(r)$, scaled with Re_G/R, and the analytical prediction. Figure 4.8b shows a comparison of the measured values of maximal $\zeta_G(r)$ and those predicted analytically. The solid lines are the calculated variations from the laminar flow equations and the filled symbols indicate that puffs and slugs were first observed in the experiment at this value of Re_G. In both figures, there is again a deviation from the laminar line when transition starts. Note that the laminar prediction is not a straight line in these figures since as we have increased Re_G, the best fit to the rheological parameters changes and therefore so do n and r_p.

4.2 Moody diagrams

Figure 4.9 plots the Moody diagram for Glycerin, Carbopol and Xanthan, based on the Reynolds number Re_G. Also plotted are the Newtonian fluid curves for Hagen-Poiseuille flow and the Blasius expression for turbulent flows. In the laminar regime the non-Newtonian data lies below the $f = 64/Re_G$ curve, as predicted by the laminar flow calculations. Transition, identified in the experiments by the onset of puffs and slugs, (see § 3), started at around $Re_G = 2100$.

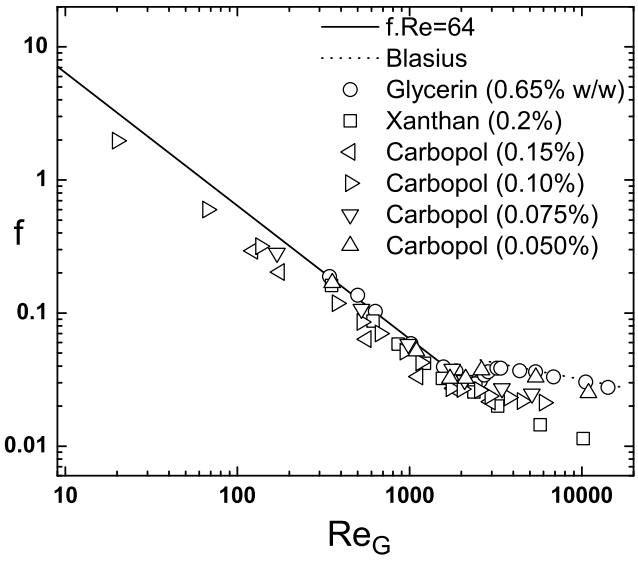

Figure 4.9: Moody diagram plotted against Re_G for 65% Glycerin, 0.2% Xanthan gum and several solutions of Carbopol

Figure 4.10a shows the Moody diagrams plotted against Re_G for the individual fluids treated. For clarity, we have offset each fluid data by a factor of 10. In the turbulent range we plot the Blasius curve($f.Re_G^{(1/4)} = 0.3164$) and in the laminar range we plot the Newtonian curve ($f.Re_G = 64$). We also plot $f.Re_G = 51$ and $f.Re_G = 31$, which correspond approximately to the rheological parameters of the lowest flow rates for Xanthan and Carbopol, respectively. Because these values vary with n and r_p as discussed earlier, (due to viscous heating, fluid degradation and parameter fitting based on different shear rate ranges), the dimensionless parameters n and ξ change with the flow rate, i.e. with Re_G. Thus, it is not feasible to match the experimental data to any single non-Newtonian friction factor curve, (4.17) or (4.26). In Figure 4.10b, we plot f against the localised parameter, $\zeta_{G,max}$, which enables comparison with the criteria of Hanks/Ryan & Johnson. From both these figures we see that the sharp change in f at transition is largely absent for the non-Newtonian fluids.

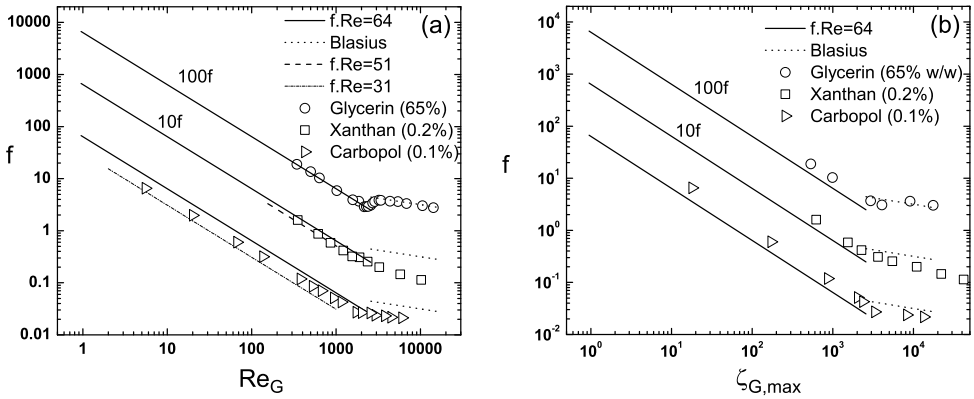

Figure 4.10: Moody Diagrams for 65% Glycerin, 0.2% Xanthan gum and 0.1% Carbopol, (a)with respect to Re_G and (b)with respect to ζ_G, max

Figure 4.11 plots the unit pressure drop vs. velocity. One can notice that the turbulent lines for Xanthan solutions are even lower than the one for water, due to shear-thinning effects. The filled symbols in this figure represent flows that are observed to be transitional, defined by the onset of puffs. This confirms that the transition occurs at approximately where the laminar (Hagen-Poiseuille) line ends and the turbulent (Blasius) lines start.

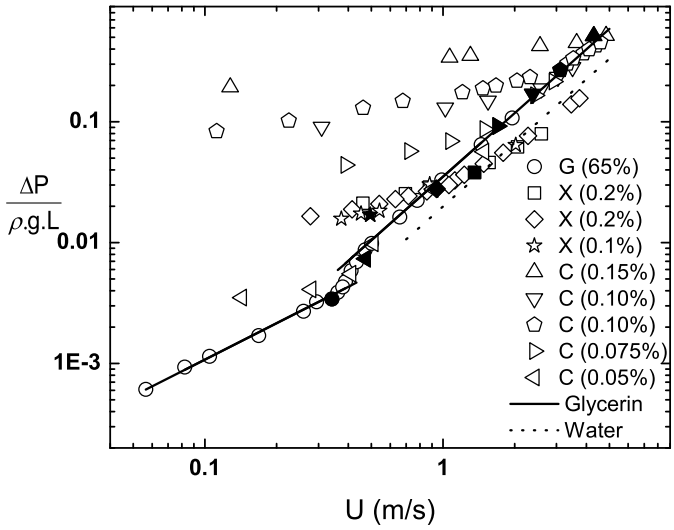

Figure 4.11: Normalized Pressure Drop vs. Mean Velocity for Glycerin and several solutions for Xanthan gum and Carbopol. The solid lines represent Hagen-Poiseuille and Blasius lines for 65% Glycerin and the dashed line Blasius for water. The filled symbols indicate points where the flow has become transitional, with puffs and slugs appearing.

Chapter 5

Summary and conclusions

In this work we measured the instantaneous velocity profiles of fully developed Hagen-Poiseuille flow using three different classes of fluids. The goal of this work was to develop a better understanding of transition in a yield stress fluid.

In §3 of this work we characterized the flow field of the three different fluids and found that during transition, a persistent asymmetry was found both in the time-averaged velocity and in the local u_{rms} profiles. The asymmetry was confirmed by high-speed video imaging of the puffs and slugs from which we observed that the leading edge of the puff is elongated and located off the central axis of the pipe. Our findings are thus consistent with those reported in Escudier *et al.* [42].

Initially we were sceptical about the physical mechanisms creating the asymmetry reported in Escudier *et al.* [42], and about initial observations of the asymmetry in our own apparatus. We thus took all precautions possible to eliminate systematic bias. With regard to the Coriolis suggestions explored in Escudier *et al.* [42], the Eckman numbers in our experiments were also large, Vancouver is at 49.26° North and the flow loop is oriented North-South. We found no evidence therefore to support this idea. In addition to the other potential factors discussed in Escudier *et al.* [42], we considered also whether the optical properties of the fluids could affect the LDV measurements and whether extensional stresses transmitted backwards from the end tank ($\mathbf{R_2}$) could be responsible. Eventually, our scepticism about these asymmetries has been rebuffed - we concur that they appear to be a fluid mechanical phenomenon. Perhaps the strongest evidence for this has come from the systematic and repeatable nature of the phenomena, but also with the asymmetries occurring for different fluids in different parts of the pipe.

In the context of our aim to study transitional phenomena in shear-thinning yield stress fluids, it is worth pointing out that the observed asymmetries have occurred with all structured fluids. Whilst none of these is rheologically perfect as a generalised Newtonian fluid, the different fluids show different degrees of departure from this ideal model, e.g. for Laponite suspensions thixotropy is certainly the dominant feature, apart from the shear rheology, for Xanthan this would be viscoelasticity, etc. Thus, we suggest that it is the commonality of these fluids, i.e. the (largely inelastic) shear-thinning rheological behaviour, that is responsible for the asymmetry.

Recently, Esmael & Nouar [43] have offered an explanation for these asymmetries in terms of the existence of a robust nonlinear coherent structure characterized by two weakly modulated counter-rotating longitudinal vortices in the region (approximately) occupied by the sheared fluid. This explanation seems plausible in the light of recent developments in understanding of Newtonian fluid transition. To support this conclusion, Esmael & Nouar [43] have measured these structures both longitudinally and within the pipe cross-section, showing that there is a slow axial rotation of an otherwise modal structure with one-fold symmetry. The form of traveling wave solution is visually different to those computed for Newtonian fluids by Faisst & Eckhardt [44], Wedin & Kerswell [141], but that should anyway be expected.

We concur with Peixinho [99], Peixinho *et al.* [100] that transition takes place in a different manner than for Newtonian fluids, with a first stage in which the centreline velocity fluctuations are suppressed near to laminar levels while levels nearer the pipe wall increase significantly. The consequence of this is that if rms velocity or turbulence intensity components are to be monitored in order to detect transition, a radial position nearer the wall should be chosen, e.g. here $r/R = 0.75$, or $r/R = 0.8$ as advocated by Escudier *et al.* [40], Park *et al.* [97].

We have reported our findings on characteristics of the puff/slugs, i.e. size and velocity of the leading and trailing edges. For yield stress fluids we have observed that the leading edges can be highly elongated and located off the central axis of the pipe. The other main finding here is that the trailing

edges of puffs appear to move slower for the non-Newtonian fluids than for the Newtonian fluids reported in the literature. The leading edge velocities are similar to those for Newtonian fluids. The consequence of this is that puffs will spread slower in the axial direction as they travel along a pipe. We have not made a distinction in our work between puffs and slugs, referring simply to them all as puffs. This is because some distinguishing features in Newtonian fluids, e.g. the "signature" changes in centreline velocity, are simply less clear for shear-thinning yield stress fluids. For such fluids the laminar and turbulent velocity profiles are closer to each other, meaning that abrupt changes in centreline velocity are reduced; see also Park *et al.* [97], Peixinho *et al.* [100].

We have also attempted to further characterize transition by examining both an autocorrelation function and a probability distribution function of the velocity fluctuations. The autocorrelation function shows some differences between the fluids, indicates weakly coherent unsteady structures located away from the axis in the non-Newtonian fluids, and also indicates asymmetry. This occurs at Reynolds number that are high, but are still lower than we would normally expect for transition. For Newtonian fluids there is recent work on recurrent traveling waves at Reynolds numbers in these ranges, e.g. Kerswell & Tutty [78]. Whilst our data may correspond to a non-Newtonian version of such structures, we have no strong evidence and prefer to leave the interpretation open to the reader. For the probability distribution functions there were no significant differences between the different classes of fluids examined.

Of more interest was the third statistical measure of the fluid we used, namely a structure function, in which we found that in transitional flow, the shear-thinning and yield stress fluids behaved somewhat similarly. This was the first indication that in transitional flow, the effect of the plug was minimal on the flow structure. In §3 we have presented evidence that as transition occurs the plug actually thins to an extent where the Reynolds stresses are sufficient to break it.

In addition, we have defined a new Reynolds number, Re_G, obtained from averaging across the pipe a localised Reynolds number, $Re_{G,l}(r)$. Al-

ternatively, this can be interpreted as a radial average of a function $\zeta_G(r) = 2rRe_{G,l}(r)/R$. The function $\zeta_G(r)$ is simply a scaled version of the local parameters ζ and ζ_H, introduced by Ryan & Johnson [118] and by Hanks [56], respectively. By measuring the mean velocity profiles and evaluating $\zeta_G(r)$ from the data, we have demonstrated that the maximal value of $\zeta_G(r)$ and the radial location of the maximum, both deviate from their predicted positions as transition occurs. As transition occurs, the regions of maximal $\zeta_G(r)$ appear to correspond approximately to the positions of maximal turbulence intensity. Instead of the localised criterion of Ryan & Johnson or Hanks, we have preferred to use the averaged quantity Re_G. Physically, we believe that although the basis of transition is evidenced via local phenomena, local imbalances will be to some extent dissipated. In averaging $\zeta_G(r)$ with respect to r, it is noteworthy that the principal contributions in any case will come from a range of r close to the maximal position. Thus, apart from actual numerical values the use of Re_G or the maximal local quantity is not very different. An advantage of using Re_G is that the expression is easy to evaluate from flow loop data.

The use of our Re_G appears to give transitional flows in the range $Re_G \approx 2100$, with some variation. Since transitional Reynolds numbers depend largely on the flow loop design, this simply gives an indication of the noise level in our loop. For this reason we have avoided specifically stating any *transition criterion* in terms of Re_G. Due to the local effects captured in Re_G, we believe Re_G is an appropriate number to use for quantifying transition, more so than for example the Metzner-Reed Reynolds number, which is based on extrapolating the laminar friction factor. On the other hand, use of Re_G for friction factor calculations is more cumbersome.

5.1 Contributions to knowledge

The significant findings in this study are as follows:

1. We find that for yield-stress shear thinning fluids the plug is broken before transition occurs. In transition the non-Newtonian fluids behave

somewhat similarly.

2. Transition occurs when the turbulent kinetic energy within the central region of the flow exceeds the yield stress of the fluid.

3. We have defined Reynolds number in a novel manner in which it can be evaluated without any rheological information of the fluid. With this definition we find that transition occurred at approximately $Re_G \approx 2100$ for all fluids tested. This new definition of Reynolds number brings simplicity and universality for practicing engineers in designing pipe lines for non-Newtonian fluids.

4. A persistent asymmetry in the velocity profile was found during transition and the observed puff and slugs were elongated and located off the central axis for the non-Newtonian fluids.

5.2 Future work

There are a number of experimental issues which should be addressed before this work is continued. The primary recommendation is to remove the downstream reservoir, labeled R2 in Figure 2.1, and allow the flow to discharge into the atmosphere. The reason for this is that we are unsure of the flow state in the reservoir and uncertain of the perturbations this may cause in laminar flow. Once this is corrected, it is recommended that further insight into the behaviour of puffs and slugs is warranted. In particular, a further study should be conducted in which Particle Image Velocimetry (PIV) should be used to visualize the flow patterns within the puff and slug.

Bibliography

[1] M. A. Abbas & C.T. Crowe 1987 Experimental study of the flow properties of a homogeneous slurry near transitional Reynolds numbers. *Int. J. Multiphase Flow.*, **13**(3), pp. 357-364

[2] B.J. Abu-Ghannam & R. Shah 1980 Natural Transition of Boundary Layers - the Effects of Turbulence, Pressure Gradient, and Flow History *J. Mech. Eng. Sci.*, **22**, pp.213

[3] E. De Angelis, C.M. Casciola & R. Piva 2002 DNS of wall turbulence: dilute polymers and self-sustaining mechanisms *Comput. Fluids*, **31**, pp. 495-507

[4] I.S. Aranson & L. Kramer 2002 The world of the complex GinzburgLandau equation *Rev. Mod. Phys.*, **74**, pp. 99-143

[5] N.J. Balmforth & R.V. Craster 1999 A consistent thin-layer theory for Bingham plastics *J. non-Newt. Fluid Mech.*, **84**, pp. 65–81

[6] B. Bamieh & M. Dahleh 1999 Disturbance Energy Amplification in Three-Dimensional Channel Flows *AACC*, pp. 4532-4537

[7] B. Bamieh & M. Dahleh 2001 Energy amplification in channel flows with stochastic excitation *Physics of Fluids*, **13(11)**, pp. 3258-3269

[8] P.R. Bandyopadhyay 1986 Aspects of the equilibrium puff in transitional pipe flow *J. Fluid Mech.*, **163**, pp. 439-458

[9] H.A. Barnes & Q.D. Nguyen 2001 Rotating vane rheometry - a review *J. non-Newt. Fluid Mech.*, **98**, pp. 1-14

[10] G. Ben-Dov & J. Cohen 2007 Critical Reynolds Number for a Natural Transition to Turbulence in Pipe Flows *Phys. Rev. Lett.*, **98**, pp. 064503

[11] L.B. Bergstrom 2003 Transient growth of small disturbances in a Jeffrey fluid flowing through a pipe *Fluid Dynamics Research* , **32**, pp. 29-44

[12] N.S. Berman 1978 Drag Reduction by Polymers *Ann. Rev. Fluid Mech.*, **10**, pp. 47-64

[13] H.W. Bewersdorff 1991 Turbulence structure of dilute polymer and surfactant solutions in artificially roughened pipes *In 6th European Drag Reduction Working Meeting, Eindhoven University of Technology*

[14] R.B. Bird, R.C. Armstrong & O. Hassager Dynamics of polymeric liquids, volume 1: fluid mechanics *Wiley*, **1987**

[15] L. Boberg & U. Brosa 1988 Onset of turbulence in a pipe *Z. Naturforsch A*, **43**, pp. 697726

[16] D.C. Bogue 1959 Entrance effects and prediction of turbulence in non-Newtonian flow *Ind. Eng. Chem.*, **51**, pp. 874-878

[17] T. Bohr & D.A. Rand 1991 A mechanism for localized turbulence *Physica*, , pp. 532-543

[18] F. Brand, J. Peixinho & C. Nouar 2001 A Quantitative Investigation of the Laminar-to-Turbulent Transition: Application to Efficient Mud Cleaning *SPE 71375*

[19] M.H. Buschmann & M. Gad-el-Hak 2005 New Mixing-Length Approach for the Mean Velocity Profile of Turbulent Boundary Layers *J. of Fluids Eng.*, **127**, pp. 393-396

[20] S.J. Chapman 2002 Subcritical transition in channel flows. *J. Fluid Mech.*, **451**, pp. 35-97

[21] R.Y. Chen 1973 Flow in the Entrance Region at Low Reynolds Numbers *J. Fluids Eng.*, **95**, pp.153-158

[22] R.M. Clapp 1961 Turbulent heat transfer in pseudoplastic non-Newtonian fluids *Int. Develop. in Heat Transfer*, **111A**, pp. 652-661

[23] M.E. Crawford & W.M. Kays 1976 STAN5 - A Program for Numerical Computation of Two-Dimensional Internal and External Boundary Layer Flows *NASA CR-2742*

[24] S.J. Curran & R.E. Hayes & A. Afacan & M.C. Williams & P.A. Tanguy 2002 Properties of Carbopol Solutions as Models for Yield-Stress Fluids. *J. Food Science*, **67**, pp. 176-180

[25] A.G. Darbyshire & T. Mullin 1995 Transition to turbulence in contant-mass-flux pipe flow. *J. Fluid Mech.*, **289**, pp. 83-114

[26] A. Davey & P.G. Drazin 1969 The stability of Poiseuille flow in a pipe *J. Fluid Mech.*, **36**, pp. 209-218

[27] R.J. Deissler 1987 Spatially growing waves, intermittency, and convective chaos in an open-flow system *Physica*, **25D**, pp. 233-260

[28] S.E.D.M. Desouky & M.N. Al-Awad 1998 A new laminar-to-turbulent transition criterion for yield-pseudoplastic fluids *J. Petroleum Sci. & Eng.*, **19**, pp. 171-176

[29] D.W. Dodge & A.B. Metzner 1959 Turbulent flow of non-Newtonian systems *A.I.Ch.E. Journal*, **5**, pp. 189-204

[30] J. Doherty, P.Ngan, J. Monty & M. Chong 2007 The development of turbulent pipe flow *16th Australasian Fluid Mechanics Conference*, pp. 266-270

[31] A.A. Draad & J. Westerweel 1996 Measurement of temporal and spatial evolution of transitional pipe flow with PIV *Presentation at the meeting of the APS, Fluid Mechanics Section, University of Buffalo, NY*, **1996**

[32] A.A. Draad & F.T.M. Nieuwstadt 1998 The Earth's rotation and laminar pipe flow *J. Fluid Mech.*, **361**, pp. 297-308

[33] A.A. Draad, G.D.C. Kuiken & F.T.M. Nieuwstadt 1998 Laminar-turbulent transition in pipe flow for Newtonian and non-Newtonian fluids *J. Fluid Mech.*, **377**, pp. 267-312

[34] P.G. Drazin & W.H. Reid 1981 Hydrodynamic Stability *Cambridge University Press, Cambridge*

[35] E.R. van Driest 1956 On Turbulent Flow Near a Wall *J. Aeronaut. Sci.*, **23**, pp. 1007-1011

[36] F. Durst, S. Ray, B. Unsal & O.A. Bayoumi 2005 The Development Lengths of Laminar Pipe and Channel Flows *J. Fluids Eng*, **127**, pp. 1154-1160

[37] S. Eliahou, A. Tumin & I. Wygnanski 1998 Laminar-turbulent transition in Poiseuille pipe flow subjected to periodic perturbation emanating from the wall *J. Fluid Mech.*, **361**, pp. 333-349

[38] B. Eckhardt,T. Schneider,B. Hof & J. Westerweel 1998 Turbulence transition in pipe flow *Annu. Rev. Fluid Mech.*, **39**, pp. 447468

[39] M.P. Escudier & F. Presti 1996 Pipe flow of a thixotropic liquid *J. non-Newt. Fluid Mech.*, **62**, pp. 291306

[40] M.P. Escudier, F. Presti & F. Smith 1999 Drag reduction in the turbulent pipe flow of polymers *J. non-Newt. Fluid Mech.*, **81**, pp. 197-213

[41] M.P. Escudier, I.W. Gouldson, A.S. Pereira, F.T. Pinho & R.J. Poole 2001 On the reproducibility of the rheology of shear-thinning liquids *J. non-Newt. Fluid Mech.*, **97**, pp. 99124

[42] M.P. Escudier, R.J. Poole, F. Presti, C. Dales, C. Nouar, C. Desaubry, L. Graham & L. Pullum 2005 Observations of asymmetrical flow behaviour in transitional pipe flow of yield-stress and other shear-thinning liquids *J. non-Newt. Fluid Mech.*, **127**, pp. 143-155

[43] A. Esmael & C. Nouar 2008 Transitional flow of a yield stress fluid in a pipe: Evidence of a robustc oherent structure preprint submitted to *Phys. Rev. E*, privately communicated

[44] H. Faisst & B. Eckhardt 2003 Travelling waves in pipe flow *Phys. Rev. Lett.*, **91**, 224502

[45] A.C. Fowler & P.D. Howell 2003 Intermittency in the transition to turbulence *SIAM J. APPL. MATH*, **63-4**, pp. 1184-1207

[46] I.A. Frigaard, S.D. Howison & I.J. Sobey, 1994 On the stability of Poiseuille flow of a Bingham fluid *J. Fluid Mech.*, **263**, pp. 133-150

[47] I.A. Frigaard & C. Nouar, 2003 On three-dimensional linear stability of Poiseuille flow of Bingham fluids *Phys. Fluids*, **15**, pp. 28432851

[48] I.A. Frigaard & D.P. Ryan 2004 Flow of a visco-plastic fluid in a channel of slowly varying width *J. non-Newt. Fluid Mech.*, **123**, pp. 67–83

[49] U. Frisch Turbulence: The legacy of A. N. Kolmogorov *Cambridge University Press*, **1995**

[50] G. B. Froishteter & G. V. Vinogradov 1980 The laminar flow of plastic disperse systems in circular tubes *Rheol. Acta.*, **19**, pp. 239-250

[51] K. Gasljevic, G. Aguilar & E.F. Matthys 2007 Measurement of temperature profiles in turbulent pipe flow of polymer and surfactant drag-reducing solutions *Phys. Fluids*, **19**, 083105 pp. 1-18

[52] G.W. Govier & K. Aziz 1972 The flow of complex mixtures in pipes *Van Nostrand-Reinhold, NY*, **1972**

[53] B. Guo, K. Sun & A. Ghalambor 2004 A Closed-Form Hydraulics Equation for Aerated-Mud Drilling in Inclined Wells. *SPE Drilling & Completion*, **19**(2), pp. 72-81

[54] J.M. Hamilton, J. Kim & F. Waleffe 1995 Regenaration mechanism of near-wall turbulence structures *J. Fluid Mech.*, **287**, pp. 317-348

[55] G. Han, A. Tumin & I. Wygnanski 2000 Laminar-turbulent transition in Poiseuille pipe flow subjected to periodic perturbation emanating from the wall.Part 2.Late stage of transition. *J. Fluid Mech.*, **419**, pp. 1-27

[56] R. W. Hanks 1963a The Laminar-Turbulent Transition for Fluids with a Yield Stress. *A.I.Ch.E. Journal*, **9**, pp. 306-309

[57] R. W. Hanks 1963b The Laminar-Turbulent Transition for Flow in Pipes, Concentric Annuli, and Parallel Plates. *A.I.Ch.E. Journal*, **9**, pp. 45-48

[58] R.W. Hanks & D.R. Pratt 1967 On the flow of Bingham Plastic Slurries in Pipes and Between Parallel Plates. *SPE paper number*, 1682.

[59] R. W. Hanks 1968 On the Theoretical Calculation of Friction Factors for Laminar, Transitional, and Turbulent Flow of Newtonian Fluids in Pipes and Between Parallel Plane Walls. *A.I.Ch.E. Journal*, **14**, pp. 691-695

[60] R. W. Hanks 1969 A theory of laminar flow stability. *A.I.Ch.E. Journal*, **15 (1)**, pp. 25-28

[61] R. W. Hanks & B.H. Dadia 1971 Theoretical Analysis of the Turbulent Flow of Non-Newtonian Slurries in Pipes. *A.I.Ch.E. Journal*, **17**, pp. 554-557

[62] R. W. Hanks & B.L. Ricks 1974 Laminar-Turbulent Transition in Flow of Pseudoplastic Fluids with Yield Stresses. *Journal of Hydronautics*, **8**, pp. 163-166

[63] A.M. Hecht 1972 A Turbulent Mixing Length Formulation for Non-Newtonian Power Law Fluids *J. HYDRONAUTICS*, **6**, pp. 21

[64] B. O. A. Hedström 1952 Flow of plastic materials in pipes. *Ind. Eng. Chem.*, **44 (3)**, pp. 652-656

[65] B. Hof A. Juel & T. Mullin 2003 Scaling of the turbulence transition threshold in a pipe *Phys. Rev. Lett.*, **91**, pp. 244502-1-4

[66] B. Hof, C.W.H. vanDoorne, J. Westerweel, F.T.M. Nieuwstadt, H. Faisst, B. Eckhardt, H. Wedin, R.R. Kerswell & F. Waleffe 2004 Experimental observation of nonlinear traveling waves in turbulent pipe flow *Science*, **305**, pp. 1594-1598

[67] B. Hof, C.W.H. vanDoorne, J. Westerweel & F.T.M. Nieuwstadt 2005 Turbulence regeneration in pipe flow at moderate Reynolds numbers *Phys. Rev. Lett.*, **95**, 214502

[68] B. Hof 2005 Transition to turbulence in pipe flow. in Laminar Turbulent Transition and Finite Amplitude Solutions, T. Mullin and R.R. Kerswell (eds), Springer (2005), pp. 221-231.

[69] R.P. Hornby, J. Mistry & H. Barrow 1977 A Mixing Length Model for Turbulent Flow in Constant Cross Section Ducts *Warme- und Stoffubertragung*, **10**, pp. 125-129

[70] J. Laufer 1952 The structure of turbulence in fully developed pipe flow *National Advisory Committee of Aeronautics, USA*, **Report number 1174**

[71] O. C. Jones 1976 An improvement in the calculation of turbulent friction in rectangular ducts. *ASME, Jour. Fluids Engineering*, **96**, pp. 173-181

[72] O. C. Jones 1981 An improvement in the calculation of turbulent friction in smooth concentric annuli. *ASME, Jour. Fluids Engineering*, **103**, pp. 615-623

[73] T. von Karman 1934 Turbulence and Skin Friction *J. of Aeronautical Sci.*, **1**, pp. 1-20

[74] H. Kanda 2008 Calculation of minimum critical Reynolds number for laminar-turbulent transition in pipe flows *Elect. Transact. on Numerical Analysis, Kent State Uni.*, **30**, pp. 168-186

[75] H. Kanda & T. Yanagiya 2008 Hysteresis Curve in Reproduction of Reynolds Color-Band Experiments *J. Fluids Engineering*, **130**, pp. 051202

[76] RR. Kerswell & O.R. Tutty 2004 Exact coherent solutions in pipe flow: Travelling wave solutions. *J. Fluid Mech.*, **508**, pp. 333-371

[77] R. R. Kerswell 2005 Recent progress in understanding the transition to turbulence in a pipe *Nonlinearity*, **18**, R17-R44

[78] R.R. Kerswell & O.R. Tutty 2007 Recurrence of travelling waves in transitional pipe flow. *J. Fluid Mech.*, **584**, pp. 69-102

[79] J.Y. Kim, J.Y. Song, E.J. Lee & S.K. Park 2003 Rheological properties and microstructures of Carbopol gel network system. *Colloid Polym. Sci.*, **281**, pp. 614-623

[80] M. Kostic & J. P. Hartnett 1984 Predicting turbulent friction factors of non newtonian fluids in non circular ducts. *Int. Comm. Heat Mass Transfer*, **11**, pp. 345-352

[81] W. Kozicki, C. Chou & C. Tiou 1966 Non-Newtonian flow in ducts of arbitrary cross-sectional shape. *Chem. Engineering Science*, **21**, pp. 665-679

[82] L. D. Landau & E. M. Lifschitz Fluid mechanics *Pergamon Press, Oxford*, **1987**

[83] C.X. Lin & M.A. Ebadian 2008 A numerical study of developing slurry flow in the entrance region of a horizontal pipe *Computers & Fluids*, **37**, pp. 965-974

[84] M. Lesieur 1990 Turbulence in Fluids Stochastic and Numerical Modelling (Fluid Mechanics and Its Applications) *Springer; 2nd rev. ed. edition*

[85] G. Lu & H.W. Jun 1998 Diffusion studies of methotrexate in Carbopol and Poloxamer gels *Int. J. Pharmaceutics*, **160**, pp. 1-9

[86] R.E. Mayle 1991 The Role of Laminar-Turbulent Transition in Gas Turbine Engines *J. Turbomachinery*, **113**, pp. 509

[87] F. Mellibovsky & A. Meseguer 2005 Global finite amplitude perturbations in medium aspect ratio pipe flow *J. Physics: Conference Series*, **14**, pp. 192-2005

[88] F. Mellibovsky & A. Meseguer 2007 Pipe flow transition threshold following localized impulsive perturbations *Phys. of Fluids*, **19**, pp. 044102

[89] C. Métivier, C. Nouar, and J.-P. Brancher 2005 Linear stability involving the Bingham model when the yield stress approaches zero *Phys. of Fluids*, **17**, pp. 104106

[90] A.B. Metzner & J.C. Reed 1955 Flow of Non-Newtonian Fluids - Correlation of the Laminar, Transition and Turbulent-flow Regions *A.I.Ch.E. Journal*, **1**, pp. 434-440

[91] P. Mishra & G. Tripathi 1971 Transition from Laminar to Turbulent Flow of Purely Viscous non-Newtonian fluids in Tubes. *Chem. Eng. Science*, **26**, pp. 915-921

[92] Q. D. Nguyen & D. V. Boger 1985 Direct yield stress measurement with the vane method *J. Rheol.*, **29**, pp. 335-347

[93] N.V. Nikitin 1994 Direct numerical modeling of three-dimensional turbulent flows in pipes of circular cross section *Fluid Dyn.*, **29**, pp. 749

[94] J. Nikuradse 1932 Gesetzmassigkeiten der turbulenten stromung in glatten rohren, Forschung auf dem Gebiet des Ingenieurwesens *Translated in NASA TT F-10, 359, 1966*, **3**, pp.1-36

[95] C. Nouar & I.A. Frigaard 2001 Nonlinear stability of Poiseuille flow of a Bingham fluid *J. non-Newt. Fluid Mech.*, **100**, pp. 127-149

[96] C. Nouar, N. Kabouya, J. Dusek & M. Mamou 2007 Modal and non-modal linear stability of the plane BinghamPoiseuille flow *J. Fluid Mech.*, **577**, pp. 211-239

[97] J.T. Park, R.J. Mannheimer, T.A. Grimley & T.B. Morrow 1989 Pipe flow measurements of a transparent non-Newtonian slurry. *ASME Journal of Fluids Engineering.*, **111**(3), pp. 331-336

[98] N.A. Park & T.F. Irvine 1996 Anomalous viscosity-temperature behavior of aqueous Carbopol solutions *J. Rheol.*, **41**(1), pp. 167-173

[99] J. Peixinho 2004 Contribution expérimentale à l'étude de la convection thermique en régime laminaire, transitoire et turbulent

pour un fluide à seuil en écoulement dans une conduite *PhD thesis*, Université Henri Poincaré, Nancy, France

[100] J. Peixinho, C. Nouar, C. Desaubry & B. Theron 2005 Laminar transitional and turbulent flow of yield-stress fluid in a pipe *J. non-Newt. Fluid Mech.*, **128**, pp. 172-184

[101] J. Peixinho, C. Desaubry & M. Lebouche 2008 Heat transfer of a non-Newtonian fluid (Carbopol aqueous solution) in transitional pipe flow *I. J. Heat and Mass Trans.*, **51**, pp. 198-209

[102] C.W. Pernell, E.A. Foegeding & C.R. Daubert 2000 Measurement of the Yield Stress of Protein Foams by Vane Rheometry *J. Food Sci.*, **65**, pp. 110-114

[103] A.E. Perry & C.J. Abell 1978 Scaling laws for pipe-flow turbulence *J. Fluid Mech.*, **67**, pp. 257-271

[104] A.A. Pilehvari & R.W. Serth 2005 Generalized Hydraulic Calculation Method Using Rational Polynomial Model *J. Energy Resources Tech.*, **127**, pp. 15-25

[105] F.T. Pinho & J.H. Whitelaw 1990 Flow of non-Newtonian fluids in a pipe *J. non-Newt. Fluid Mech.*, **34-2**, pp. 129-144

[106] R.J. Poole & B. S. Ridley 2007 Development-Length Requirements for Fully Developed Laminar Pipe Flow of Inelastic Non-Newtonian Liquids *J. Fluids Eng.*, **129**, pp. 1281-1287

[107] V.G. Priymak & T. Miyazaki 2004 Direct numerical simulation of equilibrium spatially localized structures in pipe flow *Phys. Fluids*, **16**, pp. 4221

[108] L. Prandtl 1925 Bericht ber Untersuchungen zur ausgebildeten Turbulenz *Z. Angew. Math. Mech*, **5**, pp. 136-139

[109] S.C. Reddy, P.J. Schmid & D.S. Henningson 1993 Pseudospectra of the Orr-Sommerfeld operator *SIAM J. Appl. Maths*, **53**, pp. 15-47

[110] T. D. Reed & A. A. Pilehvari 1993 A New Model for Laminar, Transitional and Turbulent Flow of Drilling Fluids. *Society of Petroleum Engineers*, SPE **25456**

[111] J. Reuter & D. Rempfer 2004 Analysis of pipe flow transition. Part 1. Direct numerical simulation *Theor. Comput. Fluid Dyn.*, **17**, pp. 273

[112] O. Reynolds 1883 An experimental investigation of the circumstances which determine whether the motion of water shall be direct or sinuous, and the law of resistance in parallel channels *Phil. Trans. R. Soc. Lond*, **174**, pp. 935-982

[113] A. Roshko 2000 On the problem of turbulence *Current Science*, **79**, pp. 834-839

[114] M. Rudman & H.M. Blackburn 1999 Large eddy simulation of turbulent pipe flow *P. of the Second Int. Conf. on CFD in the Minerals and Process Ind., Melbourne*

[115] M. Rudman, L.J.W. Graham, H.M. Blackburn & L. Pullum 2002 Non-Newtonian turbulent and transitional pipe flow. *Hydrotransport*, **15**, Banff.

[116] M. Rudman, H.M. Blackburn, L.J.W. Graham & L. Pullum 2004 Turbulent pipe flow of shear-thinning fluids *J. non-Newt. Fluid Mech.*, **118**, pp. 33-48

[117] M. Rudman & H.M. Blackburn 2006 Direct numerical simulation of turbulent non-Newtonian flow using a spectral element method *Applied Mathematical Modelling*, **30**, pp. 1229-1248

[118] N. W. Ryan & M. M. Johnson 1959 Transition from Laminar to Turbulent Flow in Pipes. *A.I.Ch.E. Journal*, **5**, pp. 433-435

[119] A.W. Saak, H.M. Jennings & S.P. Shah 2001 The influence of wall slip on yield stress and viscoelastic measurements of cement paste *J. Cement and Concrete Research*, **31**, pp. 205-212

[120] P.J. Schmid & D.S. Henningson 2001 Stability and Transition in Shear Flows *Springer, New York*

[121] P.J. Schmid & D.S. Henningson & D.F. Jankowski 2002 Stability and transition in shear flows *Applied Mechanics Reviews*, **55**, B57-B59

[122] S.N. Shah & D.L. Sutton 1990 New Friction Correlation for Cements From Pipe and Rotational-Viscometer Data. *SPE Prod. Engng.*, **5**(4), pp. 415-424

[123] H. Shan, Z. Zhang & F.T.M. Nieuwstadt 1998 Direct numerical simulation of transition in pipe flow under the influence of wall disturbances *Int. J. Heat and Fluid Flow*, **19**, pp. 320-325

[124] H. Shan, B. Ma, Z. Zhang & F.T.M. Nieuwstadt 1999 Direct numerical simulation of a puff and a slug in transitional cylindrical pipe flow *J. Fluid Mech.*, **387**, pp. 39-60

[125] P.T. Slatter 1999 The laminar-turbulent transition in large pipes in Int. Conf. Problems in Fluid Mechanics and Hydrology, Prague, pp. 247-256

[126] P.T. Slatter & E.J. Wasp 2000 The laminar-turbulent transition in large pipes in Proceedings of 10th International Conference on Transport and Sedimentation of Solid Particles, Wroclaw, Poland, pp. 389-399

[127] M. Sourlier 1988 Contribution à l'étude des propriétés convectives de fluides thermodépendants. Cas de l'écoulement en canal de section rectangulaire. Ph.D Thesis, Université de Nancy I

[128] R.J. Soto & V.L. Shah 1976 Entrance Flow of a Yield-Power Law Fluid *Appl. Sci. Res.*, **32**, pp. 73-85

[129] K. Stewartson & J.T. Stuart 1971 A non-linear instability theory for a wave system in plane Poiseuille flow *J. Fluid Mech.*, **48**, pp. 529-545

[130] R. Sureskumar, A.N. Beris & A.H. Handler 1997 Direct numerical simulation of the turbulent channel flow of a polymer solution *Phys. Fluids*, **9**, pp. 743-755

[131] G. I. Taylor 1932 The Transport of Vorticity and Heat through Fluids in Turbulent Motion *Proc. R. Soc. London, Ser. A*, **135**, pp. 685-702

[132] G. I. Taylor 1938 The spectrum of turbulence *Proc. R. Soc. London, Ser. A*, **164**, pp. 476

[133] R. Teitgen 1980 Laminar-turbulent transition in pipe flow:development and structure of the turbulent slug *Laminar-Turbulent Transition, IUTAM Symposium, Stuttgart, Germany*, **1979**, pp. 27-36 Springer

[134] A.D. Thomas & K.C. Wilson A new analysis of non-Newtonian turbulent flow-yield power law fluids. *Can. J. Chem. Eng.*, **65**, pp. 335-338

[135] J.M.J. Toonder & F.T.M. Nieuwstadt 1997 Reynolds number effects in a turbulent pipe flow for low to moderate *Re Phys. of Fluids*, **9**, pp. 3398-3409

[136] L.N. Trefethen, A.E. Trefethen, A.E. Reddy & T.A. Driscoll 1993 Hydrodynamic stability without eigenvalues *Science*, **261**, pp. 578-584

[137] A.E. Trefethen, L.N. Trefethen & P.J. Schmid 1999 Spectra and pseudospectra for pipe Poiseuille flow *Comput. Methods Appl. Mech. Eng.*, **1926**, pp. 413-420

[138] R.M. Turian, T.W. Ma, F.L.G. Hsu & D.J. Sung 1998 Experimental study of the flow properties of a homogeneous slurry near transitional Reynolds numbers. *Int. J. Multiphase Flow.*, **13**(3), pp. 357-364

[139] M.A. Valdez, L. Yeomans, F. Montes, H. Acuna, & A. Ayala 1995 Influence of temperature on the slip velocity of semidilute xanthan gum solutions *Rheol. Acta*, **34**, pp. 474-482

[140] F. Waleffe 1997 On a self-sustaining mechanism in shear flows *Phys. of Fluids*, **9**, pp. 883-900

[141] H. Wedin & R.R. Kerswell 2004 Exact coherent solutions in pipe flow: Travelling wave solutions. *J. Fluid Mech.*, **508**, pp. 333-371

[142] F.M. White 1991 Viscous Fluid Flow *McGraw-Hill; 2nd edition, New York*, pp. 369-370

[143] F.M. White 1999 Fluid Mechanics *McGraw-Hill; 4th edition*

[144] C.M. White & M.G. Mungal 2008 Mechanics and Prediction of Turbulent Drag Reduction with Polymer Additives *Ann. Rev. Fluid Mech.*, **40**, pp. 235-256

[145] K.C. Wilson & A.D. Thomas 1985 A new analysis of the turbulent flow of non-Newtonian fluids *Can. J. Chem. Engng.*, **63**, pp. 539-546

[146] K.C. Wilson & A.D. Thomas 2006 Analytic model of laminar-turbulent transition for Bingham plastics *Can. J. Chem. Engng.*, **84**(5), pp. 520-526

[147] J.D. Willingham & S.N. Shah 2000 Friction Pressures of Newtonian and Non-Newtonian Fluids in Straight and Reeled Coiled Tubing. *SPE paper number*, 60719-MS, in proceedings of the SPE/ICoTA Coiled Tubing Roundtable, 5-6 April 2000, Houston, Texas.

[148] K. Wojs 1993 Laminar and turbulent flow of dilute polymer solutions in smooth and rough pipes *J. Non-Newtonian Fluid Mech.*, **48**, pp. 337-355

[149] I.J. Wygnanski & F.H. Champagne 1973 On transition in a pipe. Part 1. The origin of puffs and slugs and the flow in a turbulent slug *J. Fluid Mech.*, **59**, pp. 281-335

[150] I.J. Wygnanski, M. Sokolov & D. Friedman 1975 On Transition in a Pipe. Part 2. The equilibrium puff. *J. Fluid Mech.*, **69**, pp. 283-304

Appendix A

Experimental pictures

Figure A.1: Image of the reservoir tank **R1**

Figure A.2: Image of the pipe and the reservoir tank **R2**

Figure A.3: Closer look to **FT** and the measuring stations

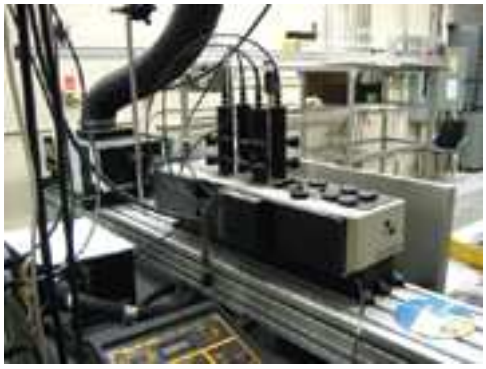

Figure A.4: Image of the LDV system

Appendix B

Experimental velocity

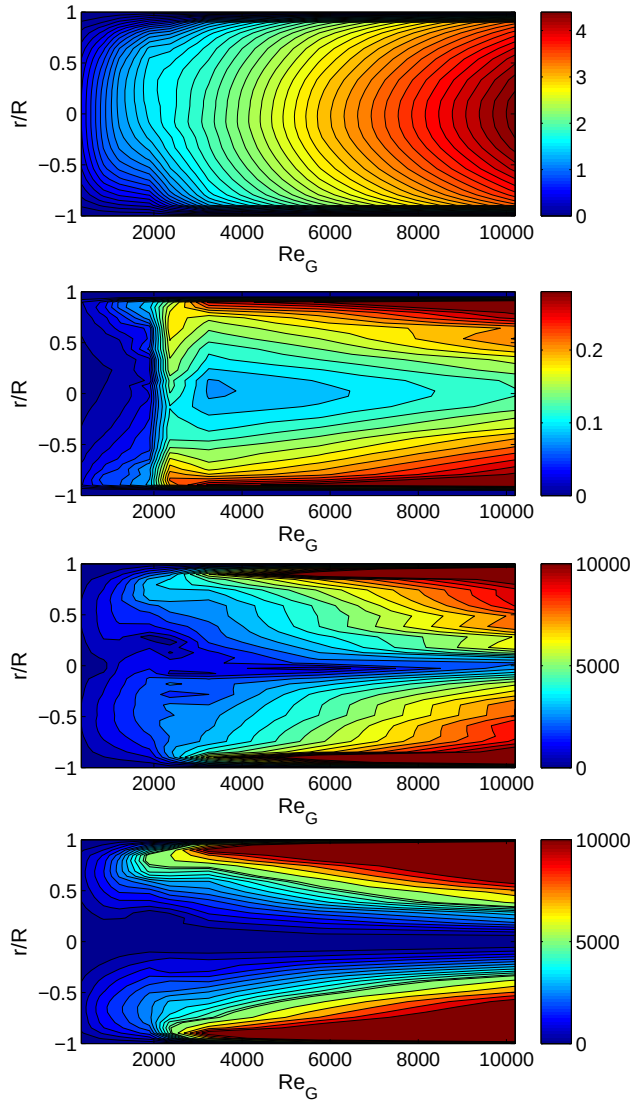

Figure B.1: From top to bottom; (a) Local velocity and (b) Local RMS velocity (c) $Re_{G,l}$ (d) ζ_G profiles for 0.2% Xanthan gum.

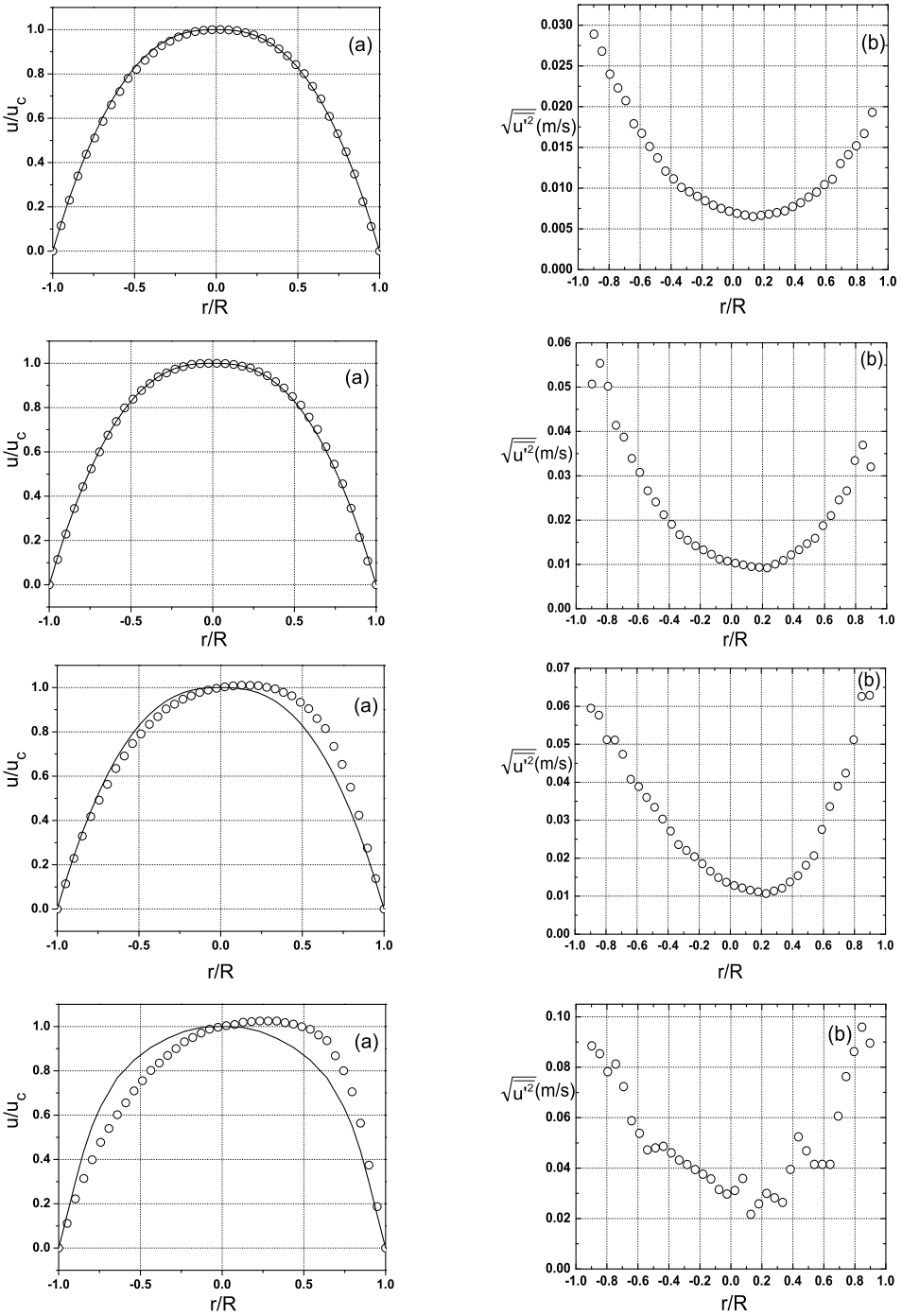

Figure B.2: (a) The time averaged velocity and (b) Local RMS velocity profiles for 0.2% Xanthan gum. From top to bottom; Re_G=352, Re_G=858, Re_G=1218 and Re_G=1900

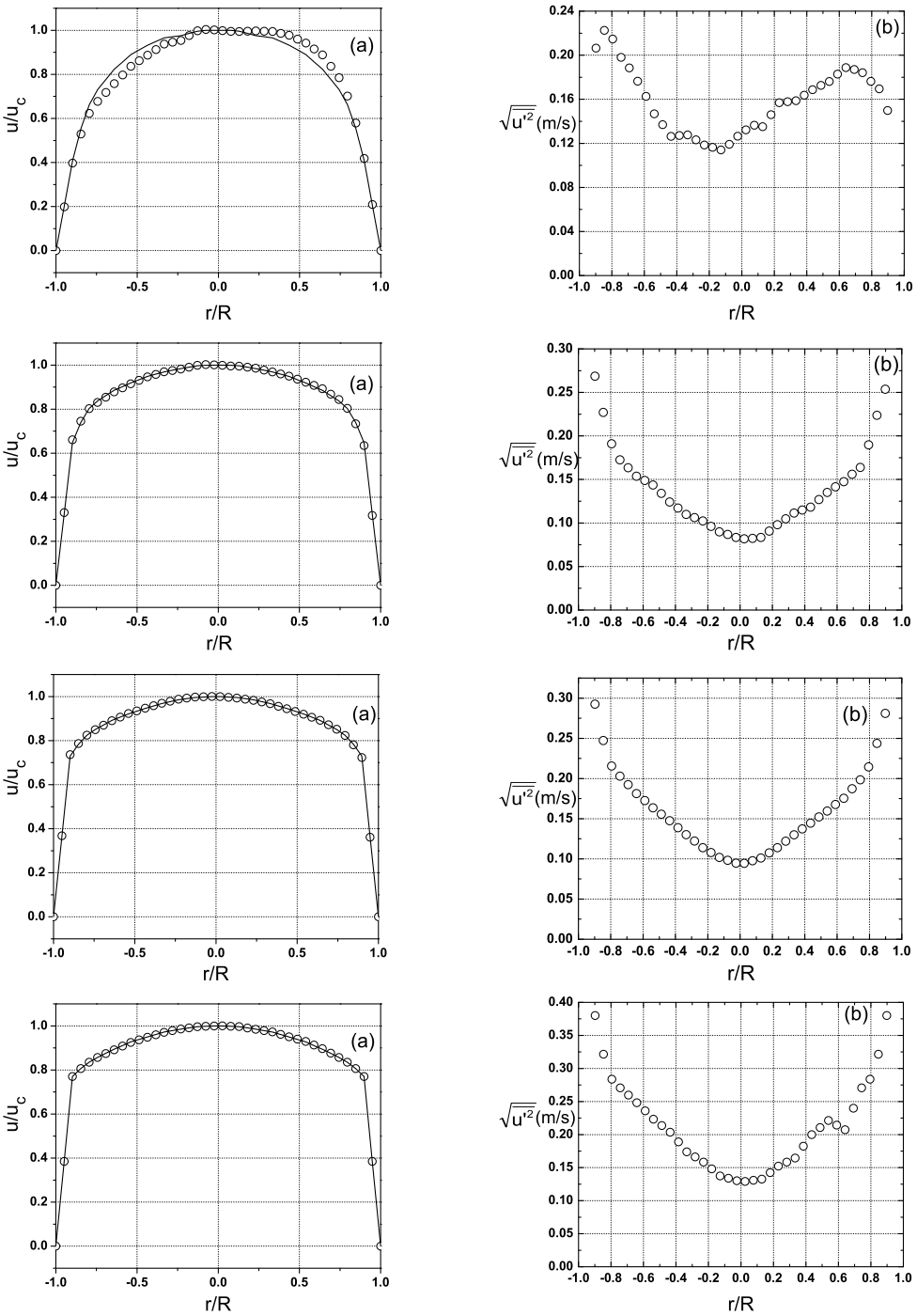

Figure B.3: (a) The time averaged velocity and (b) Local RMS velocity profiles for 0.2% Xanthan gum. From top to bottom; Re_G=2363, Re_G=3244, Re_G=5736 and Re_G=10197

$U_b(m/s)$	$\dot{\gamma}(s^{-1})$	$\kappa(Pa.s^n)$	n	Re_G	$T(^0C)$
0.2776	$0.2-46$	0.11	0.65	352	29
0.5396	$0.5-90$	0.11	0.65	858	29
0.7163	$0.7-137$	0.11	0.65	1218	29
0.9413	$1-224$	0.14	0.56	1900	29
1.1224	$1-270$	0.135	0.56	2363	30
1.4850	$2-501$	0.13	0.56	3244	30.5
2.2756	$2-835$	0.13	0.56	5736	31
3.4615	$3-1311$	0.13	0.56	10197	34

Table B.1: Flow conditions and power-law parameters for 0.2% Xanthan gum

Table B.2: Velocity readings for 0.2% Xanthan gum in Table B.1

	U_b=0.2776, ΔP=1.62		U_b=0.5396, ΔP=2.05		U_b=0.7163, ΔP=2.39		U_b=0.9413, ΔP=2.73	
r/R	$\overline{u}$	u'	$\overline{u}$	u'	$\overline{u}$	u'	$\overline{u}$	u'
-1	0	–	0	–	0	–	0	–
-0.94872	0.0579	–	0.11055	–	0.14065	–	0.17015	–
-0.89744	0.1158	0.0289	0.2211	0.0507	0.2813	0.0595	0.3403	0.0885
-0.84615	0.1705	0.0268	0.33243	0.05539	0.40617	0.05764	0.4797	0.08536
-0.79487	0.2196	0.024	0.42723	0.05019	0.51393	0.05118	0.60927	0.07825
-0.74359	0.2565	0.0223	0.5055	0.0414	0.6046	0.0511	0.729	0.0813
-0.69231	0.2943	0.02072	0.5787	0.03874	0.6927	0.04737	0.82415	0.07231
-0.64103	0.3321	0.0179	0.6519	0.0339	0.7808	0.0408	0.9193	0.0588
-0.58974	0.3619	0.01673	0.7111	0.03077	0.8499	0.03885	1.0014	0.05384
-0.53846	0.3917	0.0151	0.7703	0.0266	0.919	0.036	1.0835	0.0472
-0.48718	0.41225	0.01371	0.8084	0.02408	0.97235	0.03341	1.15415	0.04804
-0.4359	0.4328	0.0121	0.8465	0.0212	1.0257	0.0303	1.2248	0.0486
-0.38462	0.4494	0.01115	0.87625	0.01905	1.06835	0.02713	1.27625	0.04608
-0.33333	0.466	0.0101	0.906	0.0167	1.111	0.0236	1.3277	0.0432
-0.28205	0.4759	0.00957	0.92285	0.01548	1.13805	0.02205	1.37485	0.04141
-0.23077	0.4858	0.009	0.9397	0.0142	1.1651	0.0204	1.422	0.0394

Continued on next page

Table B.2 – continued from previous page

r/R	$\overline{u}$	u'	$\overline{u}$	u'	$\overline{u}$	u'	$\overline{u}$	u'
-0.17949	0.4919	0.00846	0.94995	0.01326	1.18395	0.01853	1.4523	0.0376
-0.12821	0.498	0.0079	0.9602	0.0123	1.2028	0.0166	1.4826	0.0357
-0.07692	0.5008	0.0075	0.9636	0.0112	1.2158	0.0149	1.5091	0.0315
-0.02564	0.5022	0.00717	0.965	0.01073	1.2258	0.01371	1.52237	0.02971
0.02564	0.50247	0.0069	0.96493	0.0103	1.23377	0.0128	1.5333	0.03115
0.07692	0.5016	0.0067	0.9634	0.0099	1.2397	0.0122	1.5419	0.0359
0.12821	0.4999	0.0065	0.9596	0.0095	1.2429	0.0116	1.5579	0.0217
0.17949	0.4952	0.00665	0.95205	0.00935	1.24155	0.01115	1.5619	0.02584
0.23077	0.4905	0.0068	0.9445	0.0092	1.2402	0.0107	1.5659	0.03
0.28205	0.4822	0.00701	0.92785	0.01007	1.2313	0.01141	1.5657	0.0282
0.33333	0.4739	0.0072	0.9112	0.0109	1.2224	0.0121	1.5655	0.0264
0.38462	0.4585	0.00773	0.88415	0.01215	1.2032	0.01378	1.5549	0.03949
0.4359	0.4431	0.0082	0.8571	0.0133	1.184	0.0154	1.5443	0.0524
0.48718	0.42275	0.0089	0.81995	0.01469	1.1485	0.01815	1.52635	0.04689
0.53846	0.4024	0.0095	0.7828	0.0159	1.113	0.0207	1.5084	0.0415
0.58974	0.37375	0.01042	0.7299	0.01873	1.05785	0.02756	1.46935	0.04153
0.64103	0.3451	0.0111	0.677	0.021	1.0027	0.0336	1.4303	0.0415
0.69231	0.30555	0.01301	0.60105	0.02455	0.90295	0.03896	1.3264	0.06064
0.74359	0.266	0.0141	0.5251	0.0266	0.8032	0.0424	1.2225	0.0763

Continued on next page

Table B.2 – continued from previous page

r/R	$\overline{u}$	u'	$\overline{u}$	u'	$\overline{u}$	u'	$\overline{u}$	u'
0.79487	0.2254	0.0152	0.43983	0.03341	0.67627	0.05119	1.07797	0.08624
0.84615	0.1749	0.0167	0.3338	0.03692	0.52143	0.06257	0.86117	0.09594
0.89744	0.1124	0.0193	0.207	0.032	0.3387	0.0629	0.5721	0.0896
0.94872	0.0562	–	0.1035	–	0.16935	–	0.28605	–
1	0	–	0	–	0	–	0	–

Table B.3: Velocity readings for 0.2% Xanthan gum in Table B.1

	U_b=1.1224, ΔP=3.22		U_b=1.4850, ΔP=4.42		U_b=2.2756, ΔP=7.52		U_b=3.4615, ΔP=13.7	
r/R	$\overline{u}$	u'	$\overline{u}$	u'	$\overline{u}$	u'	$\overline{u}$	u'
-1	0	–	0	–	0	–	0	–
-0.94872	0.3298	–	0.6431	–	1.07095	–	1.68115	–
-0.89744	0.6596	0.2065	1.2862	0.2687	2.1419	0.2926	3.3623	0.3801
-0.84615	0.87887	0.22259	1.45187	0.22705	2.28923	0.24731	3.5195	0.3216
-0.79487	1.03397	0.21467	1.56207	0.19106	2.3991	0.21558	3.64547	0.28369
-0.74359	1.1249	0.1981	1.6168	0.1725	2.4715	0.2029	3.7402	0.2707
-0.69231	1.19175	0.18845	1.6636	0.16349	2.53105	0.19246	3.81645	0.25973
-0.64103	1.2586	0.1764	1.7104	0.1537	2.5906	0.1813	3.8927	0.2481
-0.58974	1.32395	0.16273	1.74585	0.14881	2.63785	0.17266	3.96495	0.23596
-0.53846	1.3893	0.1468	1.7813	0.1436	2.6851	0.1636	4.0372	0.2232
-0.48718	1.4312	0.13702	1.8123	0.13406	2.7204	0.15568	4.08905	0.21356
-0.4359	1.4731	0.1264	1.8433	0.1241	2.7557	0.1475	4.1409	0.2036
-0.38462	1.5145	0.12713	1.8652	0.1171	2.788	0.13892	4.18965	0.18895
-0.33333	1.5559	0.1277	1.8871	0.1099	2.8203	0.1301	4.2384	0.1739
-0.28205	1.57	0.12315	1.8997	0.10613	2.84735	0.12214	4.27085	0.16622
-0.23077	1.5841	0.1185	1.9123	0.1023	2.8744	0.114	4.3033	0.1584

Continued on next page

Table B.3 – continued from previous page

r/R	$\overline{u}$	u'	$\overline{u}$	u'	$\overline{u}$	u'	$\overline{u}$	u'
-0.17949	1.6201	0.11641	1.92855	0.09611	2.88925	0.10793	4.3261	0.14801
-0.12821	1.6561	0.1141	1.9448	0.0898	2.9041	0.1018	4.3489	0.1375
-0.07692	1.6665	0.1191	1.9521	0.0868	2.90758	0.09821	4.3567	0.13383
-0.02564	1.66263	0.12644	1.94917	0.08333	2.91106	0.0946	4.3645	0.13015
0.02564	1.65783	0.13221	1.9447	0.08187	2.9083	0.09447	4.36512	0.12916
0.07692	1.6521	0.1364	1.9387	0.0824	2.8993	0.0978	4.35856	0.13088
0.12821	1.6511	0.1351	1.9378	0.0834	2.8903	0.1011	4.352	0.1326
0.17949	1.65325	0.14599	1.92865	0.09079	2.8751	0.10754	4.32435	0.14252
0.23077	1.6554	0.1569	1.9195	0.0981	2.8599	0.1139	4.2967	0.1523
0.28205	1.6531	0.1578	1.9032	0.10481	2.83755	0.12197	4.27205	0.15849
0.33333	1.6508	0.1587	1.8869	0.1114	2.8152	0.1299	4.2474	0.1646
0.38462	1.6368	0.16375	1.86845	0.11484	2.7819	0.13731	4.1989	0.18243
0.4359	1.6228	0.1687	1.85	0.1182	2.7486	0.1445	4.1504	0.1998
0.48718	1.5936	0.17258	1.8232	0.12685	2.71275	0.15218	4.10415	0.21065
0.53846	1.5644	0.1762	1.7964	0.1352	2.6769	0.1596	4.0579	0.2212
0.58974	1.5196	0.18284	1.7671	0.14149	2.63665	0.16771	3.9857	0.21425
0.64103	1.4748	0.1888	1.7378	0.1475	2.5964	0.1755	3.9135	0.2074
0.69231	1.38865	0.18702	1.6905	0.156	2.53695	0.18732	3.82685	0.23989
0.74359	1.3025	0.1841	1.6432	0.1638	2.4775	0.1984	3.7402	0.2707

Continued on next page

Table B.3 – continued from previous page

r/R	$\overline{u}$	u'	$\overline{u}$	u'	$\overline{u}$	u'	$\overline{u}$	u'
0.79487	1.16417	0.17633	1.5646	0.18985	2.3961	0.21438	3.64547	0.28369
0.84615	0.9616	0.16945	1.4287	0.22368	2.27173	0.24376	3.5195	0.3216
0.89744	0.6948	0.1498	1.2355	0.2537	2.1044	0.2811	3.3623	0.3801
0.94872	0.3474	–	0.61775	–	1.0522	–	1.68115	–
1	0	–	0	–	0	–	0	–

$U(m/s)$	$\dot{\gamma}(s^{-1})$	$\kappa(Pa.s^n)$	n	Re_G	$T(^0C)$
0.4613	$0.1-82$	0.23	0.56	451	30
0.6957	$0.1-118$	0.23	0.56	809	30
0.8775	$1-192$	0.22	0.56	1185	30
1.3574	$2-598$	0.20	0.56	2244	31
1.5616	$1-635$	0.14	0.64	2542	32
2.0574	$1-692$	0.11	0.69	3513	33
2.5877	$1-988$	0.10	0.69	5070	34

Table B.4: Flow conditions and power-law parameters for 0.2% Xanthan gum

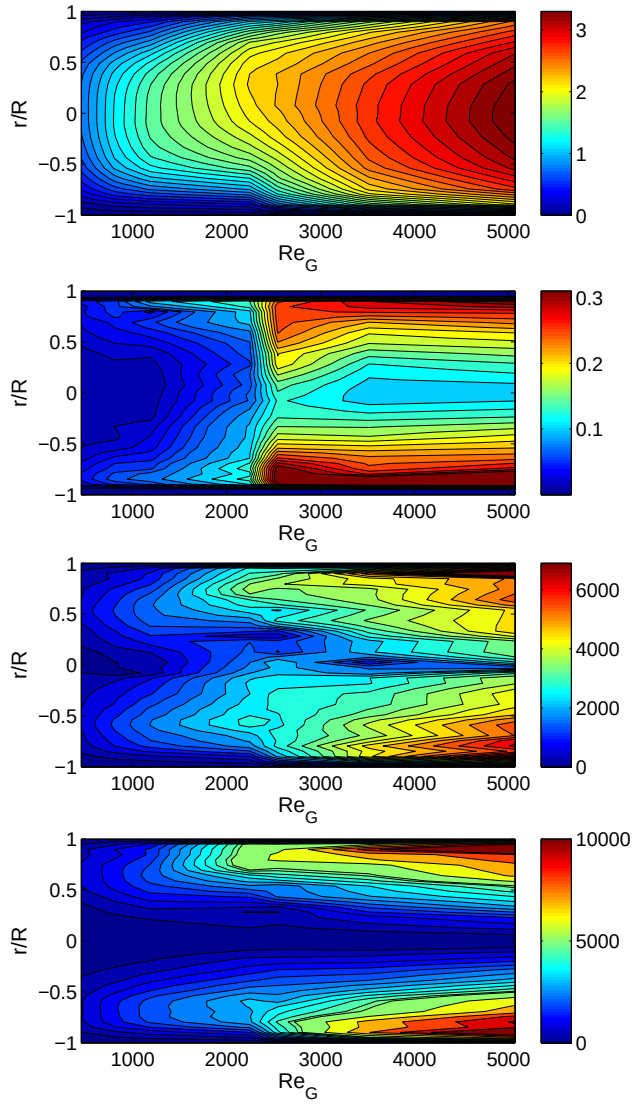

Figure B.4: From top to bottom; (a) Local velocity and (b) Local RMS velocity (c) $Re_{G,l}$ (d) ζ_G profiles for 0.2% Xanthan gum.

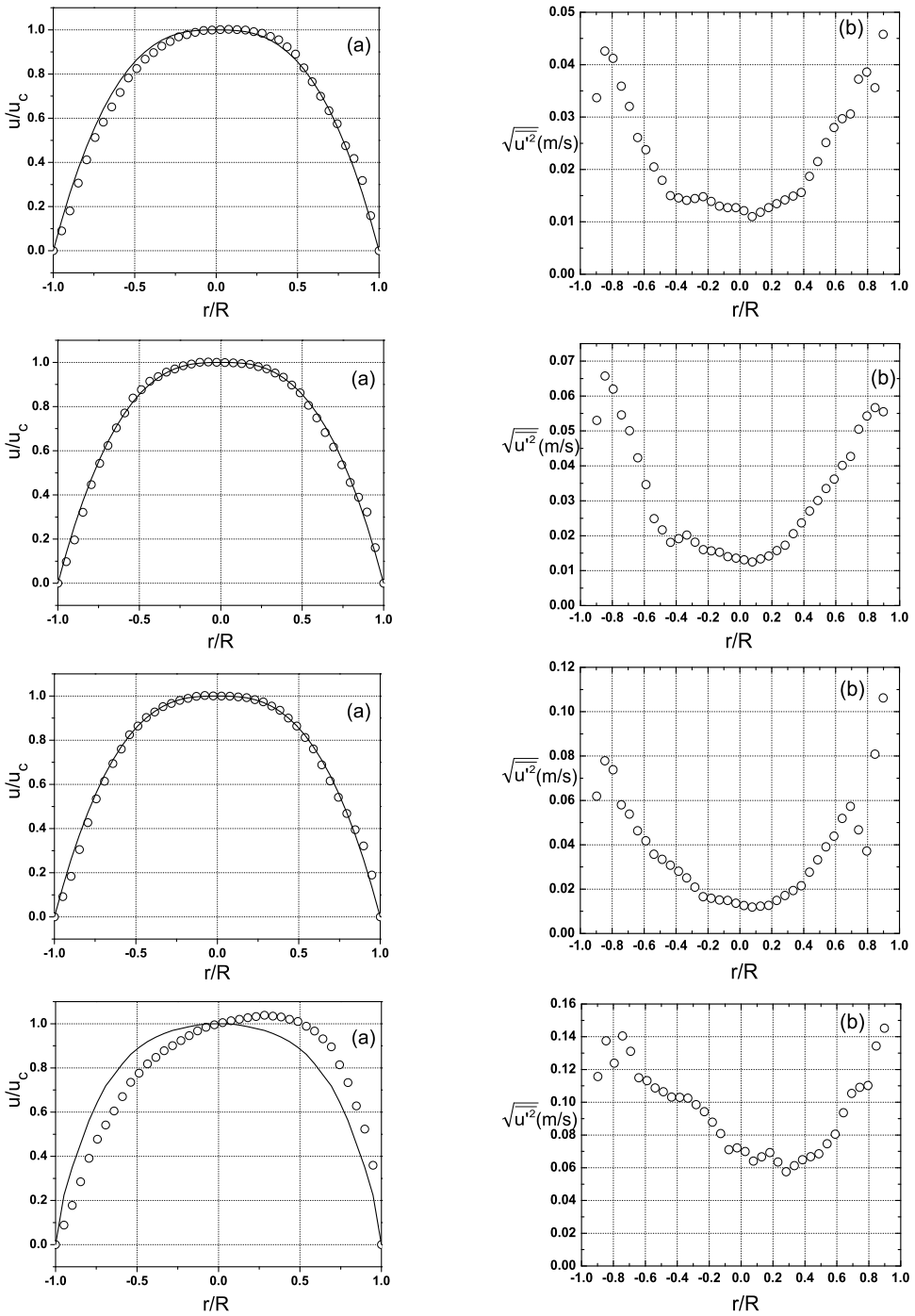

Figure B.5: (a) The time averaged velocity and (b) Local RMS velocity profiles for 0.2% Xanthan gum. From top to bottom; Re_G=451, Re_G=809, Re_G=1185 and Re_G=2244

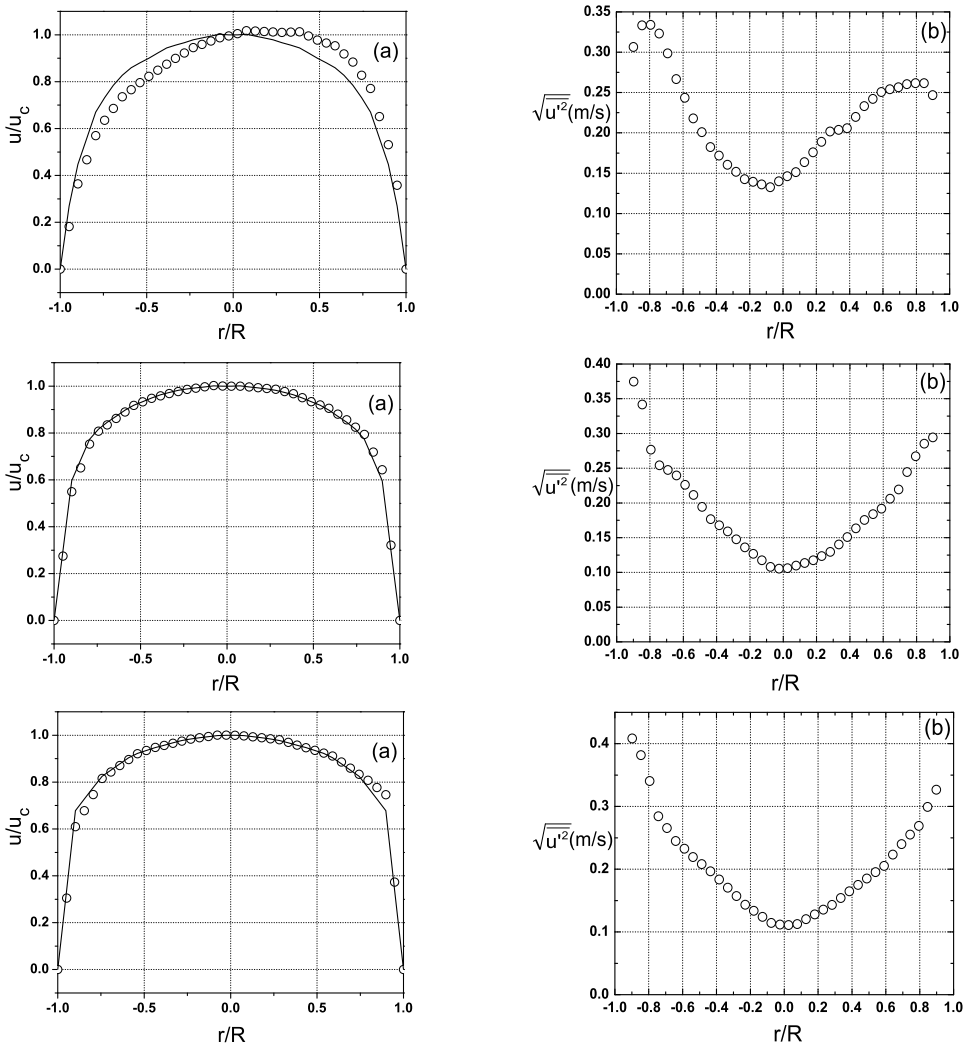

Figure B.6: (a) The time averaged velocity and (b) Local RMS velocity profiles for 0.2% Xanthan gum. From top to bottom; Re_G=2542, Re_G=3513 and Re_G=5070

Table B.5: Velocity readings for 0.2% Xanthan gum in Table B.4

	U_b=0.4613, ΔP=2.09		U_b=0.6957, ΔP=2.49		U_b=0.8775, ΔP=2.83		U_b=1.3574, ΔP=3.75	
r/R	$\overline{u}$	u'	$\overline{u}$	u'	$\overline{u}$	u'	$\overline{u}$	u'
-1	0	–	0	–	0	–	0	–
-0.94872	0.0735	–	0.1191	–	0.14105	–	0.19005	–
-0.89744	0.147	0.0337	0.2382	0.053	0.2821	0.0619	0.3801	0.1157
-0.84615	0.2497	0.0426	0.3902	0.06572	0.4691	0.07785	0.6072	0.1375
-0.79487	0.336	0.0412	0.5422	0.062	0.6561	0.0738	0.8343	0.1239
-0.74359	0.4183	0.0359	0.6596	0.0546	0.8214	0.058	1.0196	0.1405
-0.69231	0.4747	0.03203	0.7569	0.05007	0.94385	0.05381	1.1559	0.13108
-0.64103	0.5311	0.0261	0.8542	0.0423	1.0663	0.0463	1.2922	0.115
-0.58974	0.58435	0.02375	0.9363	0.03463	1.1669	0.04177	1.4305	0.11321
-0.53846	0.6376	0.0205	1.0184	0.0249	1.2675	0.0357	1.5688	0.1087
-0.48718	0.6724	0.01794	1.06445	0.02169	1.3274	0.03343	1.65755	0.1064
-0.4359	0.7072	0.015	1.1105	0.0181	1.3873	0.0308	1.7463	0.1032
-0.38462	0.73115	0.01458	1.1357	0.01914	1.425	0.02805	1.80985	0.10299
-0.33333	0.7551	0.0141	1.1609	0.0202	1.4627	0.0251	1.8734	0.1025
-0.28205	0.7723	0.01445	1.17825	0.01813	1.48435	0.02092	1.9227	0.09857
-0.23077	0.7895	0.0148	1.1956	0.016	1.506	0.0166	1.972	0.0943

Continued on next page

Table B.5 – continued from previous page

r/R	$\overline{u}$	u'	$\overline{u}$	u'	$\overline{u}$	u'	$\overline{u}$	u'
-0.17949	0.7978	0.01391	1.20525	0.01565	1.5201	0.01586	2.0189	0.0878
-0.12821	0.8061	0.013	1.2149	0.0153	1.5342	0.0151	2.0658	0.0809
-0.07692	0.8131	0.0127	1.2166	0.014	1.5399	0.0149	2.1006	0.071
-0.02564	0.8147	0.0127	1.21513	0.0136	1.53717	0.01363	2.12433	0.0722
0.02564	0.8161	0.01213	1.21353	0.0131	1.5354	0.01263	2.14543	0.06993
0.07692	0.8173	0.011	1.2118	0.0125	1.5346	0.0119	2.1639	0.0641
0.12821	0.8161	0.01185	1.20755	0.01335	1.52985	0.0123	2.1782	0.06669
0.17949	0.8149	0.0127	1.2033	0.0142	1.5251	0.0127	2.1925	0.0693
0.23077	0.8089	0.01346	1.19095	0.01577	1.5104	0.01492	2.2048	0.06348
0.28205	0.8029	0.0142	1.1786	0.0173	1.4957	0.0171	2.2171	0.0576
0.33333	0.791	0.01491	1.1556	0.02057	1.4666	0.01935	2.20875	0.06126
0.38462	0.7791	0.0156	1.1326	0.0237	1.4375	0.0215	2.2004	0.0649
0.4359	0.7526	0.01868	1.0898	0.02707	1.38255	0.02763	2.1782	0.06673
0.48718	0.7261	0.0215	1.047	0.0301	1.3276	0.0332	2.156	0.0685
0.53846	0.6749	0.02514	0.9782	0.03353	1.2482	0.03905	2.11045	0.07466
0.58974	0.6237	0.028	0.9094	0.0362	1.1688	0.0439	2.0649	0.0805
0.64103	0.57025	0.02968	0.8292	0.04014	1.0573	0.05188	1.9883	0.09357
0.69231	0.5168	0.0306	0.749	0.0427	0.9458	0.0573	1.9117	0.1054
0.74359	0.4691	0.03723	0.65155	0.0505	0.83235	0.04675	1.73875	0.10912

Continued on next page

Table B.5 – continued from previous page

r/R	$\overline{u}$	u'	$\overline{u}$	u'	$\overline{u}$	u'	$\overline{u}$	u'
0.79487	0.3878	0.0386	0.5541	0.0543	0.7189	0.0372	1.5658	0.1102
0.84615	0.3407	0.0356	0.47285	0.05668	0.60655	0.08086	1.34125	0.1344
0.89744	0.2595	0.0458	0.3916	0.0555	0.4942	0.10619	1.1167	0.1452
0.94872	0.12975	–	0.1958	–	0.2918	–	0.7674	–
1	0	–	0	–	0	–	0	–

Table B.6: Velocity readings for 0.2% Xanthan gum in Table B.4

	U_b=1.5616, ΔP=4.52		U_b=2.0574, ΔP=6.09		U_b=2.5877, ΔP=7.8	
r/R	$\overline{u}$	u'	$\overline{u}$	u'	$\overline{u}$	u'
-1	0	–	0	–	0	–
-0.94872	0.41425	–	0.75905	–	1.0352	–
-0.89744	0.8285	0.3065	1.5181	0.3748	2.0704	0.4085
-0.84615	1.0626	0.33336	1.79835	0.34169	2.30373	0.38188
-0.79487	1.2967	0.3339	2.0786	0.2767	2.53707	0.34055
-0.74359	1.4464	0.3231	2.2311	0.2543	2.7704	0.2845
-0.69231	1.5604	0.29855	2.3056	0.2474	2.8638	0.26563
-0.64103	1.6744	0.2667	2.3801	0.2395	2.9572	0.2449
-0.58974	1.7429	0.24364	2.4575	0.22617	3.04335	0.23265
-0.53846	1.8114	0.2179	2.5349	0.2115	3.1295	0.2193
-0.48718	1.87225	0.20094	2.5766	0.19438	3.17455	0.20815
-0.4359	1.9331	0.1824	2.6183	0.1766	3.2196	0.1966
-0.38462	1.9905	0.17186	2.646	0.16791	3.2499	0.18371
-0.33333	2.0479	0.1604	2.6737	0.159	3.2802	0.17055
-0.28205	2.09965	0.15176	2.69825	0.14767	3.3105	0.15711
-0.23077	2.1514	0.1425	2.7228	0.1361	3.3408	0.1434

Continued on next page

Table B.6 – continued from previous page

r/R	$\overline{u}$	u'	$\overline{u}$	u'	$\overline{u}$	u'
-0.17949	2.18323	0.13939	2.73793	0.12681	3.35963	0.13385
-0.12821	2.21507	0.13612	2.75307	0.11741	3.37847	0.12418
-0.07692	2.2469	0.1327	2.7682	0.1079	3.3973	0.1144
-0.02564	2.26463	0.14001	2.76267	0.10543	3.3985	0.11167
0.02564	2.28757	0.14625	2.7605	0.10603	3.39537	0.11107
0.07692	2.3157	0.1514	2.7617	0.1097	3.3879	0.1126
0.12821	2.31225	0.16372	2.75195	0.11357	3.37363	0.12033
0.17949	2.3088	0.176	2.7422	0.1174	3.35935	0.12799
0.23077	2.3042	0.18893	2.73315	0.12352	3.34508	0.13558
0.28205	2.2996	0.2018	2.7241	0.1296	3.3308	0.1431
0.33333	2.30275	0.2038	2.6983	0.14031	3.29268	0.15404
0.38462	2.3059	0.2058	2.6725	0.1508	3.25455	0.16468
0.4359	2.26515	0.21982	2.62555	0.16342	3.21643	0.17504
0.48718	2.2244	0.2332	2.5786	0.1755	3.1783	0.1851
0.53846	2.197	0.24205	2.5392	0.18377	3.1374	0.19531
0.58974	2.1696	0.2506	2.4998	0.1917	3.0965	0.2052
0.64103	2.09065	0.25402	2.43185	0.20615	3.0081	0.22326
0.69231	2.0117	0.2565	2.3639	0.2195	2.9197	0.23991
0.74359	1.88295	0.26044	2.27785	0.24455	2.8313	0.25516

Continued on next page

Table B.6 – continued from previous page

r/R	$\overline{u}$	u'	$\overline{u}$	u'	$\overline{u}$	u'
0.79487	1.7542	0.2616	2.1918	0.2671	2.7429	0.269
0.84615	1.4813	0.26172	1.98405	0.28531	2.63855	0.29941
0.89744	1.2084	0.2468	1.7763	0.2944	2.5342	0.3266
0.94872	0.81453	–	0.88815	–	1.2671	–
1	0	–	0	–	0	–

$U(m/s)$	$\dot{\gamma}(s^{-1})$	$\kappa(Pa.s^n)$	n	Re_G	$T(^0C)$
0.3747	$0.2-66$	0.0235	0.77	1701	30
0.4529	$0.3-78$	0.0235	0.77	2131	31
0.4954	$0.5-113$	0.019	0.78	2789	32
0.5414	$0.5-104$	0.015	0.80	3538	33
0.8802	$0.4-301$	0.0103	0.80	8370	33
2.0203	$2-757$	0.0083	0.82	24746	34

Table B.7: Flow conditions and power-law parameters for 0.1% Xanthan gum

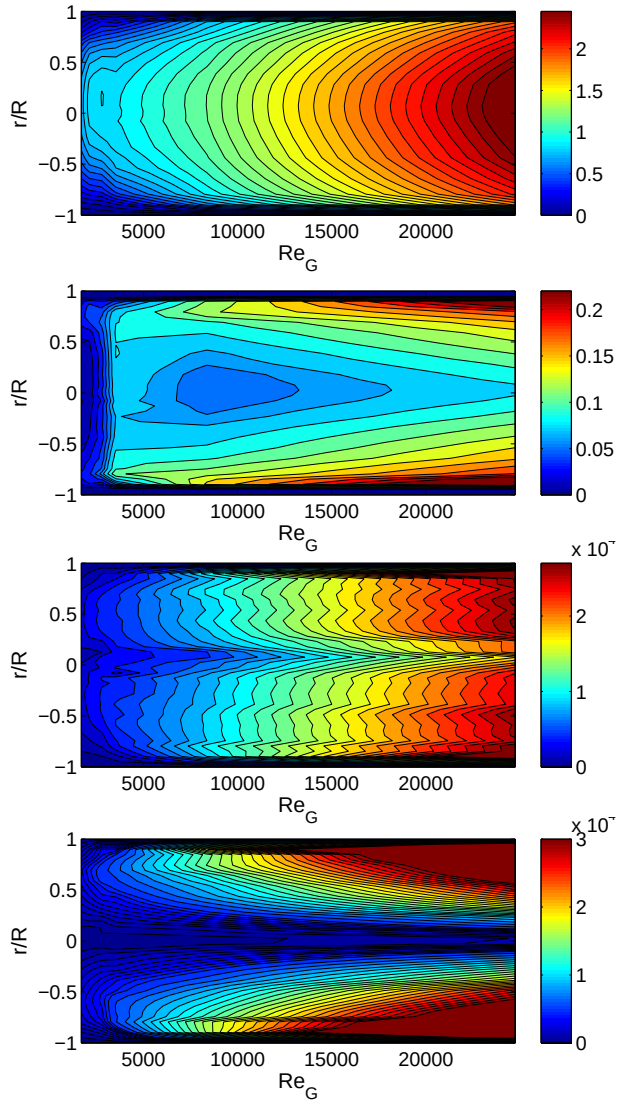

Figure B.7: From top to bottom; (a) Local velocity and (b) Local RMS velocity (c) $Re_{G,l}$ (d) ζ_G profiles for 0.1% Xanthan gum.

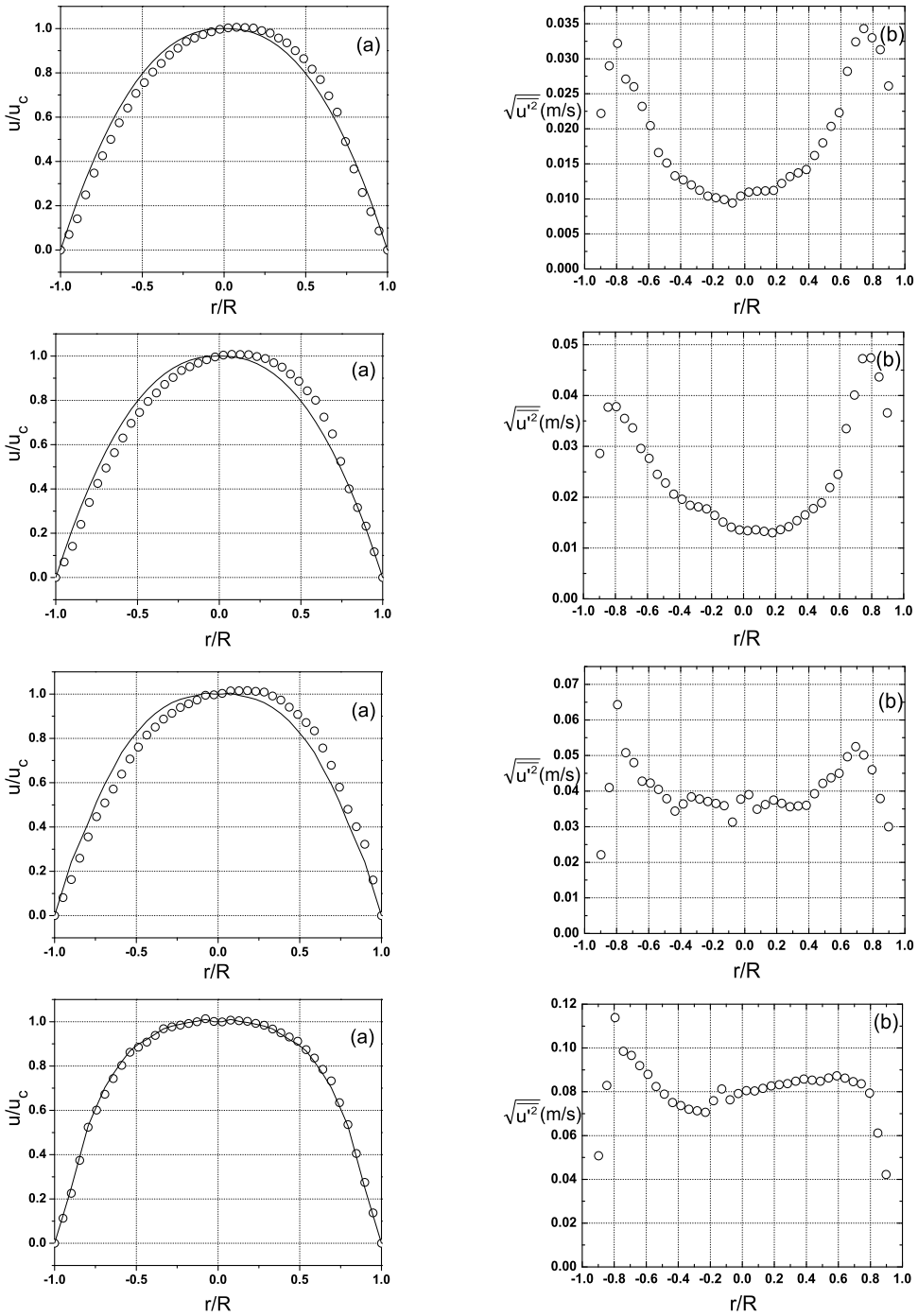

Figure B.8: (a) The time averaged velocity and (b) Local RMS velocity profiles for 0.1% Xanthan gum. From top to bottom; Re_G=1701, Re_G=2131, Re_G=2789 and Re_G=3538

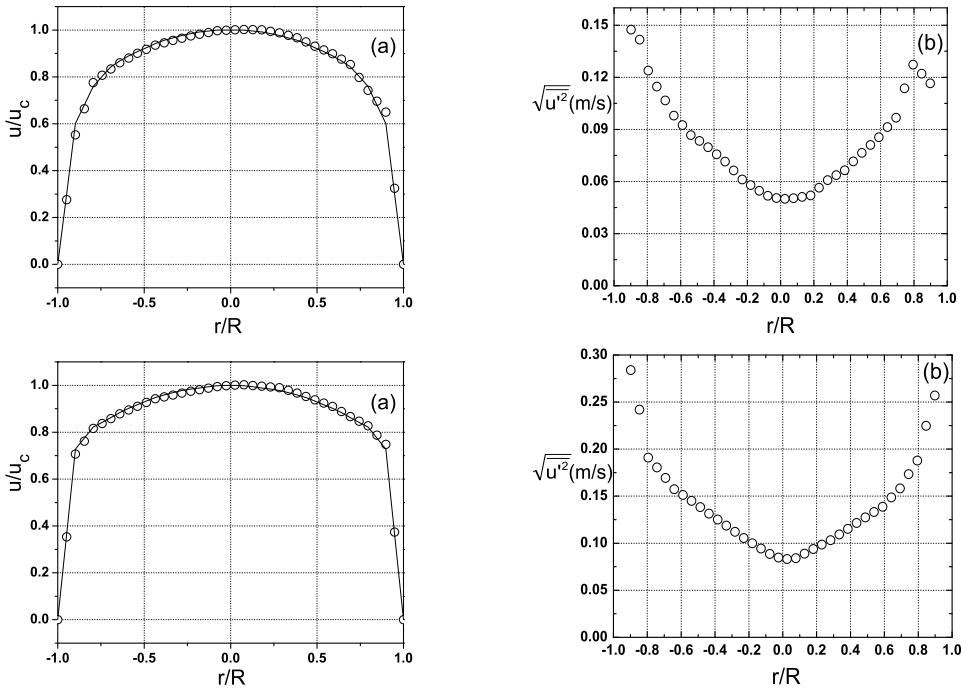

Figure B.9: (a) The time averaged velocity and (b) Local RMS velocity profiles for 0.1% Xanthan gum. From top to bottom; Re_G=8370 and Re_G=24746

Table B.8: Velocity readings for 0.1% Xanthan gum in Table B.7

	U_b=0.3747, ΔP=0.48		U_b=0.4529, ΔP=0.71		U_b=0.4954, ΔP=0.94		U_b=0.5414, ΔP=1.08	
r/R	$\overline{u}$	u'	$\overline{u}$	u'	$\overline{u}$	u'	$\overline{u}$	u'
-1	0	–	0	–	0	–	0	–
-0.94872	0.05175	–	0.0611	–	0.0732	–	0.1007	–
-0.89744	0.1035	0.0222	0.1222	0.0286	0.1464	0.0221	0.2014	0.0508
-0.84615	0.1829	0.029	0.208	0.03772	0.23285	0.04102	0.33415	0.0829
-0.79487	0.2546	0.0322	0.2938	0.0378	0.3193	0.0643	0.4669	0.1139
-0.74359	0.312	0.0271	0.3679	0.0355	0.4012	0.0508	0.5363	0.0985
-0.69231	0.3664	0.02601	0.4282	0.03363	0.45695	0.048	0.5997	0.09663
-0.64103	0.4208	0.0232	0.4885	0.0296	0.5127	0.0428	0.6631	0.0919
-0.58974	0.4697	0.02047	0.54575	0.02762	0.57385	0.04225	0.7159	0.08798
-0.53846	0.5186	0.0166	0.603	0.0245	0.635	0.0405	0.7687	0.0824
-0.48718	0.5539	0.01512	0.64585	0.02278	0.68335	0.03786	0.7891	0.0789
-0.4359	0.5892	0.0133	0.6887	0.0206	0.7317	0.0344	0.8095	0.0751
-0.38462	0.6173	0.01271	0.72185	0.01959	0.7641	0.03638	0.83645	0.07368
-0.33333	0.6454	0.012	0.755	0.0184	0.7965	0.0384	0.8634	0.072
-0.28205	0.6677	0.01124	0.7824	0.01808	0.8201	0.0378	0.8706	0.07131
-0.23077	0.69	0.0104	0.8098	0.0177	0.8437	0.0371	0.8778	0.0706

Continued on next page

Table B.8 – continued from previous page

r/R	$\overline{u}$	u'	$\overline{u}$	u'	$\overline{u}$	u'	$\overline{u}$	u'
-0.17949	0.7014	0.01016	0.82435	0.01643	0.8587	0.03652	0.8845	0.07591
-0.12821	0.7128	0.0099	0.8389	0.0151	0.8737	0.0359	0.8912	0.0813
-0.07692	0.7223	0.0094	0.8518	0.0141	0.8931	0.0313	0.9037	0.0763
-0.02564	0.73043	0.0104	0.86273	0.01357	0.89523	0.03776	0.89257	0.07919
0.02564	0.7353	0.01097	0.86967	0.0134	0.9012	0.03899	0.89053	0.08054
0.07692	0.7369	0.0111	0.8726	0.0136	0.911	0.0349	0.8976	0.0804
0.12821	0.7358	0.01115	0.87225	0.0133	0.9116	0.0362	0.8952	0.08155
0.17949	0.7347	0.0112	0.8719	0.013	0.9122	0.0375	0.8928	0.0827
0.23077	0.72615	0.01221	0.8641	0.01361	0.9093	0.03655	0.885	0.08321
0.28205	0.7176	0.0132	0.8563	0.0142	0.9064	0.0356	0.8772	0.0837
0.33333	0.7016	0.01372	0.8397	0.01538	0.8902	0.03582	0.8621	0.08479
0.38462	0.6856	0.0142	0.8231	0.0165	0.874	0.036	0.847	0.0858
0.4359	0.65945	0.0162	0.7953	0.01776	0.8448	0.03925	0.83	0.08533
0.48718	0.6333	0.018	0.7675	0.0189	0.8156	0.0422	0.813	0.0848
0.53846	0.59875	0.02034	0.73045	0.0219	0.7823	0.04374	0.77915	0.08627
0.58974	0.5642	0.0223	0.6934	0.0245	0.749	0.045	0.7453	0.0873
0.64103	0.5103	0.0282	0.6276	0.03349	0.6794	0.04966	0.6994	0.08623
0.69231	0.4564	0.0324	0.5618	0.0401	0.6098	0.0525	0.6535	0.0846
0.74359	0.3592	0.0343	0.45435	0.04726	0.5206	0.05017	0.5657	0.08361

Continued on next page

Table B.8 – continued from previous page

r/R	$\overline{u}$	u'	$\overline{u}$	u'	$\overline{u}$	u'	$\overline{u}$	u'
0.79487	0.268	0.033	0.3469	0.0474	0.4314	0.046	0.4779	0.0794
0.84615	0.1902	0.0313	0.274	0.04365	0.36035	0.0379	0.3615	0.06115
0.89744	0.1268	0.02612	0.2011	0.0366	0.2893	0.03	0.2451	0.0422
0.94872	0.0634	–	0.10055	–	0.14465	–	0.12255	–
1	0	–	0	–	0	–	0	–

Table B.9: Velocity readings for 0.1% Xanthan gum in Table B.7

	U_b=0.8802, ΔP=2.24		U_b=2.0203, ΔP=5.58	
r/R	$\overline{u}$	u'	$\overline{u}$	u'
-1	0	–	0	–
-0.94872	0.3285	–	0.9172	–
-0.89744	0.657	0.1475	1.8344	0.2839
-0.84615	0.7898	0.14169	1.97645	0.24204
-0.79487	0.9226	0.1239	2.1185	0.191
-0.74359	0.96	0.1147	2.17213	0.18055
-0.69231	0.9914	0.10672	2.22577	0.16935
-0.64103	1.0228	0.098	2.2794	0.1574
-0.58974	1.047	0.09253	2.32112	0.15138
-0.53846	1.0712	0.0867	2.36285	0.14504
-0.48718	1.09185	0.08335	2.40457	0.13838
-0.4359	1.1125	0.0798	2.4463	0.1314
-0.38462	1.12445	0.0757	2.4669	0.12511
-0.33333	1.1364	0.0715	2.4875	0.1187
-0.28205	1.14785	0.06641	2.5081	0.11216
-0.23077	1.1593	0.0612	2.5287	0.1055

Continued on next page

Table B.9 – continued from previous page

r/R	$\overline{u}$	u'	$\overline{u}$	u'
-0.17949	1.16805	0.05798	2.5458	0.09998
-0.12821	1.1768	0.0547	2.5629	0.09438
-0.07692	1.1859	0.0518	2.58	0.0887
-0.02564	1.18823	0.05053	2.59113	0.08484
0.02564	1.19023	0.05007	2.598	0.0833
0.07692	1.1919	0.0504	2.6006	0.0841
0.12821	1.1913	0.0512	2.5926	0.08895
0.17949	1.1907	0.052	2.5846	0.09376
0.23077	1.18285	0.05643	2.5766	0.09855
0.28205	1.175	0.0608	2.5686	0.1033
0.33333	1.16255	0.06369	2.53885	0.10939
0.38462	1.1501	0.0665	2.5091	0.1153
0.4359	1.1286	0.07162	2.47198	0.12151
0.48718	1.1071	0.0765	2.43485	0.12748
0.53846	1.0881	0.0811	2.39772	0.13321
0.58974	1.0691	0.0855	2.3606	0.1387
0.64103	1.0418	0.09136	2.305	0.14877
0.69231	1.0145	0.0968	2.2494	0.1582
0.74359	0.94895	0.11365	2.19765	0.1735

Continued on next page

Table B.9 – continued from previous page

r/R	$\overline{u}$	u'	$\overline{u}$	u'
0.79487	0.8834	0.1273	2.1459	0.1879
0.84615	0.82805	0.12208	2.04345	0.22475
0.89744	0.7727	0.1165	1.941	0.257
0.94872	0.38635	–	0.9705	–
1	0	–	0	–

$U(m/s)$	$\dot{\gamma}(s^{-1})$	$\tau_y(Pa)$	$\kappa(Pa.s^n)$	n	$r_p(mm)$	Re_G	$T(^0C)$
0.11202	$0.1-24$	2	2.05	0.36	5.55	5.5	29
0.4622	$0.1-87$	1.5	2.01	0.40	2.57	67	29
1.2076	$1-220$	1.4	1.59	0.43	1.84	378	29
2.0461	$5-414$	1.3	1.20	0.48	1.40	937	31
2.3218	$5-472$	1.2	0.92	0.53	1.20	1160	32.5
3.1146	$5-657$	1	0.65	0.60	–	1735	36
3.9005	$5-1261$	0.6	0.35	0.65	–	2920	39
4.3967	$5-1559$	0.4	0.20	0.70	–	4488	43

Table B.10: Flow conditions and Herschel-Bulkley parameters for 0.1% Carbopol

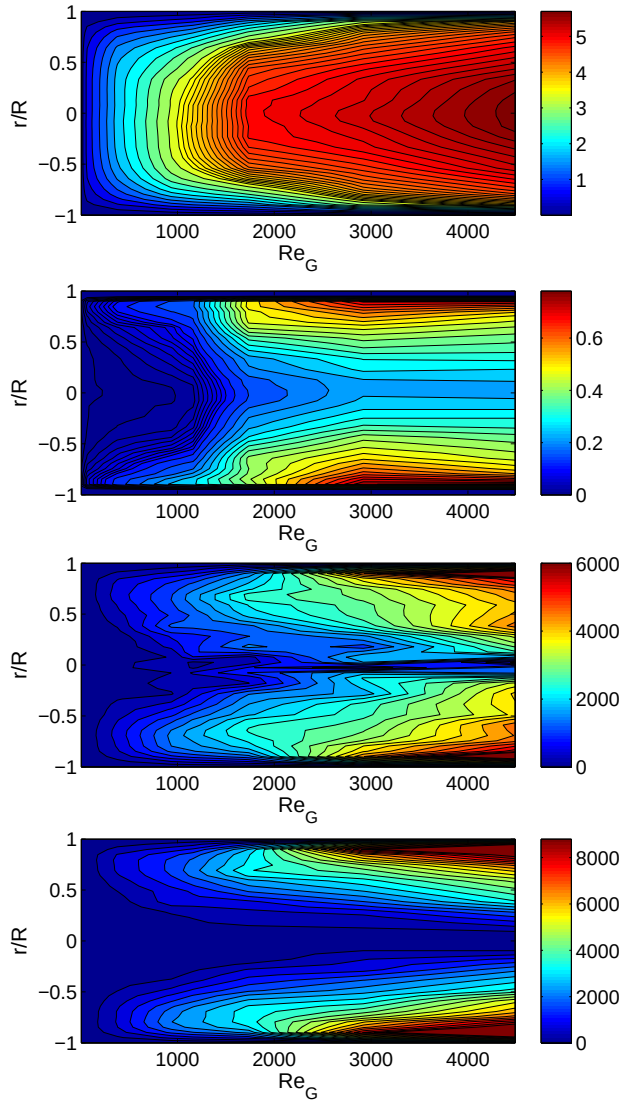

Figure B.10: From top to bottom; (a) Local velocity and (b) Local RMS velocity (c) $Re_{G,l}$ (d) ζ_G profiles for 0.1% Carbopol.

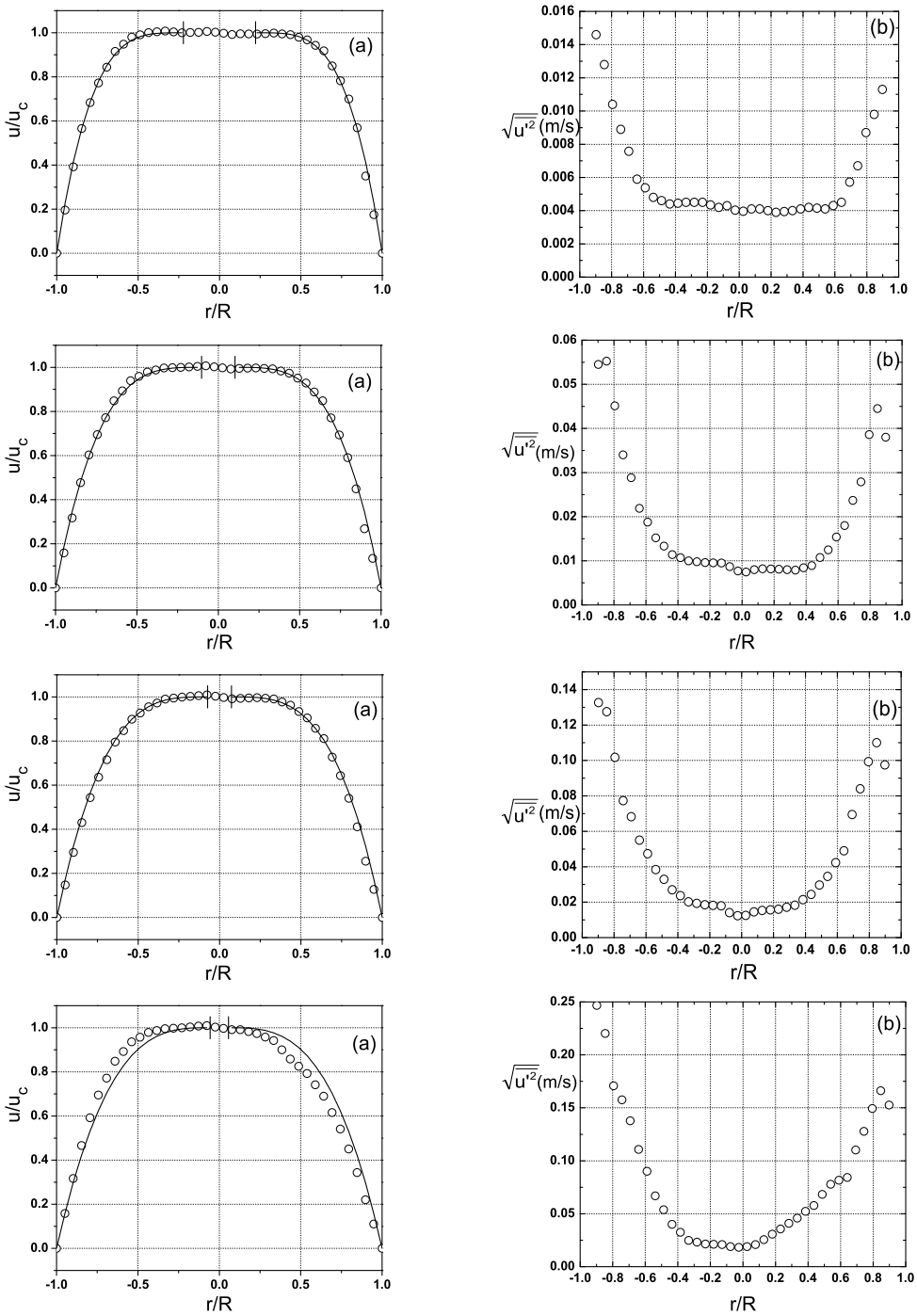

Figure B.11: (a) The time averaged velocity and (b) Local RMS velocity profiles for 0.1% Carbopol. From top to bottom; Re_G=5.5, Re_G=67, Re_G=378 and Re_G=937

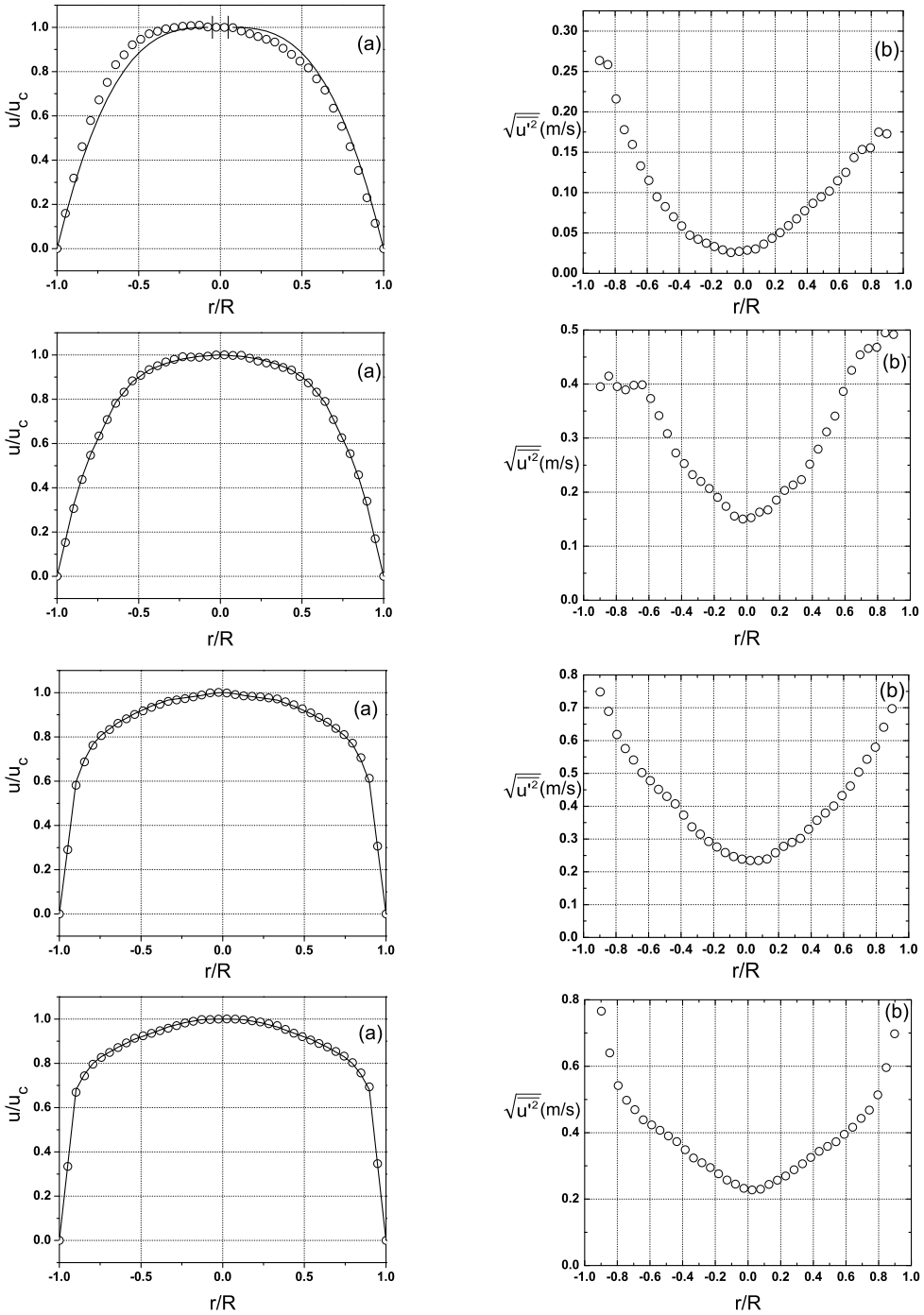

Figure B.12: (a) The time averaged velocity and (b) Local RMS velocity profiles for 0.1% Carbopol. From top to bottom; Re_G=1160, Re_G=1735, Re_G=2920 and Re_G=4488

Table B.11: Velocity readings for 0.1% Carbopol in Table B.10

	U_b=0.1120, ΔP=8.21		U_b=0.4622, ΔP=12.81		U_b=1.2076, ΔP=17.26		U_b=2.0461, ΔP=21.45	
r/R	$\overline{u}$	u'	$\overline{u}$	u'	$\overline{u}$	u'	$\overline{u}$	u'
-1	0	–	0	–	0	–	0	–
-0.94872	0.0309	–	0.11155	–	0.2829	–	0.53195	–
-0.89744	0.0618	0.0146	0.2231	0.0545	0.5658	0.1327	1.0639	0.2467
-0.84615	0.0892	0.0128	0.33543	0.05524	0.82487	0.12758	1.56543	0.22024
-0.79487	0.1077	0.0104	0.42383	0.04512	1.04277	0.10179	1.98897	0.17081
-0.74359	0.1218	0.0089	0.4883	0.034	1.2195	0.0773	2.3345	0.1575
-0.69231	0.13305	0.00758	0.54205	0.02883	1.3722	0.06824	2.5922	0.13779
-0.64103	0.1443	0.0059	0.5958	0.0219	1.5249	0.055	2.8499	0.1107
-0.58974	0.14945	0.00538	0.62795	0.01877	1.6244	0.04739	2.9978	0.0901
-0.53846	0.1546	0.0048	0.6601	0.0152	1.7239	0.0384	3.1457	0.0669
-0.48718	0.1562	0.0046	0.6738	0.01334	1.7778	0.0329	3.21645	0.05377
-0.4359	0.1578	0.0044	0.6875	0.0114	1.8317	0.027	3.2872	0.04
-0.38462	0.15835	0.00445	0.6941	0.01071	1.8652	0.02367	3.31595	0.03247
-0.33333	0.1589	0.0045	0.7007	0.01	1.8987	0.0202	3.3447	0.0248
-0.28205	0.1583	0.0045	0.70145	0.0098	1.9075	0.01935	3.3513	0.02315
-0.23077	0.1577	0.0045	0.7022	0.0096	1.9163	0.0185	3.3579	0.0215

Continued on next page

Table B.11 – continued from previous page

r/R	$\overline{u}$	u'	$\overline{u}$	u'	$\overline{u}$	u'	$\overline{u}$	u'
-0.17949	0.15785	0.00435	0.7039	0.00955	1.9228	0.0182	3.37185	0.0212
-0.12821	0.158	0.0042	0.7056	0.0095	1.9293	0.0179	3.3858	0.0209
-0.07692	0.1586	0.0043	0.7073	0.0087	1.9356	0.0141	3.3924	0.019
-0.02564	0.15807	0.00403	0.70423	0.0077	1.92367	0.01236	3.36993	0.01833
0.02564	0.15733	0.00397	0.7009	0.00747	1.91223	0.01251	3.34923	0.01897
0.07692	0.1564	0.0041	0.6973	0.008	1.9013	0.0145	3.3303	0.0209
0.12821	0.1569	0.0041	0.699	0.0082	1.9048	0.0153	3.3311	0.0256
0.17949	0.1568	0.004	0.69985	0.00815	1.908	0.01565	3.30105	0.0307
0.23077	0.1567	0.0039	0.7007	0.0081	1.9112	0.016	3.271	0.0357
0.28205	0.15705	0.00395	0.6992	0.008	1.90575	0.01715	3.21815	0.04089
0.33333	0.1574	0.004	0.6977	0.0079	1.9003	0.0183	3.1653	0.0459
0.38462	0.15685	0.0041	0.6908	0.00841	1.8729	0.0214	3.02415	0.05224
0.4359	0.1563	0.0042	0.6839	0.0089	1.8455	0.0244	2.883	0.0578
0.48718	0.15445	0.00415	0.66835	0.01075	1.79025	0.02969	2.7731	0.0683
0.53846	0.1526	0.0041	0.6528	0.0125	1.735	0.0346	2.6632	0.0778
0.58974	0.14865	0.00431	0.6243	0.01541	1.6452	0.04232	2.4903	0.08162
0.64103	0.1447	0.0045	0.5958	0.018	1.5554	0.049	2.3174	0.0842
0.69231	0.134	0.00572	0.54155	0.02368	1.3948	0.06944	2.06795	0.11023
0.74359	0.1233	0.0067	0.4873	0.0279	1.2342	0.084	1.8185	0.1278

Continued on next page

Table B.11 – continued from previous page

r/R	$\overline{u}$	u'	$\overline{u}$	u'	$\overline{u}$	u'	$\overline{u}$	u'
0.79487	0.1103	0.0087	0.41497	0.03859	1.0368	0.09934	1.5133	0.14933
0.84615	0.0898	0.0098	0.31543	0.04449	0.78857	0.11002	1.15403	0.16615
0.89744	0.0552	0.0113	0.1887	0.038	0.4895	0.0975	0.7407	0.1527
0.94872	0.0276	–	0.09435	–	0.24475	–	0.37035	–
1	0	–	0	–	0	–	0	–

Table B.12: Velocity readings for 0.1% Carbopol in Table B.10

	U_b=2.3218, ΔP=22.95		U_b=3.1146, ΔP=26.3		U_b=3.9005, ΔP=36.16		U_b=4.3967, ΔP=42.05	
r/R	$\overline{u}$	u'	$\overline{u}$	u'	$\overline{u}$	u'	$\overline{u}$	u'
-1	0	–	0	–	0	–	0	–
-0.94872	0.6059	–	0.7598	–	1.5335	–	1.9277	–
-0.89744	1.2118	0.2635	1.5196	0.3951	3.067	0.7484	3.8554	0.7658
-0.84615	1.75427	0.25845	2.16853	0.4148	3.62187	0.6888	4.2836	0.64026
-0.79487	2.20253	0.21594	2.71013	0.39542	4.01543	0.61842	4.58617	0.54157
-0.74359	2.5566	0.1779	3.1444	0.3895	4.2477	0.5756	4.7631	0.4977
-0.69231	2.85925	0.15957	3.5086	0.39786	4.39465	0.54078	4.89165	0.4692
-0.64103	3.1619	0.1329	3.8728	0.3986	4.5416	0.5023	5.0202	0.4385
-0.58974	3.33275	0.11503	4.12535	0.37324	4.648	0.47763	5.1411	0.42335
-0.53846	3.5036	0.0946	4.3779	0.3416	4.7544	0.4513	5.262	0.407
-0.48718	3.59825	0.08268	4.5021	0.30819	4.8381	0.42976	5.3259	0.39036
-0.4359	3.6929	0.07	4.6263	0.2724	4.9218	0.4072	5.3898	0.3732
-0.38462	3.73595	0.05869	4.71385	0.25291	4.99345	0.37278	5.45655	0.3488
-0.33333	3.779	0.0471	4.8014	0.2325	5.0651	0.3372	5.5233	0.3237
-0.28205	3.80085	0.04223	4.85915	0.21983	5.09685	0.31495	5.58995	0.30952
-0.23077	3.8227	0.0373	4.9169	0.2068	5.1286	0.2924	5.6566	0.2949

Continued on next page

Table B.12 – continued from previous page

r/R	$\overline{u}$	u'	$\overline{u}$	u'	$\overline{u}$	u'	$\overline{u}$	u'
-0.17949	3.832	0.03321	4.9096	0.19028	5.17275	0.27566	5.70185	0.27632
-0.12821	3.8413	0.0291	4.9023	0.1738	5.2169	0.2586	5.7471	0.2574
-0.07692	3.8104	0.0259	4.9285	0.1556	5.2684	0.2466	5.7506	0.245
-0.02564	3.80613	0.02717	4.95437	0.15015	5.2796	0.23881	5.76	0.23261
0.02564	3.8024	0.0286	4.96007	0.15258	5.26583	0.2347	5.76343	0.22753
0.07692	3.7992	0.0302	4.9456	0.1629	5.2271	0.2343	5.7609	0.2298
0.12821	3.7421	0.0363	4.9493	0.1672	5.1954	0.2389	5.7446	0.2444
0.17949	3.69355	0.04345	4.88465	0.18552	5.1841	0.25824	5.71465	0.25712
0.23077	3.645	0.0504	4.82	0.2033	5.1728	0.2775	5.6847	0.2697
0.28205	3.59825	0.05912	4.7781	0.2133	5.1472	0.28962	5.6381	0.28822
0.33333	3.5515	0.0676	4.7362	0.2231	5.1216	0.3016	5.5915	0.3064
0.38462	3.44495	0.07757	4.6766	0.2518	5.05235	0.32969	5.4932	0.32564
0.4359	3.3384	0.0868	4.617	0.2797	4.9831	0.3569	5.3949	0.344
0.48718	3.2229	0.09469	4.4741	0.3116	4.88735	0.37948	5.30495	0.35859
0.53846	3.1074	0.1018	4.3312	0.3409	4.7916	0.4009	5.215	0.3725
0.58974	2.91705	0.11465	4.1237	0.38631	4.68065	0.43206	5.12565	0.39495
0.64103	2.7267	0.125	3.9162	0.4255	4.5697	0.4613	5.0363	0.4164
0.69231	2.4144	0.14344	3.5098	0.45407	4.4208	0.5042	4.917	0.44309
0.74359	2.1021	0.1534	3.1034	0.4658	4.2719	0.5432	4.7977	0.468

Continued on next page

Table B.12 – continued from previous page

r/R	$\overline{u}$	u'	$\overline{u}$	u'	$\overline{u}$	u'	$\overline{u}$	u'
0.79487	1.75403	0.15538	2.7454	0.46812	4.06997	0.58009	4.62597	0.51376
0.84615	1.34563	0.17481	2.27257	0.49486	3.72387	0.64063	4.35943	0.59607
0.89744	0.8769	0.1727	1.6849	0.4917	3.2336	0.6974	3.9981	0.6979
0.94872	0.43845	–	0.84245	–	1.6168	–	1.99905	–
1	0	–	0	–	0	–	0	–

$U(m/s)$	$\dot{\gamma}(s^{-1})$	$\tau_y(Pa)$	$\kappa(Pa.s^n)$	n	$r_p(mm)$	Re_G	$T(^0C)$
0.3093	$0.2 - 62$	1.80	1.11	0.50	4.11	42	34
1.0233	$0.1 - 181$	1.58	0.71	0.53	2.90	397	34
1.5457	$0.1 - 267$	0.95	0.60	0.54	1.67	914	34.5
2.3849	$0.1 - 495$	0.90	0.50	0.54	–	2001	36.5
2.5912	$5 - 591$	0.90	0.50	0.54	–	2238	37
3.0411	$5 - 1063$	0.52	0.39	0.58	–	2612	38
3.5002	$3 - 1296$	0.30	0.26	0.65	–	3309	39

Table B.13: Flow conditions and Herschel-Bulkley parameters for 0.1% Carbopol

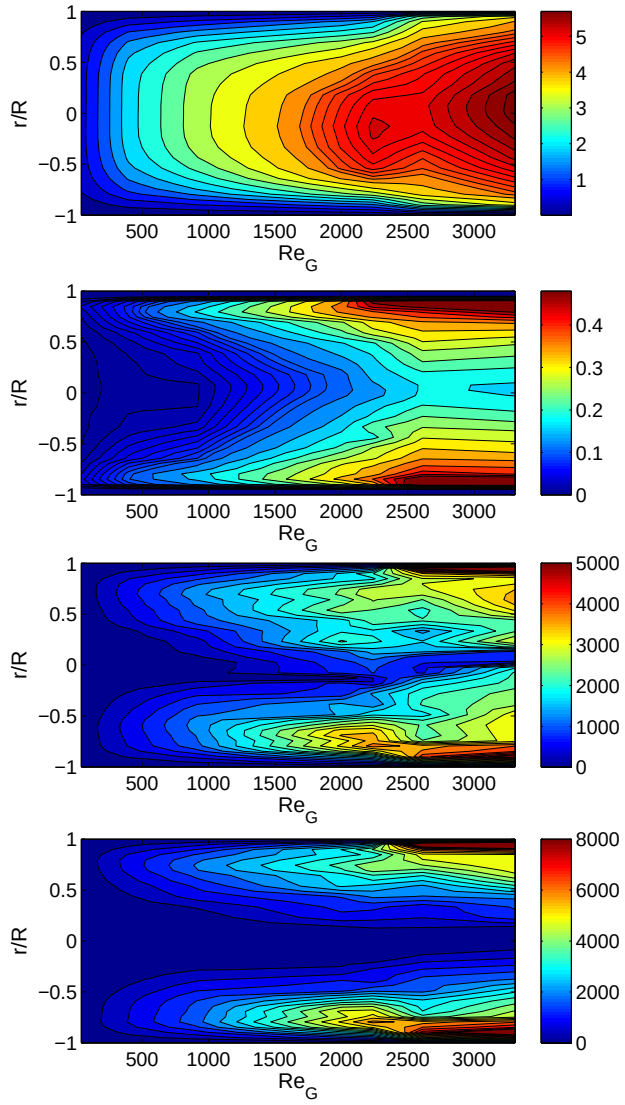

Figure B.13: From top to bottom; (a) Local velocity and (b) Local RMS velocity (c) $Re_{G,l}$ (d) ζ_G profiles for 0.1% Carbopol.

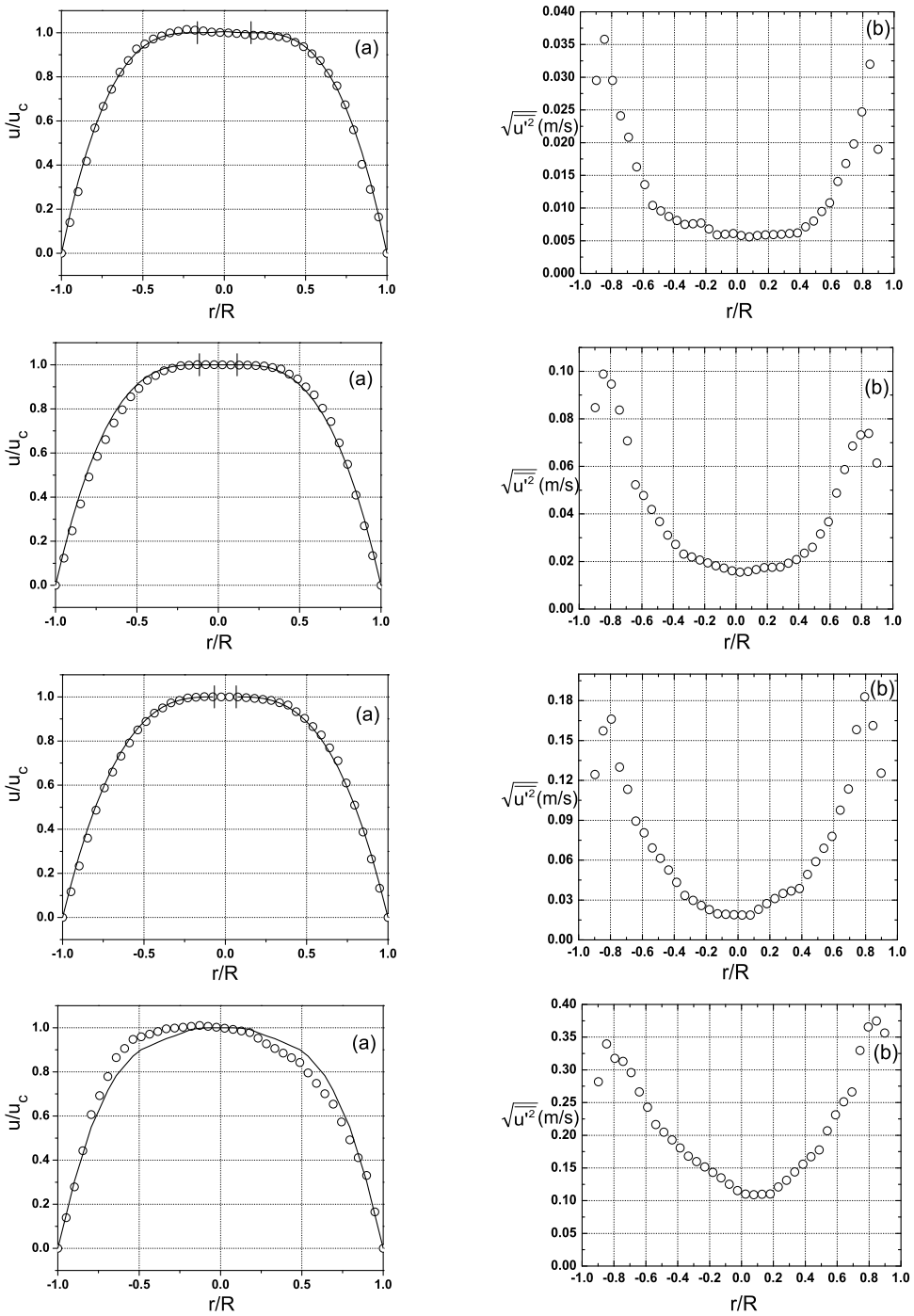

Figure B.14: (a) The time averaged velocity and (b) Local RMS velocity profiles for 0.1% Carbopol. From top to bottom; Re_G=42, Re_G=397, Re_G=914 and Re_G=2001

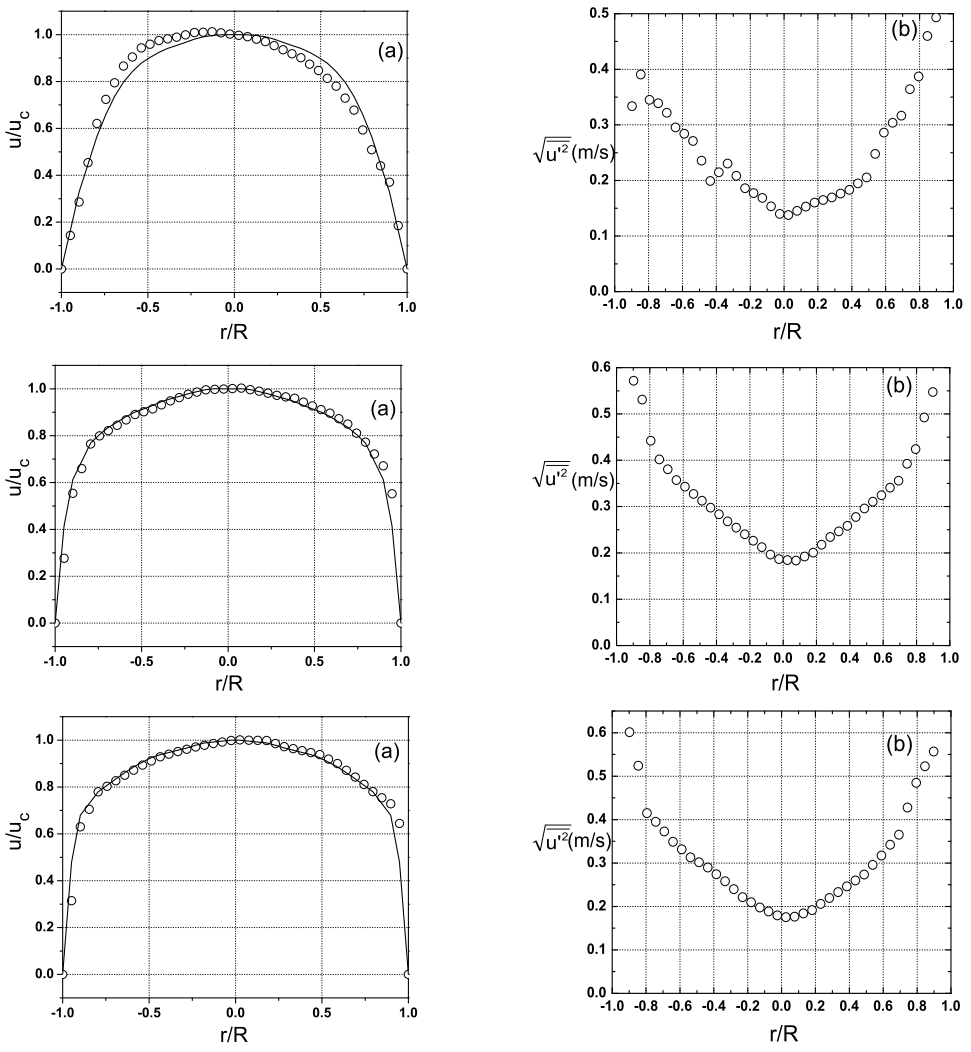

Figure B.15: (a) The time averaged velocity and (b) Local RMS velocity profiles for 0.1% Carbopol. From top to bottom; Re_G=2238, Re_G=2612 and Re_G=3309

Table B.14: Velocity readings for 0.1% Carbopol in Table B.13

	U_b=0.3093, ΔP=8.91		U_b=1.0233, ΔP=12.87		U_b=1.5457, ΔP=14.63		U_b=2.3849, ΔP=16.75	
r/R	$\overline{u}$	u'	$\overline{u}$	u'	$\overline{u}$	u'	$\overline{u}$	u'
-1	0	–	0	–	0	–	0	–
-0.94872	0.0674	–	0.2066	–	0.3016	–	0.5345	–
-0.89744	0.1348	0.0295	0.4132	0.0847	0.6032	0.1244	1.069	0.2818
-0.84615	0.2014	0.0358	0.6171	0.0988	0.9286	0.15725	1.69785	0.3397
-0.79487	0.274	0.0295	0.821	0.0946	1.254	0.1661	2.3267	0.3177
-0.74359	0.321	0.0241	0.978	0.0837	1.5151	0.13	2.6571	0.31296
-0.69231	0.3584	0.02083	1.10455	0.07073	1.70135	0.11328	2.9875	0.29583
-0.64103	0.3958	0.0163	1.2311	0.0523	1.8876	0.0894	3.3179	0.2663
-0.58974	0.42105	0.01358	1.33015	0.04775	2.04015	0.08051	3.4755	0.24293
-0.53846	0.4463	0.0104	1.4292	0.0419	2.1927	0.0692	3.6331	0.2163
-0.48718	0.4572	0.00958	1.4912	0.03679	2.29105	0.06137	3.6789	0.20476
-0.4359	0.4681	0.0087	1.5532	0.0311	2.3894	0.0526	3.7247	0.19286
-0.38462	0.47485	0.00811	1.58955	0.02721	2.4494	0.04326	3.7705	0.18061
-0.33333	0.4816	0.0075	1.6259	0.0231	2.5094	0.0334	3.8163	0.168
-0.28205	0.4853	0.0076	1.64495	0.02187	2.5381	0.0297	3.831	0.1598
-0.23077	0.489	0.0077	1.664	0.0206	2.5668	0.0259	3.8457	0.15154

Continued on next page

Table B.14 – continued from previous page

r/R	$\overline{u}$	u'	$\overline{u}$	u'	$\overline{u}$	u'	$\overline{u}$	u'
-0.17949	0.4875	0.0068	1.66775	0.0194	2.57435	0.02276	3.8604	0.1432
-0.12821	0.486	0.0059	1.6715	0.0182	2.5819	0.0196	3.8751	0.1348
-0.07692	0.4834	0.006	1.6717	0.01727	2.5797	0.01927	3.85998	0.12507
-0.02564	0.4823	0.0061	1.6718	0.0161	2.57875	0.0189	3.84486	0.1154
0.02564	0.4815	0.0058	1.671	0.01553	2.57887	0.0187	3.82747	0.1101
0.07692	0.4803	0.0056	1.6694	0.0158	2.5788	0.0187	3.8078	0.1091
0.12821	0.4781	0.0058	1.66905	0.0166	2.5699	0.02302	3.78005	0.10971
0.17949	0.4764	0.0059	1.6687	0.0174	2.561	0.0273	3.7523	0.1103
0.23077	0.47615	0.00595	1.6653	0.01755	2.54955	0.03112	3.6546	0.12106
0.28205	0.4759	0.006	1.6619	0.0177	2.5381	0.0349	3.5569	0.1311
0.33333	0.47325	0.0061	1.65045	0.01926	2.5108	0.03683	3.47575	0.14385
0.38462	0.4706	0.0062	1.639	0.0208	2.4835	0.0387	3.3946	0.15587
0.4359	0.46105	0.00712	1.6013	0.02347	2.40565	0.04918	3.31345	0.16715
0.48718	0.4515	0.008	1.5636	0.026	2.3278	0.0589	3.2323	0.1777
0.53846	0.4361	0.00946	1.5036	0.03161	2.231	0.06894	3.05117	0.20681
0.58974	0.4207	0.0108	1.4436	0.0367	2.1342	0.0779	2.87005	0.23128
0.64103	0.39335	0.01408	1.3424	0.04881	1.9831	0.09762	2.68893	0.25111
0.69231	0.366	0.0168	1.2412	0.0587	1.832	0.1135	2.5078	0.2663
0.74359	0.3246	0.0198	1.07925	0.06858	1.5731	0.1582	2.19765	0.32955

Continued on next page

Table B.14 – continued from previous page

r/R	$\overline{u}$	u'	$\overline{u}$	u'	$\overline{u}$	u'	$\overline{u}$	u'
0.79487	0.2699	0.0247	0.9173	0.0732	1.3142	0.1829	1.8875	0.36565
0.84615	0.1944	0.032	0.6839	0.07389	0.9989	0.1612	1.57735	0.3746
0.89744	0.1396	0.019	0.4505	0.0614	0.6836	0.1255	1.2672	0.3564
0.94872	0.07947	–	0.22525	–	0.3418	–	0.6336	–
1	0	–	0	–	0	–	0	–

Table B.15: Velocity readings for 0.1% Carbopol in Table B.13

	U_b=2.5912, ΔP=18.56		U_b=3.0411, ΔP=23.03		U_b=Ub=3.5002, ΔP=Ub=27.78	
r/R	$\overline{u}$	u'	$\overline{u}$	u'	$\overline{u}$	u'
-1	0	–	0	–	0	–
-0.94872	0.58435	–	1.12375	–	1.4347	–
-0.89744	1.1687	0.3338	2.2475	0.5719	2.8694	0.6012
-0.84615	1.85195	0.39048	2.6745	0.53089	3.21	0.52383
-0.79487	2.5352	0.345	3.1015	0.4421	3.5506	0.4149
-0.74359	2.9551	0.3389	3.241	0.402	3.65877	0.39483
-0.69231	3.24505	0.32171	3.3324	0.38055	3.76693	0.37283
-0.64103	3.535	0.2955	3.4238	0.3573	3.8751	0.3489
-0.58974	3.6925	0.28424	3.5167	0.34289	3.97275	0.33164
-0.53846	3.85	0.2709	3.6096	0.3272	4.0704	0.3131
-0.48718	3.91425	0.23565	3.65885	0.31275	4.1514	0.30169
-0.4359	3.9785	0.1991	3.7081	0.2978	4.2324	0.2896
-0.38462	4.00845	0.21469	3.77725	0.28332	4.28245	0.27407
-0.33333	4.0384	0.2305	3.8464	0.2681	4.3325	0.2581
-0.28205	4.07845	0.20844	3.904	0.25446	4.3776	0.24006
-0.23077	4.1185	0.1859	3.9616	0.2403	4.4227	0.2216

Continued on next page

Table B.15 – continued from previous page

r/R	$\overline{u}$	u'	$\overline{u}$	u'	$\overline{u}$	u'
-0.17949	4.1251	0.17731	3.9999	0.22645	4.4559	0.20965
-0.12821	4.1317	0.1687	4.0382	0.2123	4.4891	0.1975
-0.07692	4.11223	0.1534	4.04613	0.19632	4.51962	0.18856
-0.02564	4.09325	0.13989	4.0524	0.1866	4.55014	0.17949
0.02564	4.0718	0.13783	4.05917	0.18447	4.5622	0.1755
0.07692	4.0474	0.1454	4.0681	0.1836	4.5558	0.1767
0.12821	4.0046	0.15285	4.04205	0.19211	4.55175	0.18421
0.17949	3.9618	0.1601	4.016	0.2005	4.5477	0.1917
0.23077	3.8906	0.16494	3.97915	0.21763	4.4886	0.20587
0.28205	3.8194	0.1695	3.9423	0.2344	4.4295	0.2196
0.33333	3.7494	0.17644	3.9172	0.24654	4.3906	0.23304
0.38462	3.6794	0.183	3.8921	0.2585	4.3517	0.2462
0.4359	3.56815	0.19479	3.8263	0.2776	4.31325	0.26004
0.48718	3.4569	0.2055	3.7605	0.2959	4.2748	0.2736
0.53846	3.32105	0.24781	3.69695	0.31049	4.18765	0.29593
0.58974	3.1852	0.286	3.6334	0.3244	4.1005	0.3171
0.64103	2.9766	0.30381	3.53925	0.34081	3.96915	0.34227
0.69231	2.768	0.3165	3.4451	0.3559	3.8378	0.3651
0.74359	2.42255	0.36418	3.2886	0.39246	3.696	0.42793

Continued on next page

Table B.15 – continued from previous page

r/R	$\overline{u}$	u'	$\overline{u}$	u'	$\overline{u}$	u'
0.79487	2.0771	0.387	3.1321	0.424	3.5542	0.4849
0.84615	1.79535	0.45982	2.9273	0.49248	3.436	0.52281
0.89744	1.5136	0.4933	2.7225	0.5475	3.3178	0.557
0.94872	0.7568	–	2.2383	–	2.936	–
1	0	–	0	–	0	–

$U(m/s)$	$\dot{\gamma}(s^{-1})$	$\tau_y(Pa)$	$\kappa(Pa.s^n)$	n	$r_p(mm)$	Re_G	$T(^0C)$
0.1278	$0.1-29$	6.0	4.79	0.37	6.29	2.7	31
1.068	$1-201$	5.7	3.66	0.42	3.33	123	32
1.304	$2-235$	5.7	3.28	0.44	3.11	176	32
2.5573	$0.4-480$	5.6	2.87	0.46	2.40	561	35
3.6459	$1-849$	4.7	2.17	0.48	2.04	1120	39
3.7424	$2-1065$	1.7	1.7	0.48	–	1750	50
4.3054	$2-1609$	1.6	1.77	0.48	–	1804	45
4.8443	$8-1816$	0.72	0.93	0.52	–	2953	40

Table B.16: Flow conditions and Herschel-Bulkley parameters for 0.15% Carbopol

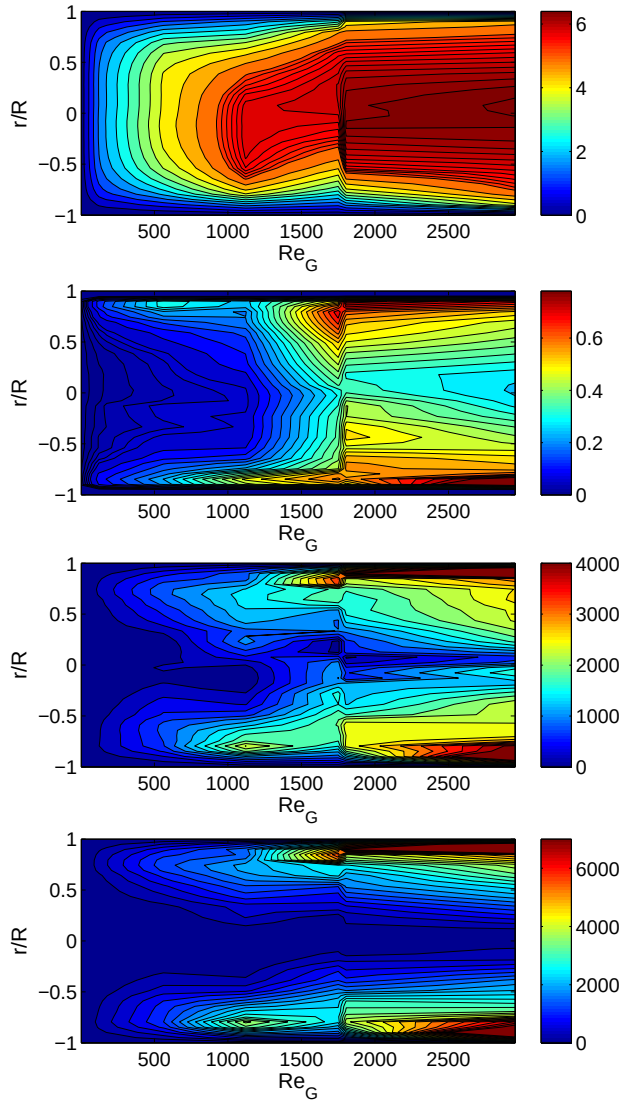

Figure B.16: From top to bottom; (a) Local velocity and (b) Local RMS velocity (c) $Re_{G,l}$ (d) ζ_G profiles for 0.15% Carbopol.

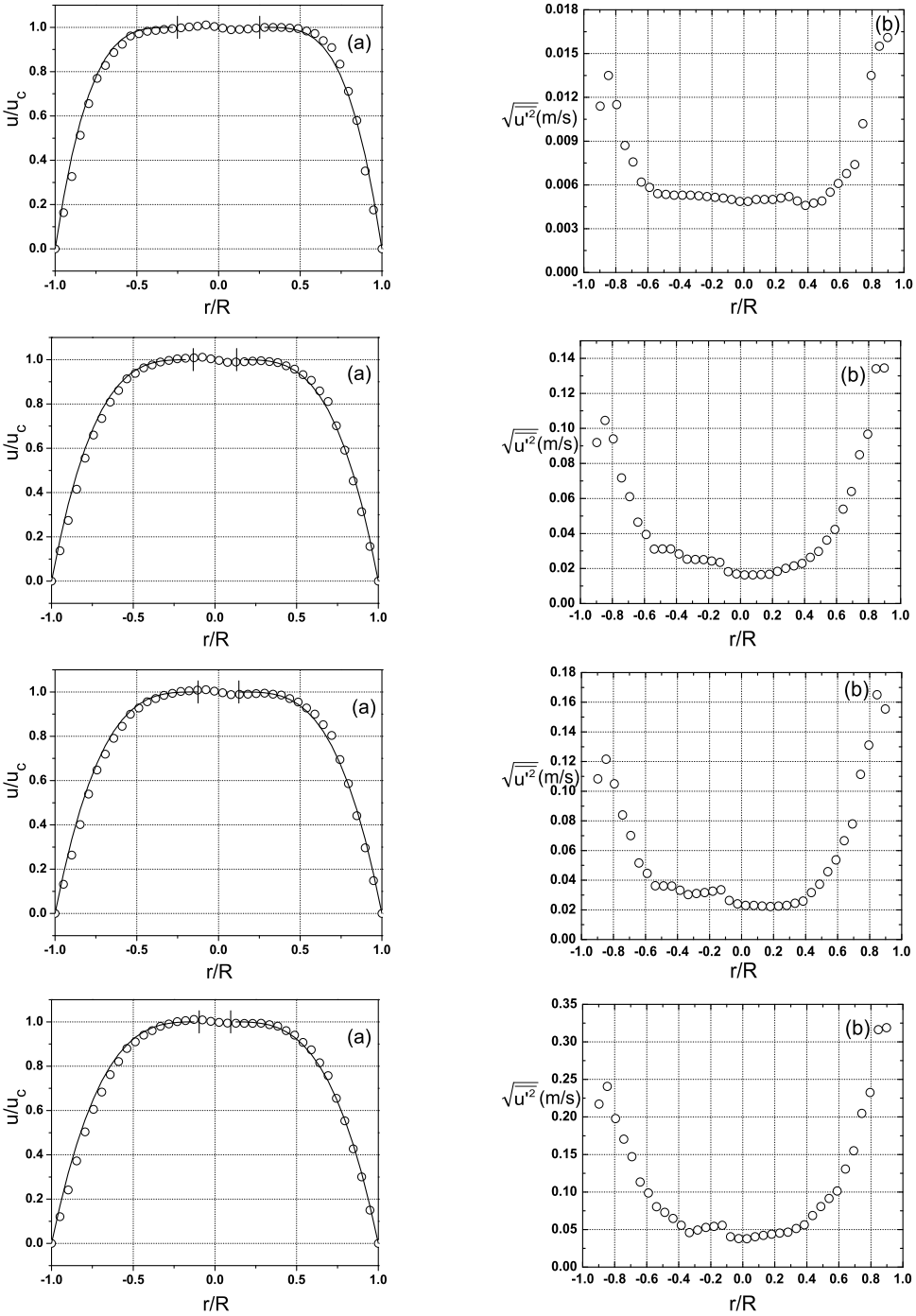

Figure B.17: (a) The time averaged velocity and (b) Local RMS velocity profiles for 0.15% Carbopol. From top to bottom; Re_G=2.7, Re_G=123, Re_G=176 and Re_G=561

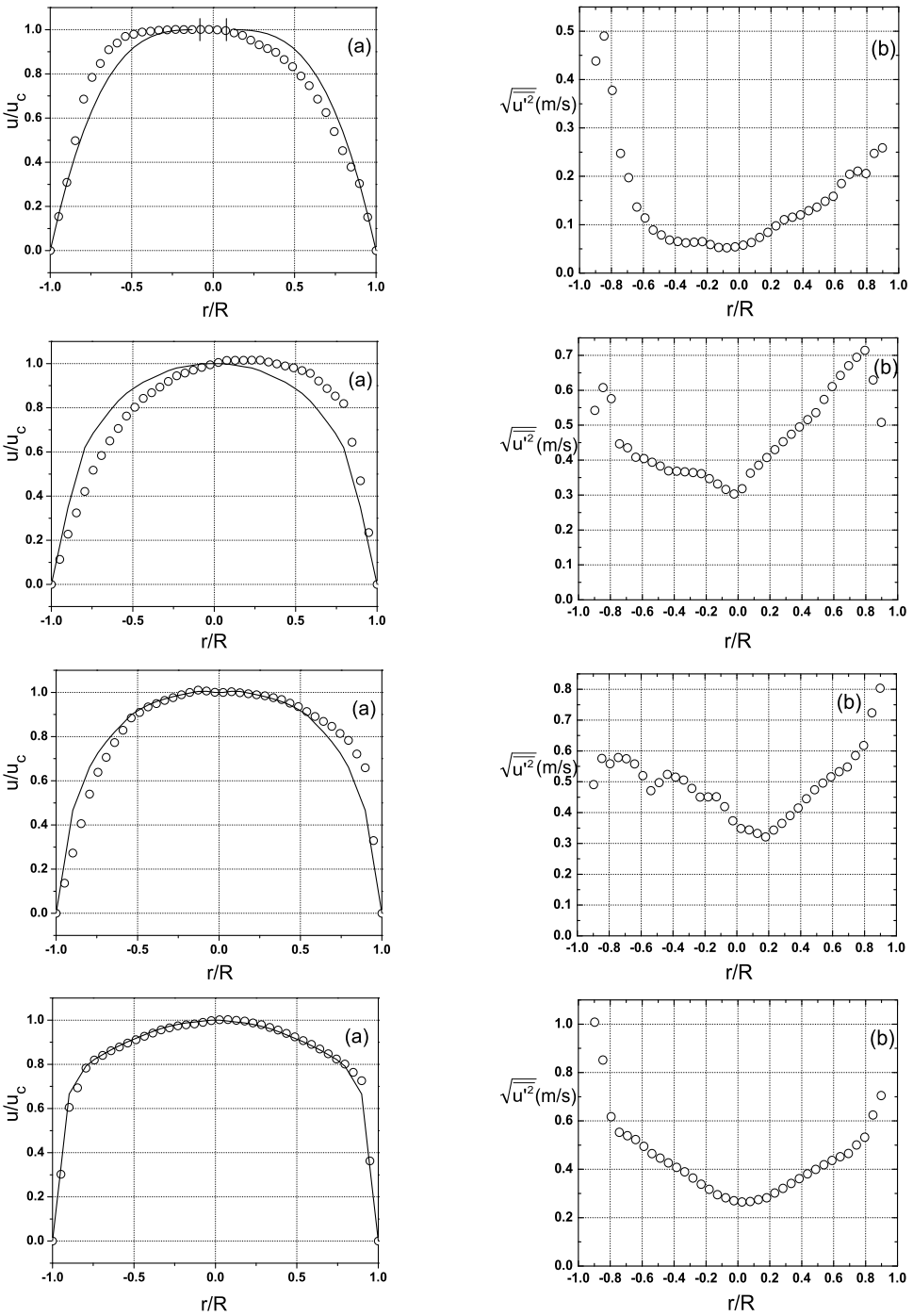

Figure B.18: (a) The time averaged velocity and (b) Local RMS velocity profiles for 0.15% Carbopol. From top to bottom; Re_G=1120, Re_G=1750, Re_G=1804 and Re_G=2953

Table B.17: Velocity readings for 0.15% Carbopol in Table B.16

	U_b=0.1278, ΔP=19.01		U_b=1.068, ΔP=33.43		U_b=1.304, ΔP=34.59		U_b=2.5573, ΔP=41.66	
r/R	$\overline{u}$	u'	$\overline{u}$	u'	$\overline{u}$	u'	$\overline{u}$	u'
-1	0	–	0	–	0	–	0	–
-0.94872	0.0296	–	0.2257	–	0.2679	–	0.49575	–
-0.89744	0.0592	0.0114	0.4514	0.0919	0.5358	0.1083	0.9915	0.2172
-0.84615	0.0929	0.0135	0.6825	0.10459	0.81605	0.12155	1.5307	0.2408
-0.79487	0.1187	0.0115	0.9136	0.094	1.0963	0.105	2.0699	0.1978
-0.74359	0.1394	0.0087	1.085	0.0717	1.3173	0.084	2.4864	0.1704
-0.69231	0.14995	0.00758	1.20705	0.061	1.46285	0.07011	2.80735	0.14708
-0.64103	0.1605	0.0062	1.3291	0.0465	1.6084	0.0516	3.1283	0.1134
-0.58974	0.1673	0.00583	1.4155	0.03942	1.719	0.04458	3.37115	0.09865
-0.53846	0.1741	0.0054	1.5019	0.0311	1.8296	0.0362	3.614	0.0805
-0.48718	0.17595	0.00535	1.54305	0.03117	1.88715	0.03614	3.73795	0.07299
-0.4359	0.1778	0.0053	1.5842	0.0312	1.9447	0.036	3.8619	0.0648
-0.38462	0.1786	0.0053	1.6055	0.02829	1.974	0.0332	3.9444	0.05557
-0.33333	0.1794	0.0053	1.6268	0.0253	2.0033	0.0303	4.0269	0.0459
-0.28205	0.18005	0.00525	1.6389	0.0252	2.02115	0.031	4.06905	0.04937
-0.23077	0.1807	0.0052	1.651	0.0251	2.039	0.0317	4.1112	0.0529

Continued on next page

Table B.17 – continued from previous page

r/R	$\overline{u}$	u'	$\overline{u}$	u'	$\overline{u}$	u'	$\overline{u}$	u'
-0.17949	0.18135	0.00515	1.6548	0.0243	2.0446	0.0326	4.13165	0.05424
-0.12821	0.182	0.0051	1.6586	0.0235	2.0502	0.0335	4.1521	0.0556
-0.07692	0.1831	0.005	1.6624	0.0182	2.0548	0.0263	4.144	0.0405
-0.02564	0.18177	0.00487	1.65073	0.01693	2.04147	0.02403	4.11753	0.03789
0.02564	0.18043	0.00487	1.6382	0.01633	2.02643	0.02293	4.09773	0.03787
0.07692	0.1791	0.005	1.6248	0.0164	2.0097	0.023	4.0846	0.0404
0.12821	0.1794	0.005	1.62715	0.01655	2.01155	0.0226	4.0817	0.04215
0.17949	0.1797	0.005	1.6295	0.0167	2.0134	0.0222	4.0788	0.0439
0.23077	0.1804	0.0051	1.63325	0.0184	2.0182	0.0226	4.0807	0.0452
0.28205	0.1811	0.0052	1.637	0.0201	2.023	0.023	4.0826	0.0465
0.33333	0.18105	0.0049	1.62985	0.02151	2.01395	0.02446	4.0554	0.05138
0.38462	0.181	0.0046	1.6227	0.0229	2.0049	0.0259	4.0282	0.0562
0.4359	0.18055	0.00475	1.5985	0.02641	1.9734	0.0317	3.9455	0.06874
0.48718	0.1801	0.0049	1.5743	0.0298	1.9419	0.0373	3.8628	0.0807
0.53846	0.1781	0.00551	1.5328	0.03625	1.8865	0.04578	3.72565	0.0915
0.58974	0.1761	0.0061	1.4913	0.0423	1.8311	0.0537	3.5885	0.1013
0.64103	0.1703	0.00678	1.4126	0.05392	1.7333	0.0667	3.3499	0.13067
0.69231	0.1645	0.0074	1.3339	0.064	1.6355	0.0779	3.1113	0.1549
0.74359	0.151	0.0102	1.15325	0.085	1.4138	0.11141	2.69165	0.20473

Continued on next page

Table B.17 – continued from previous page

r/R	$\overline{u}$	u'	$\overline{u}$	u'	$\overline{u}$	u'	$\overline{u}$	u'
0.79487	0.1288	0.0135	0.9726	0.0967	1.1921	0.1311	2.272	0.2325
0.84615	0.105	0.0155	0.7441	0.13404	0.89745	0.1651	1.7525	0.3163
0.89744	0.0637	0.0161	0.5156	0.1345	0.6028	0.1555	1.233	0.3189
0.94872	0.03185	–	0.2578	–	0.3014	–	0.6165	–
1	0	–	0	–	0	–	0	–

Table B.18: Velocity readings for 0.15% Carbopol in Table B.16

	U_b=3.6459, ΔP=44.25		U_b=3.7424, ΔP=		U_b=4.3054, ΔP=50.46		U_b=4.8443, ΔP=50.75	
r/R	$\overline{u}$	u'	$\overline{u}$	u'	$\overline{u}$	u'	$\overline{u}$	u'
-1	0	–	0	–	0	–	0	–
-0.94872	0.89145	–	0.66295	–	0.8541	–	1.9405	–
-0.89744	1.7829	0.4384	1.3259	0.5422	1.7082	0.491	3.881	1.0079
-0.84615	2.8714	0.48997	1.8866	0.60773	2.5439	0.57569	4.45125	0.85155
-0.79487	3.9599	0.3777	2.4473	0.57593	3.3796	0.5582	5.0215	0.6172
-0.74359	4.5268	0.2474	3.008	0.4468	3.9993	0.5787	5.2574	0.5529
-0.69231	4.8868	0.1972	3.39365	0.43531	4.41965	0.57458	5.3911	0.53865
-0.64103	5.2468	0.1367	3.7793	0.4082	4.84	0.5581	5.5248	0.523
-0.58974	5.42085	0.11383	4.10725	0.4042	5.18935	0.51993	5.6374	0.49473
-0.53846	5.5949	0.0892	4.4352	0.3939	5.5387	0.4712	5.75	0.4649
-0.48718	5.6522	0.07881	4.66735	0.38306	5.69505	0.4971	5.8472	0.44599
-0.4359	5.7095	0.0682	4.8995	0.3691	5.8514	0.5237	5.9444	0.4262
-0.38462	5.73265	0.06536	5.0482	0.36822	5.94325	0.51486	6.0377	0.40808
-0.33333	5.7558	0.0625	5.1969	0.36662	6.0351	0.5055	6.131	0.3892
-0.28205	5.76615	0.06385	5.3456	0.36432	6.1141	0.47829	6.1902	0.36418
-0.23077	5.7765	0.0652	5.4943	0.3613	6.1931	0.4502	6.2494	0.3386

Continued on next page

Table B.18 – continued from previous page

r/R	$\overline{u}$	u'	$\overline{u}$	u'	$\overline{u}$	u'	$\overline{u}$	u'
-0.17949	5.77445	0.05905	5.5689	0.34675	6.26015	0.45094	6.27755	0.317
-0.12821	5.7724	0.0529	5.6435	0.33169	6.3272	0.4516	6.3057	0.2952
-0.07692	5.7768	0.0525	5.7181	0.3161	6.3011	0.4195	6.3513	0.2823
-0.02564	5.77627	0.05423	5.78677	0.30313	6.26497	0.37337	6.4021	0.26983
0.02564	5.76677	0.05781	5.8472	0.31835	6.25803	0.34828	6.42773	0.26467
0.07692	5.7483	0.0632	5.8994	0.3626	6.2803	0.3438	6.4282	0.267
0.12821	5.6855	0.07382	5.90172	0.38505	6.2523	0.33251	6.4082	0.27473
0.17949	5.6227	0.0842	5.90405	0.40751	6.2243	0.3213	6.3882	0.2824
0.23077	5.49925	0.09769	5.90637	0.43	6.1945	0.34321	6.3345	0.30189
0.28205	5.3758	0.1105	5.9087	0.4525	6.1647	0.3649	6.2808	0.321
0.33333	5.2778	0.11563	5.85735	0.47402	6.11205	0.39004	6.2049	0.34145
0.38462	5.1798	0.1205	5.806	0.49509	6.0594	0.4147	6.129	0.3613
0.4359	4.9919	0.12888	5.75465	0.51572	5.95795	0.44498	6.02925	0.38102
0.48718	4.804	0.1363	5.7033	0.5359	5.8565	0.474	5.9295	0.3999
0.53846	4.5578	0.14849	5.63095	0.57377	5.7168	0.49571	5.82125	0.41889
0.58974	4.3116	0.1586	5.5586	0.6105	5.5771	0.5158	5.713	0.4369
0.64103	3.9588	0.18501	5.35962	0.64247	5.4375	0.53266	5.5746	0.45178
0.69231	3.606	0.2044	5.16065	0.67044	5.2979	0.548	5.4362	0.4654
0.74359	3.1095	0.2107	4.96167	0.69442	5.0997	0.58509	5.2882	0.50028

Continued on next page

Table B.18 – continued from previous page

r/R	$\overline{u}$	u'	$\overline{u}$	u'	$\overline{u}$	u'	$\overline{u}$	u'
0.79487	2.613	0.206	4.7627	0.7144	4.9015	0.6177	5.1402	0.5325
0.84615	2.18355	0.24728	3.7467	0.62957	4.5142	0.72395	4.8987	0.62441
0.89744	1.7541	0.259	2.7307	0.5081	4.1269	0.8036	4.6572	0.7048
0.94872	0.87705	–	1.36535	–	2.06345	–	2.3286	–
1	0	–	0	–	0	–	0	–

$U(m/s)$	$\dot{\gamma}(s^{-1})$	$\tau_y(Pa)$	$\kappa(Pa.s^n)$	n	$r_p(mm)$	Re_G	$T(^0C)$
0.3902	$0.6-70$	0.38	0.37	0.58	1.89	170	30
0.7227	$0.1-131$	0.30	0.29	0.60	1.29	526	30
1.0754	$3-195$	0.28	0.26	0.61	1.01	984	30
1.4977	$7-290$	0.23	0.22	0.62	–	1770	31
1.697	$2-358$	0.21	0.21	0.63	–	2089	32
2.4452	$0.1-864$	0.12	0.16	0.65	–	3442	34
2.9218	$6-1075$	0.045	0.12	0.68	–	5134	36

Table B.19: Flow conditions and Herschel-Bulkley parameters for 0.075% Carbopol

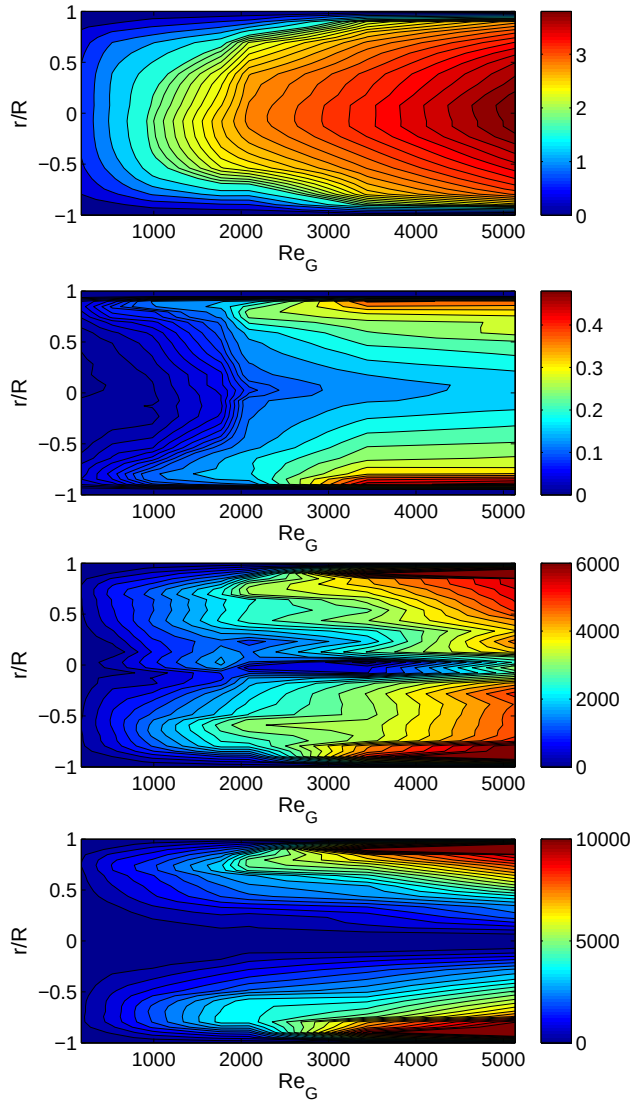

Figure B.19: From top to bottom; (a) Local velocity and (b) Local RMS velocity (c) $Re_{G,l}$ (d) ζ_G profiles for 0.075% Carbopol.

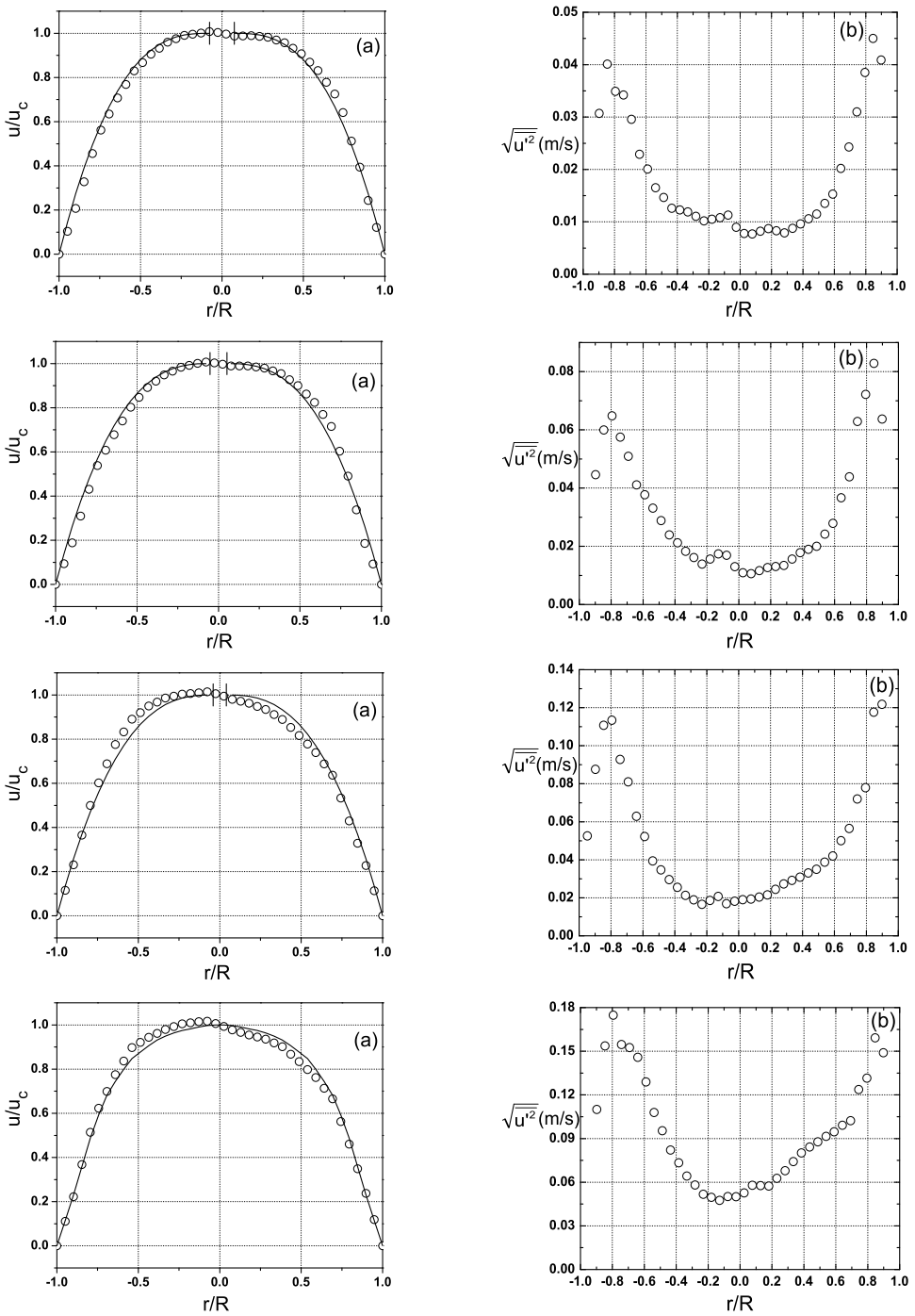

Figure B.20: (a) The time averaged velocity and (b) Local RMS velocity profiles for 0.075% Carbopol. From top to bottom; Re_G=170, Re_G=526, Re_G=984 and Re_G=1770

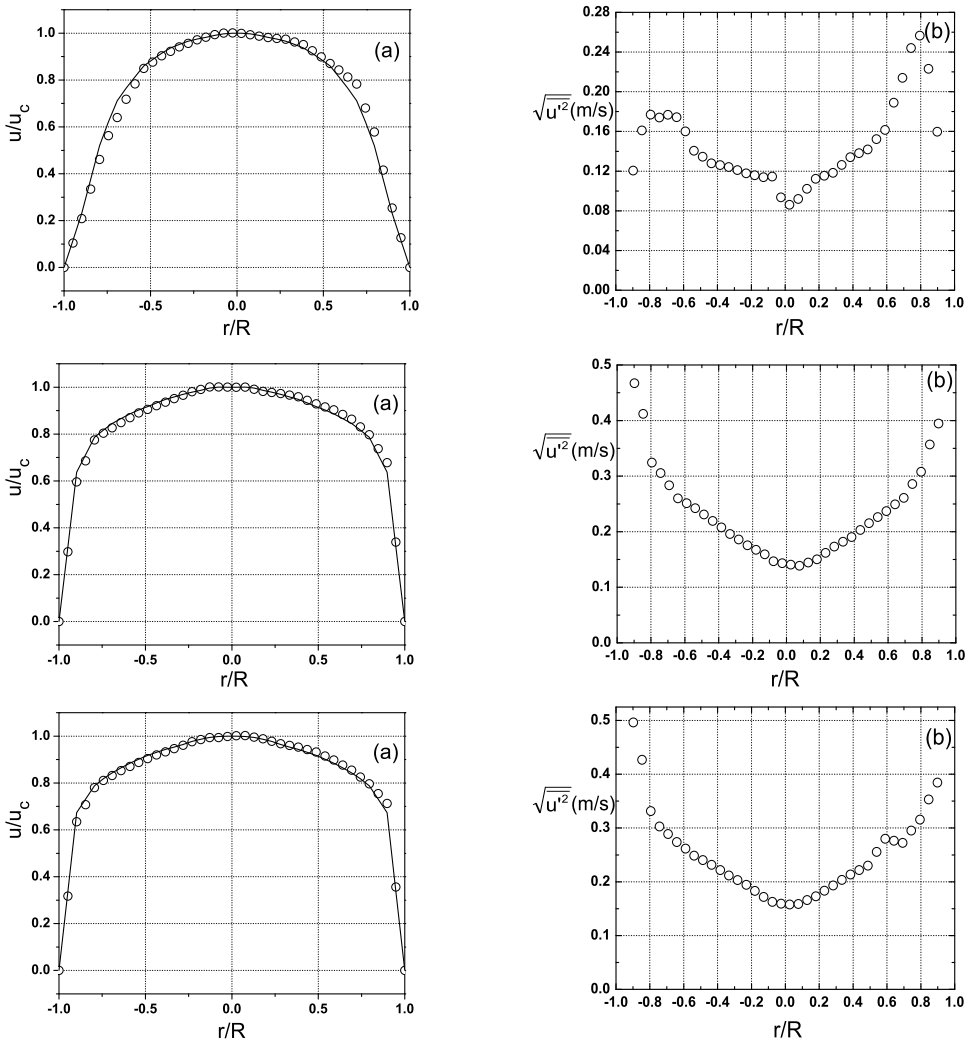

Figure B.21: (a) The time averaged velocity and (b) Local RMS velocity profiles for 0.075% Carbopol. From top to bottom; Re_G=2089, Re_G=3442 and Re_G=5134

Table B.20: Velocity readings for 0.075% Carbopol in Table B.19

	U_b=0.3902, ΔP=4.3		U_b=0.7227, ΔP=5.6		U_b=1.0754, ΔP=6.77		U_b=1.4977, ΔP=8.52	
r/R	$\overline{u}$	u'	$\overline{u}$	u'	$\overline{u}$	u'	$\overline{u}$	u'
-1	0	–	0	–	0	–	0	–
-0.94872	0.06855	–	0.11925	–	0.2149	0.0526	0.2837	–
-0.89744	0.1371	0.0307	0.2385	0.0446	0.4298	0.0876	0.5674	0.11
-0.84615	0.2169	0.0401	0.3921	0.05994	0.6798	0.11073	0.93955	0.15368
-0.79487	0.3015	0.0349	0.5457	0.0648	0.9298	0.1134	1.3117	0.1748
-0.74359	0.3718	0.0342	0.6814	0.0575	1.1205	0.0928	1.5892	0.1546
-0.69231	0.4198	0.02958	0.7701	0.05092	1.28195	0.08102	1.78335	0.15249
-0.64103	0.4678	0.0229	0.8588	0.0411	1.4434	0.0629	1.9775	0.1458
-0.58974	0.5083	0.02008	0.9375	0.0377	1.55035	0.05221	2.1339	0.12893
-0.53846	0.5488	0.0165	1.0162	0.0331	1.6573	0.0394	2.2903	0.1079
-0.48718	0.5737	0.01466	1.0727	0.02882	1.71265	0.03469	2.34935	0.09538
-0.4359	0.5986	0.0126	1.1292	0.0239	1.768	0.0296	2.4084	0.0821
-0.38462	0.61665	0.01227	1.1653	0.02121	1.80185	0.02554	2.45375	0.07334
-0.33333	0.6347	0.0119	1.2014	0.0183	1.8357	0.0213	2.4991	0.0642
-0.28205	0.64495	0.01107	1.2233	0.01614	1.85185	0.01897	2.5316	0.05804
-0.23077	0.6552	0.0102	1.2452	0.0139	1.868	0.0166	2.5641	0.0517

Continued on next page

Table B.20 – continued from previous page

r/R	$\overline{u}$	u'	$\overline{u}$	u'	$\overline{u}$	u'	$\overline{u}$	u'
-0.17949	0.65865	0.0105	1.2563	0.01564	1.8738	0.01864	2.5765	0.04961
-0.12821	0.6621	0.0108	1.2674	0.0174	1.8796	0.0207	2.5889	0.0475
-0.07692	0.6665	0.0113	1.2756	0.0169	1.8878	0.0169	2.594	0.0501
-0.02564	0.66363	0.00896	1.27027	0.01303	1.87213	0.01824	2.568	0.05004
0.02564	0.65907	0.00777	1.26267	0.01093	1.85103	0.01904	2.5347	0.05268
0.07692	0.6528	0.0077	1.2528	0.0106	1.8245	0.0193	2.4941	0.0579
0.12821	0.65355	0.0082	1.25295	0.01165	1.808	0.02041	2.465	0.05766
0.17949	0.6543	0.0087	1.2531	0.0127	1.7915	0.0215	2.4359	0.0574
0.23077	0.65195	0.0083	1.2469	0.01305	1.76525	0.02445	2.41145	0.06271
0.28205	0.6496	0.0079	1.2407	0.0134	1.739	0.0273	2.387	0.0679
0.33333	0.6414	0.00876	1.2246	0.01563	1.69685	0.02916	2.34305	0.07414
0.38462	0.6332	0.0096	1.2085	0.0178	1.6547	0.0309	2.2991	0.0801
0.4359	0.6167	0.01058	1.1744	0.01895	1.58725	0.0331	2.21355	0.08422
0.48718	0.6002	0.0115	1.1403	0.02	1.5198	0.035	2.128	0.0878
0.53846	0.57495	0.01351	1.092	0.02417	1.4475	0.03877	2.03555	0.09154
0.58974	0.5497	0.0153	1.0437	0.0279	1.3752	0.042	1.9431	0.0946
0.64103	0.5147	0.0202	0.9748	0.03665	1.2802	0.05006	1.8203	0.09916
0.69231	0.4797	0.0243	0.9059	0.0439	1.1852	0.0565	1.6975	0.1023
0.74359	0.4239	0.031	0.76355	0.06287	0.9927	0.07198	1.43585	0.12367

Continued on next page

Table B.20 – continued from previous page

r/R	$\overline{u}$	u'	$\overline{u}$	u'	$\overline{u}$	u'	$\overline{u}$	u'
0.79487	0.3386	0.0385	0.6212	0.0722	0.8002	0.0779	1.1742	0.1315
0.84615	0.2608	0.045	0.4282	0.08287	0.6122	0.11769	0.8904	0.15921
0.89744	0.1611	0.0409	0.2352	0.0637	0.4242	0.1218	0.6066	0.149
0.94872	0.08055	–	0.1176	–	0.2121	–	0.3033	–
1	0	–	0	–	0	–	0	–

Table B.21: Velocity readings for 0.075% Carbopol in Table B.19

	U_b=1.697, ΔP=9.03		U_b=2.4452, ΔP=16.24		U_b=2.9218, ΔP=21.09	
r/R	$\overline{u}$	u'	$\overline{u}$	u'	$\overline{u}$	u'
-1	0	–	0	–	0	–
-0.94872	0.295	–	0.9731	–	1.2284	–
-0.89744	0.59	0.1206	1.9462	0.4672	2.4568	0.4964
-0.84615	0.9471	0.16106	2.2383	0.41218	2.7382	0.42689
-0.79487	1.3042	0.177	2.5304	0.3245	3.0196	0.3314
-0.74359	1.5913	0.174	2.6246	0.3055	3.1379	0.3028
-0.69231	1.811	0.17678	2.69855	0.28359	3.2192	0.2889
-0.64103	2.0307	0.1744	2.7725	0.26	3.3005	0.2739
-0.58974	2.2173	0.16006	2.83925	0.25145	3.3685	0.26166
-0.53846	2.4039	0.1406	2.906	0.2422	3.4365	0.2487
-0.48718	2.47995	0.13457	2.95675	0.23101	3.49785	0.24042
-0.4359	2.556	0.1279	3.0075	0.2193	3.5592	0.2317
-0.38462	2.6103	0.12614	3.05615	0.20789	3.611	0.22189
-0.33333	2.6646	0.1242	3.1048	0.196	3.6628	0.2117
-0.28205	2.7071	0.12108	3.15285	0.186	3.72075	0.20328
-0.23077	2.7496	0.1178	3.2009	0.1756	3.7787	0.1945

Continued on next page

Table B.21 – continued from previous page

r/R	$\overline{u}$	u'	$\overline{u}$	u'	$\overline{u}$	u'
-0.17949	2.78125	0.11589	3.23495	0.16755	3.8124	0.18322
-0.12821	2.8129	0.1139	3.269	0.1593	3.8461	0.1717
-0.07692	2.8317	0.1146	3.2677	0.1468	3.8472	0.1628
-0.02564	2.83343	0.09361	3.26523	0.14347	3.86487	0.15928
0.02564	2.82633	0.08608	3.2645	0.14073	3.8758	0.15797
0.07692	2.8104	0.092	3.2655	0.1386	3.88	0.1589
0.12821	2.7936	0.10221	3.23595	0.14457	3.85335	0.16611
0.17949	2.7768	0.1123	3.2064	0.1504	3.8267	0.1732
0.23077	2.76675	0.11531	3.19135	0.16191	3.7858	0.18333
0.28205	2.7567	0.1183	3.1763	0.1733	3.7449	0.1932
0.33333	2.7242	0.12626	3.15395	0.18192	3.717	0.20344
0.38462	2.6917	0.134	3.1316	0.1904	3.6891	0.2135
0.4359	2.61725	0.13817	3.08205	0.20305	3.6481	0.22192
0.48718	2.5428	0.1419	3.0325	0.2152	3.6071	0.2301
0.53846	2.46445	0.15222	2.9905	0.2263	3.542	0.25554
0.58974	2.3861	0.1616	2.9485	0.237	3.4769	0.2799
0.64103	2.3006	0.18903	2.8842	0.24939	3.39225	0.27628
0.69231	2.2151	0.214	2.8199	0.261	3.3076	0.2725
0.74359	1.92575	0.24401	2.7113	0.2858	3.1947	0.29523

Continued on next page

Table B.21 – continued from previous page

r/R	$\overline{u}$	u'	$\overline{u}$	u'	$\overline{u}$	u'
0.79487	1.6364	0.2566	2.6027	0.3078	3.0818	0.3157
0.84615	1.17735	0.22319	2.4085	0.35707	2.9197	0.35305
0.89744	0.7183	0.1597	2.2143	0.3947	2.7576	0.3844
0.94872	0.35915	–	1.10715	–	1.3788	–
1	0	–	0	–	0	–

$U(m/s)$	$\dot{\gamma}(s^{-1})$	$\tau_y(Pa)$	$\kappa(Pa.s^n)$	n	$r_p(mm)$	Re_G	$T(^0C)$
0.1429	$0.1-24$	0.0065	0.0268	0.86	0.39	356	30
0.2792	$1-49$	0.0060	0.0188	0.86	0.29	1098	30
0.4108	$0.1-71$	0.0052	0.0173	0.88	0.18	1717	31
0.4736	$3-103$	0.0045	0.0153	0.90	–	2114	30
0.5102	$2-123$	0.0040	0.0133	0.90	–	2615	30
0.9108	$0.7-393$	0.0035	0.0110	0.91	–	5409	30
1.4876	$3-617$	0.0025	0.0090	0.92	–	10960	31

Table B.22: Flow conditions and Herschel-Bulkley parameters for 0.05% Carbopol

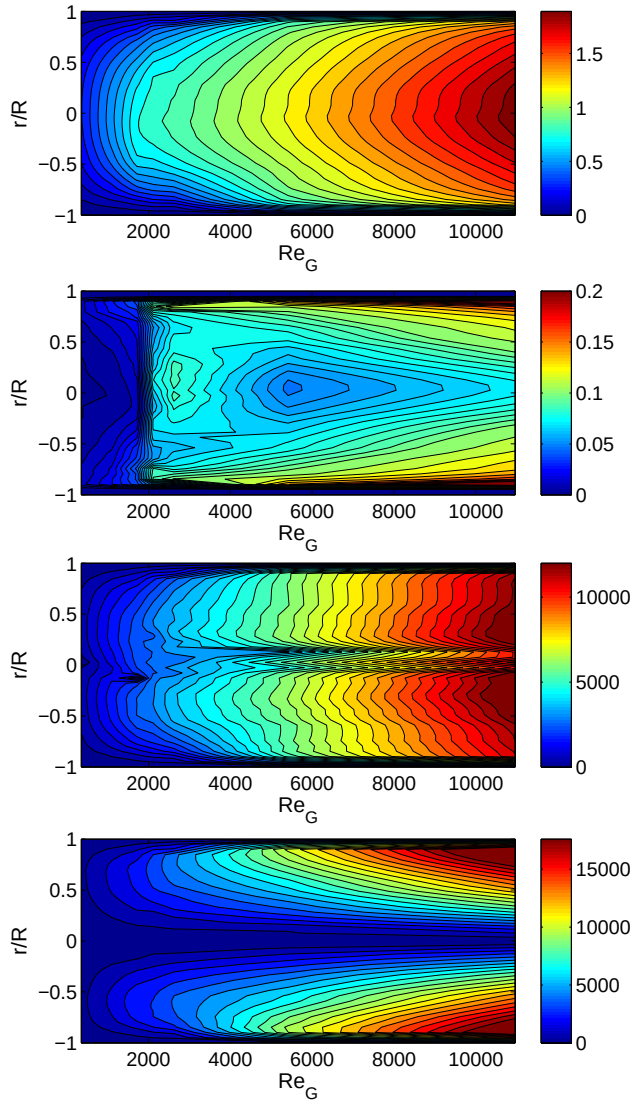

Figure B.22: From top to bottom; (a) Local velocity and (b) Local RMS velocity (c) $Re_{G,l}$ (d) ζ_G profiles for 0.05% Carbopol.

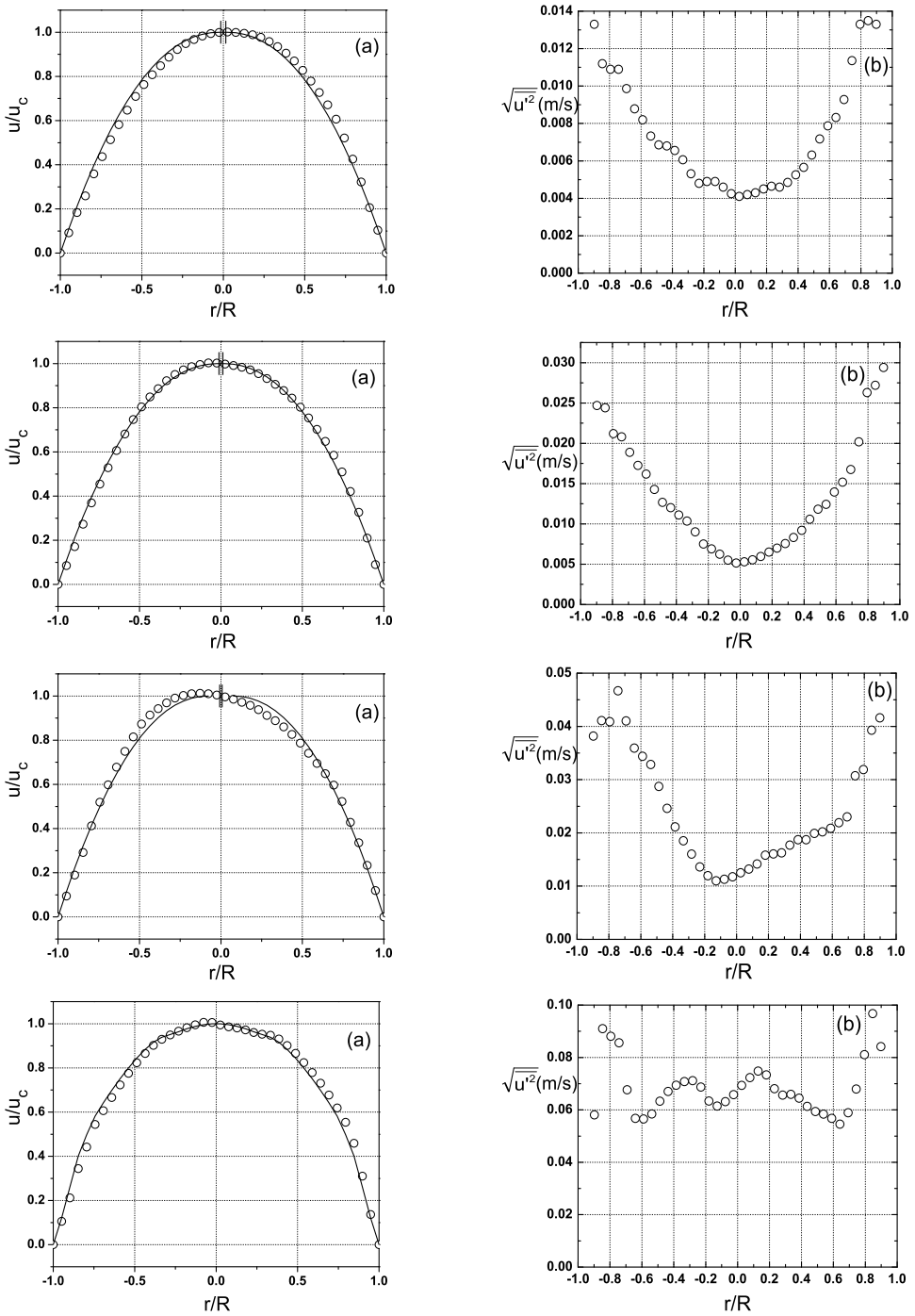

Figure B.23: (a) The time averaged velocity and (b) Local RMS velocity profiles for 0.05% Carbopol. From top to bottom; Re_G=356, Re_G=1098, Re_G=1717 and Re_G=2114

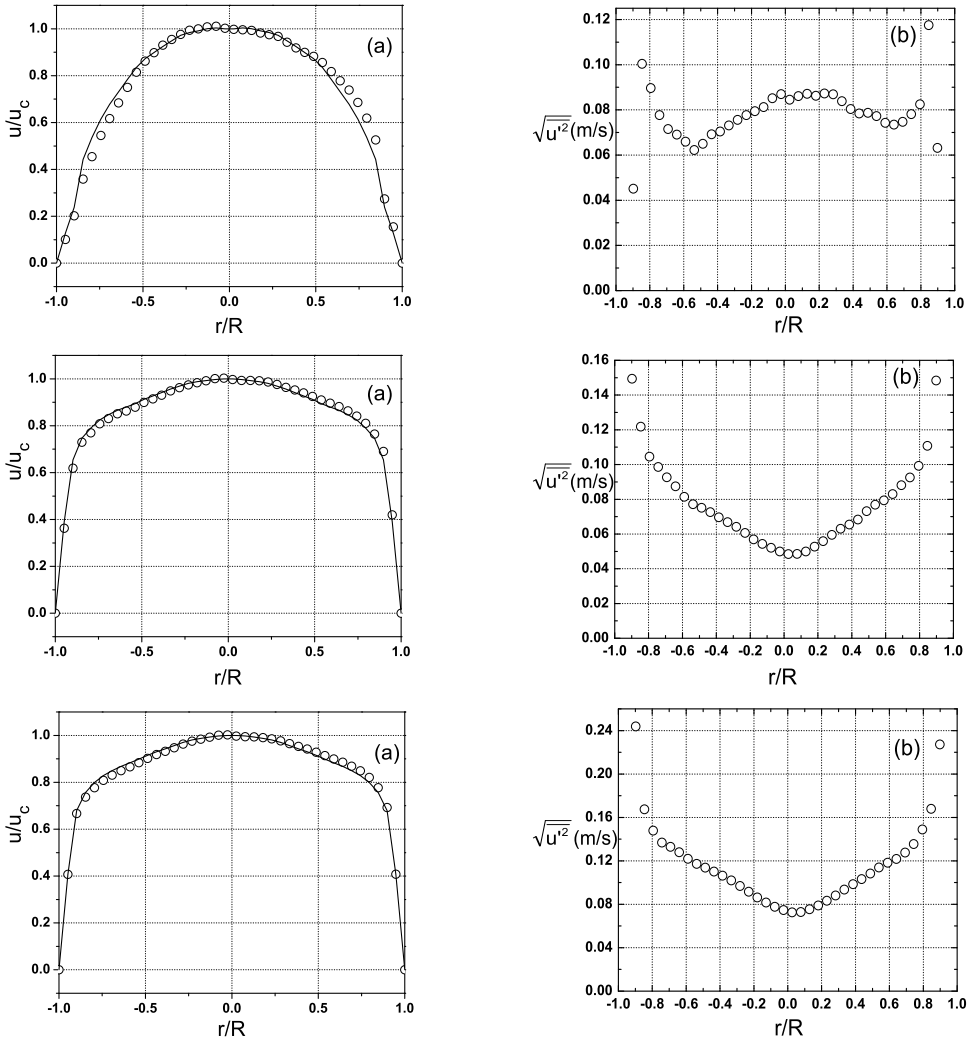

Figure B.24: (a) The time averaged velocity and (b) Local RMS velocity profiles for 0.05% Carbopol. From top to bottom; Re_G=2615, Re_G=5409 and Re_G=10960

Table B.23: Velocity readings for 0.05% Carbopol in Table B.22

	U_b=0.1429, ΔP=0.34		U_b=0.2792, ΔP=0.4		U_b=0.4108, ΔP=0.54		U_b=0.4736, ΔP=0.72	
r/R	$\overline{u}$	u'	$\overline{u}$	u'	$\overline{u}$	u'	$\overline{u}$	u'
-1	0	–	0	–	0	–	0	–
-0.94872	0.02525	–	0.04595	–	0.0716	–	0.08665	–
-0.89744	0.0505	0.0133	0.0919	0.0247	0.1432	0.0382	0.1733	0.0581
-0.84615	0.0713	0.0112	0.1463	0.0244	0.2208	0.0411	0.2817	0.091
-0.79487	0.0987	0.0109	0.1981	0.0212	0.3119	0.0409	0.3618	0.0881
-0.74359	0.1203	0.0109	0.2437	0.0208	0.3925	0.0467	0.4456	0.0856
-0.69231	0.14125	0.00986	0.28335	0.01888	0.45185	0.04105	0.49633	0.06768
-0.64103	0.16005	0.00878	0.32505	0.01725	0.5121	0.03592	0.54518	0.05678
-0.58974	0.1781	0.0082	0.3651	0.01618	0.56605	0.0344	0.59213	0.05653
-0.53846	0.19535	0.00733	0.40045	0.01428	0.61585	0.03284	0.63513	0.05847
-0.48718	0.21005	0.00686	0.4311	0.01267	0.66	0.02873	0.67417	0.06332
-0.4359	0.2223	0.0068	0.4552	0.01201	0.6908	0.0246	0.70862	0.06701
-0.38462	0.23345	0.00656	0.47535	0.01112	0.71255	0.02112	0.73847	0.06941
-0.33333	0.2441	0.00606	0.4947	0.01036	0.7323	0.01852	0.7613	0.07079
-0.28205	0.25375	0.00531	0.5096	0.00901	0.74855	0.01601	0.7771	0.07114
-0.23077	0.26115	0.0048	0.52085	0.0075	0.7572	0.0136	0.79138	0.0687

Continued on next page

Table B.23 – continued from previous page

r/R	$\overline{u}$	u'	$\overline{u}$	u'	$\overline{u}$	u'	$\overline{u}$	u'
-0.17949	0.2662	0.0049	0.5285	0.0069	0.7632	0.01195	0.80412	0.06335
-0.12821	0.27045	0.0049	0.534	0.00625	0.7651	0.011	0.81493	0.06144
-0.07692	0.2735	0.0046	0.5378	0.0055	0.7634	0.0113	0.82378	0.06314
-0.02564	0.27505	0.00425	0.5375	0.00515	0.7589	0.01175	0.82345	0.06581
0.02564	0.27545	0.0041	0.53485	0.0053	0.7524	0.0125	0.81395	0.06936
0.07692	0.27505	0.0042	0.53135	0.00555	0.74435	0.0132	0.8071	0.07234
0.12821	0.274	0.0043	0.52725	0.00595	0.73415	0.01416	0.8029	0.07479
0.17949	0.27215	0.0045	0.5208	0.0065	0.72375	0.0158	0.79605	0.07334
0.23077	0.26885	0.00465	0.5118	0.007	0.7087	0.01605	0.78655	0.06809
0.28205	0.2637	0.0046	0.5	0.00755	0.6892	0.01626	0.77998	0.06565
0.33333	0.25725	0.00485	0.48565	0.00831	0.67135	0.01771	0.77632	0.06595
0.38462	0.24925	0.00525	0.4705	0.00921	0.65	0.01871	0.7624	0.0645
0.4359	0.2395	0.00566	0.4525	0.01058	0.6244	0.01871	0.7382	0.06135
0.48718	0.22765	0.00632	0.4301	0.01182	0.5946	0.0199	0.70898	0.05937
0.53846	0.2143	0.00717	0.4041	0.01242	0.5598	0.02019	0.67472	0.05837
0.58974	0.20005	0.00787	0.37655	0.01396	0.52505	0.02087	0.63785	0.05677
0.64103	0.18485	0.00832	0.3475	0.01518	0.49	0.02192	0.59835	0.05457
0.69231	0.16695	0.00928	0.3137	0.01674	0.45075	0.02302	0.5546	0.05893
0.74359	0.14345	0.01136	0.27315	0.02018	0.39475	0.03074	0.5066	0.06798

Continued on next page

Table B.23 – continued from previous page

r/R	$\overline{u}$	u'	$\overline{u}$	u'	$\overline{u}$	u'	$\overline{u}$	u'
0.79487	0.1172	0.0133	0.2257	0.0263	0.3238	0.0319	0.4536	0.08109
0.84615	0.0886	0.0135	0.1751	0.0272	0.2538	0.0393	0.37593	0.09673
0.89744	0.0567	0.0133	0.1127	0.0294	0.1766	0.0416	0.2541	0.08417
0.94872	0.02863	–	0.04816	–	0.09033	–	0.11166	–
1	0	–	0	–	0	–	0	–

Table B.24: Velocity readings for 0.05% Carbopol in Table B.22

	U_b=0.5102, ΔP=0.97		U_b=0.9108, ΔP=2.72		U_b=1.4876, ΔP=5.56	
r/R	$\overline{u}$	u'	$\overline{u}$	u'	$\overline{u}$	u'
-1	0	–	0	–	0	–
-0.94872	0.086	–	0.4344	–	0.79027	–
-0.89744	0.172	0.0451	0.7415	0.1494	1.2933	0.2439
-0.84615	0.3056	0.1004	0.8746	0.1218	1.4289	0.1675
-0.79487	0.387	0.0897	0.9223	0.1046	1.5069	0.1479
-0.74359	0.4639	0.0777	0.9685	0.0986	1.5684	0.1368
-0.69231	0.52515	0.07155	0.99525	0.09265	1.6108	0.1329
-0.64103	0.5824	0.06907	1.01945	0.08744	1.6481	0.12792
-0.58974	0.63865	0.06597	1.0342	0.08142	1.6803	0.12192
-0.53846	0.69405	0.06227	1.0532	0.07718	1.7141	0.11719
-0.48718	0.7343	0.06499	1.07805	0.07517	1.7495	0.11379
-0.4359	0.76455	0.06922	1.09555	0.07261	1.781	0.11019
-0.38462	0.79205	0.07045	1.11485	0.06962	1.8086	0.10644
-0.33333	0.8125	0.07309	1.1368	0.06682	1.83773	0.10203
-0.28205	0.8314	0.0756	1.15355	0.06421	1.86838	0.09693
-0.23077	0.84615	0.0777	1.16775	0.06062	1.892	0.09164

Continued on next page

Table B.24 – continued from previous page

r/R	$\overline{u}$	u'	$\overline{u}$	u'	$\overline{u}$	u'
-0.17949	0.85145	0.07945	1.1786	0.05695	1.9086	0.08624
-0.12821	0.85835	0.08125	1.18875	0.05436	1.92515	0.0816
-0.07692	0.8607	0.08521	1.19925	0.05205	1.94165	0.07775
-0.02564	0.85325	0.087	1.20175	0.05	1.94485	0.07474
0.02564	0.84965	0.0845	1.1949	0.0485	1.93475	0.07264
0.07692	0.8481	0.08611	1.19015	0.0486	1.92905	0.0729
0.12821	0.8454	0.08715	1.19	0.05	1.92775	0.0755
0.17949	0.83595	0.08622	1.18845	0.0527	1.922	0.07897
0.23077	0.83	0.08725	1.18195	0.05586	1.9118	0.08327
0.28205	0.8241	0.08691	1.16935	0.05952	1.89512	0.08813
0.33333	0.8027	0.08383	1.15475	0.06306	1.87197	0.09348
0.38462	0.7819	0.08035	1.14125	0.06546	1.84922	0.09853
0.4359	0.766	0.07845	1.1266	0.06832	1.82688	0.10328
0.48718	0.75125	0.07872	1.1088	0.07318	1.80133	0.10841
0.53846	0.7288	0.07728	1.09005	0.07686	1.77258	0.11386
0.58974	0.69625	0.07429	1.074	0.07936	1.74495	0.11831
0.64103	0.6627	0.07348	1.05635	0.08298	1.71845	0.12181
0.69231	0.6294	0.07471	1.0344	0.08815	1.6856	0.12762
0.74359	0.5839	0.07816	1.008	0.09254	1.6464	0.13547

Continued on next page

Table B.24 – continued from previous page

r/R	$\overline{u}$	u'	$\overline{u}$	u'	$\overline{u}$	u'
0.79487	0.5268	0.0825	0.9711	0.0993	1.5928	0.14892
0.84615	0.4477	0.1175	0.9157	0.1108	1.50667	0.16796
0.89744	0.2337	0.0632	0.8274	0.1484	1.3424	0.22721
0.94872	0.1318	–	0.5028	–	0.79087	–
1	0	–	0	–	0	–

$U_b(m/s)$	$\dot{\gamma}(s^{-1})$	$\mu(Pa.s)$	Re_G	$T(^0C)$
0.3717	$1.8-60$	0.0306	731	24.5
0.5659	$0.6-88$	0.029	1174	25.5
0.8142	$4-127$	0.028	1737	26
1.0027	$0.7-159$	0.0274	2201	26.5
1.1301	$0.2-239$	0.025	2719	28
1.4268	$0.8-356$	0.024	3546	28.5

Table B.25: Flow conditions for 80% Glycerin

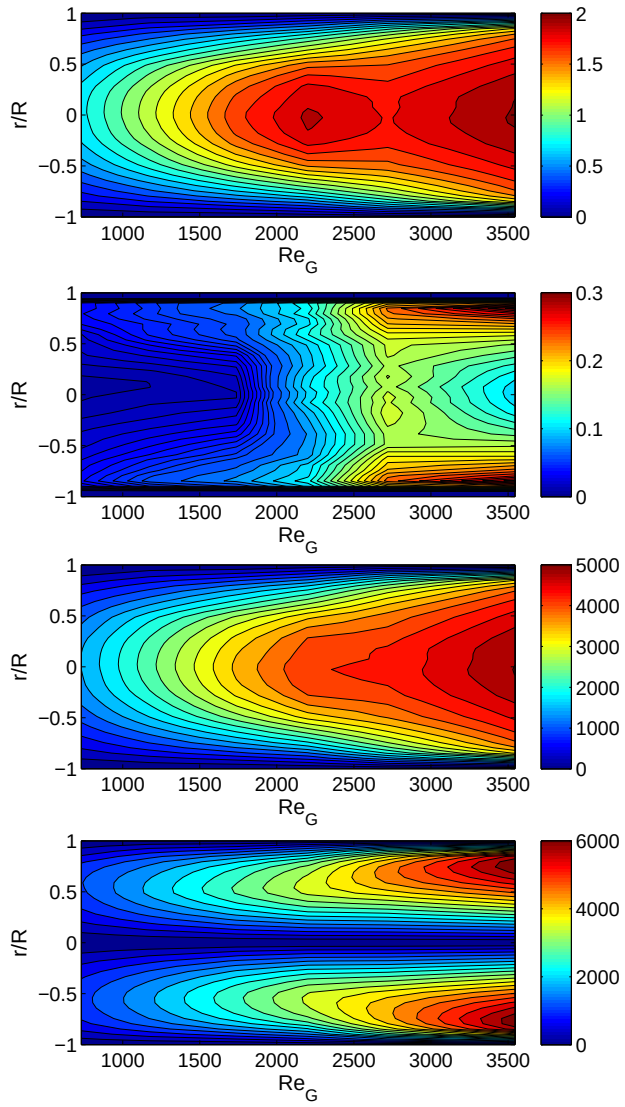

Figure B.25: From top to bottom; (a) Local velocity and (b) Local RMS velocity (c) $Re_{G,l}$ (d) ζ_G profiles for 80% Glycerin.

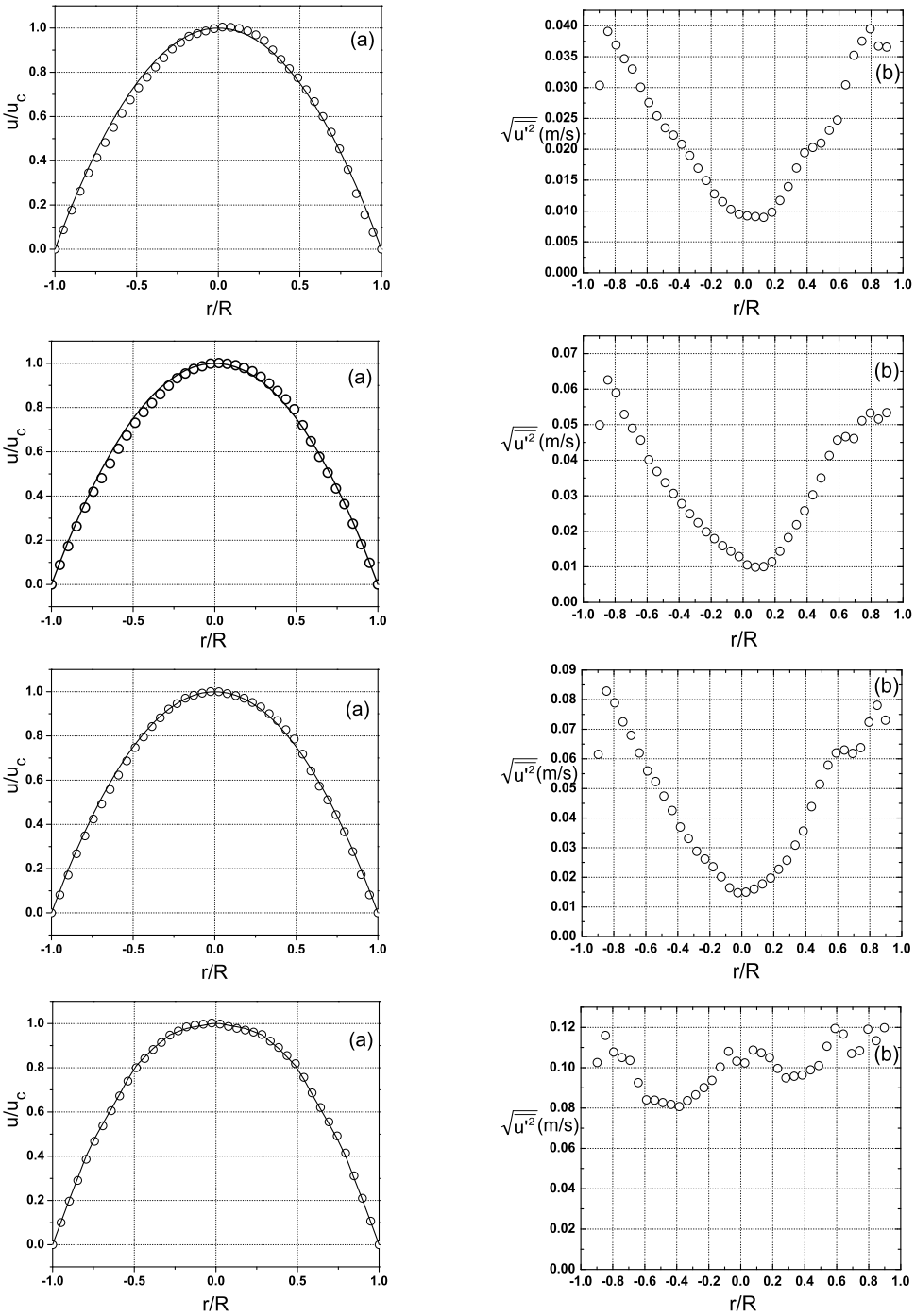

Figure B.26: (a) The time averaged velocity and (b) Local RMS velocity profiles for 80% Glycerin. From top to bottom; Re_G=731, Re_G=1174, Re_G=1737 and Re_G=2201

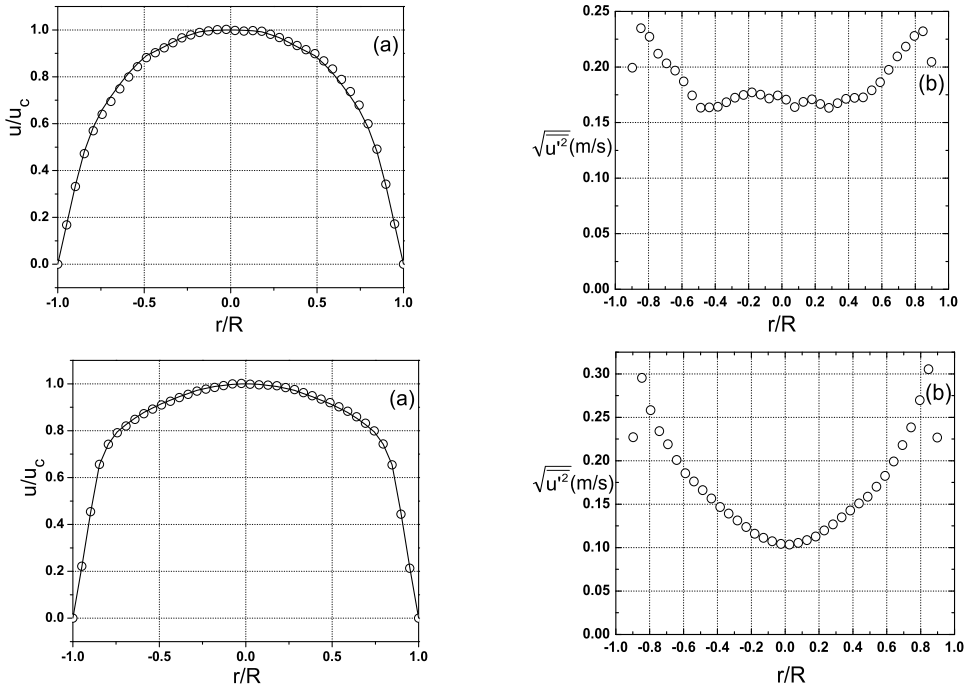

Figure B.27: (a) The time averaged velocity and (b) Local RMS velocity profiles for 80% Glycerin. From top to bottom; Re_G=2719 and Re_G=3546

Table B.26: Velocity readings for 80% Glycerin in Table B.25

	U_b=0.3717, ΔP=1.59		U_b=0.5659, ΔP=1.89		U_b=0.8142, ΔP=2.89		U_b=1.0027, ΔP=3.95	
r/R	$\overline{u}$	u'	$\overline{u}$	u'	$\overline{u}$	u'	$\overline{u}$	u'
-1	0	–	0	–	0	–	0	–
-0.94872	0.06753	–	0.10337	–	0.13618	–	0.19132	–
-0.89744	0.13502	0.03036	0.2012	0.04991	0.28527	0.06154	0.37788	0.10252
-0.84615	0.20055	0.03909	0.30561	0.06258	0.44541	0.08289	0.55812	0.11595
-0.79487	0.26418	0.03691	0.40487	0.05892	0.58018	0.07892	0.74231	0.10776
-0.74359	0.31653	0.03465	0.48776	0.05288	0.70633	0.07249	0.89816	0.10501
-0.69231	0.36879	0.03302	0.55853	0.04897	0.82045	0.06794	1.03315	0.10358
-0.64103	0.42141	0.03006	0.6359	0.04567	0.92905	0.06199	1.16335	0.09259
-0.58974	0.47016	0.02758	0.71363	0.04013	1.03721	0.05593	1.29255	0.08408
-0.53846	0.51669	0.02542	0.78282	0.03682	1.14475	0.05234	1.42035	0.08392
-0.48718	0.55854	0.02347	0.84965	0.03367	1.24533	0.04744	1.53628	0.08266
-0.4359	0.59504	0.02231	0.90505	0.03065	1.32503	0.04258	1.61658	0.08177
-0.38462	0.63021	0.02081	0.95333	0.02778	1.40354	0.037	1.69535	0.08074
-0.33333	0.66224	0.019	0.99997	0.02496	1.46885	0.03314	1.7572	0.08365
-0.28205	0.6929	0.01694	1.0446	0.02242	1.53416	0.02879	1.81905	0.08656
-0.23077	0.71469	0.01494	1.08366	0.01987	1.57611	0.02616	1.85602	0.09006

Continued on next page

Table B.26 – continued from previous page

r/R	$\overline{u}$	u'	$\overline{u}$	u'	$\overline{u}$	u'	$\overline{u}$	u'
-0.17949	0.73647	0.01277	1.10863	0.01792	1.61594	0.02357	1.89072	0.09368
-0.12821	0.7459	0.01151	1.13235	0.01593	1.63826	0.02017	1.90612	0.10034
-0.07692	0.7549	0.01026	1.14652	0.01442	1.65473	0.01647	1.91507	0.10806
-0.02564	0.76298	0.00948	1.16069	0.01288	1.6665	0.01479	1.92483	0.10319
0.02564	0.76857	0.00923	1.16377	0.01052	1.66498	0.01498	1.91675	0.1023
0.07692	0.7677	0.00911	1.15925	0.00993	1.65161	0.01602	1.89484	0.10872
0.12821	0.76359	0.00897	1.15163	0.01005	1.63555	0.01774	1.87933	0.10733
0.17949	0.75505	0.00981	1.13766	0.01147	1.61563	0.01976	1.86323	0.10495
0.23077	0.74143	0.01171	1.11967	0.01441	1.58415	0.02271	1.84537	0.09962
0.28205	0.72208	0.01397	1.09133	0.01824	1.55103	0.02575	1.82435	0.09488
0.33333	0.68936	0.01697	1.05612	0.02185	1.4998	0.03089	1.7685	0.09574
0.38462	0.65674	0.01943	1.0174	0.02578	1.44857	0.03562	1.71265	0.09636
0.4359	0.6248	0.0203	0.97263	0.03027	1.37927	0.04389	1.64251	0.09889
0.48718	0.59286	0.02098	0.9201	0.03499	1.30833	0.05147	1.57106	0.10105
0.53846	0.55196	0.0231	0.83642	0.0413	1.19555	0.05788	1.45288	0.11064
0.58974	0.51074	0.02474	0.75278	0.04566	1.06881	0.062	1.31913	0.11946
0.64103	0.45904	0.03044	0.67026	0.0466	0.95507	0.06298	1.19117	0.11664
0.69231	0.40472	0.03521	0.58774	0.04608	0.85063	0.06182	1.06733	0.10699
0.74359	0.3475	0.03751	0.50493	0.05111	0.74001	0.0638	0.94414	0.10845

Continued on next page

Table B.26 – continued from previous page

r/R	$\overline{u}$	u'	$\overline{u}$	u'	$\overline{u}$	u'	$\overline{u}$	u'
0.79487	0.27531	0.03953	0.42209	0.05326	0.61059	0.07239	0.79653	0.11906
0.84615	0.19223	0.03673	0.31913	0.05159	0.46087	0.07811	0.59831	0.11344
0.89744	0.11914	0.03654	0.21122	0.05337	0.2882	0.07306	0.40398	0.1198
0.94872	0.05848	–	0.11349	–	0.13532	–	0.20412	–
1	0	–	0	–	0	–	0	–

Table B.27: Velocity readings for 80% Glycerin in Table B.25

	U_b=1.1301, ΔP=5.58		U_b=1.4268, ΔP=10.2	
r/R	$\overline{u}$	u'	$\overline{u}$	u'
-1	0	–	0	–
-0.94872	0.30012	–	0.44695	–
-0.89744	0.59338	0.19941	0.91471	0.22716
-0.84615	0.84371	0.23495	1.32129	0.2954
-0.79487	1.01755	0.22716	1.49507	0.25829
-0.74359	1.14332	0.21201	1.59331	0.23404
-0.69231	1.24186	0.20323	1.65162	0.21893
-0.64103	1.33814	0.19682	1.70838	0.20084
-0.58974	1.42743	0.18705	1.75762	0.18568
-0.53846	1.50696	0.17439	1.79629	0.17608
-0.48718	1.57592	0.16341	1.83309	0.16615
-0.4359	1.61322	0.16374	1.86424	0.15651
-0.38462	1.65059	0.16424	1.89515	0.14668
-0.33333	1.68885	0.16829	1.9233	0.13912
-0.28205	1.72711	0.17236	1.95145	0.13127
-0.23077	1.74828	0.17485	1.96793	0.1237

Continued on next page

Table B.27 – continued from previous page

r/R	$\overline{u}$	u'	$\overline{u}$	u'
-0.17949	1.7679	0.17721	1.98335	0.11604
-0.12821	1.77972	0.17519	1.99828	0.11123
-0.07692	1.78895	0.17168	2.01305	0.10734
-0.02564	1.79054	0.17435	2.01672	0.1043
0.02564	1.78311	0.17058	2.01091	0.10356
0.07692	1.77799	0.164	2.00552	0.10545
0.12821	1.78108	0.16857	2.00294	0.10868
0.17949	1.77747	0.17093	1.99703	0.11285
0.23077	1.75375	0.16666	1.98115	0.11977
0.28205	1.72942	0.16316	1.96442	0.1267
0.33333	1.6985	0.1674	1.93825	0.13491
0.38462	1.66758	0.17138	1.91208	0.14285
0.4359	1.63653	0.1722	1.88219	0.15088
0.48718	1.60547	0.17262	1.85196	0.15862
0.53846	1.55087	0.17899	1.81626	0.1702
0.58974	1.48842	0.18631	1.77873	0.18255
0.64103	1.40885	0.19754	1.7306	0.19923
0.69231	1.31705	0.20945	1.6749	0.21802
0.74359	1.21423	0.21838	1.60978	0.23845

Continued on next page

Table B.27 – continued from previous page

r/R	$\overline{u}$	u'	$\overline{u}$	u'
0.79487	1.07089	0.22795	1.49764	0.26967
0.84615	0.87735	0.23215	1.31776	0.30547
0.89744	0.6101	0.20455	0.8947	0.2268
0.94872	0.30677	–	0.42985	–
1	0	–	0	–

$U_b(m/s)$	$\dot{\gamma}(s^{-1})$	$\mu(Pa.s)$	Re_G	$T(^0C)$
0.0564	$0.1-8$	0.0096	342	25.5
0.1045	$0.2-15$	0.0096	633	25.5
0.2943	$0.8-43$	0.0092	1860	26
0.3894	$0.5-63$	0.0088	2573	26.5
0.7791	$2-232$	0.0084	5393	27
1.4489	$2-482$	0.0080	10531	27.5

Table B.28: Flow conditions for 65% Glycerin

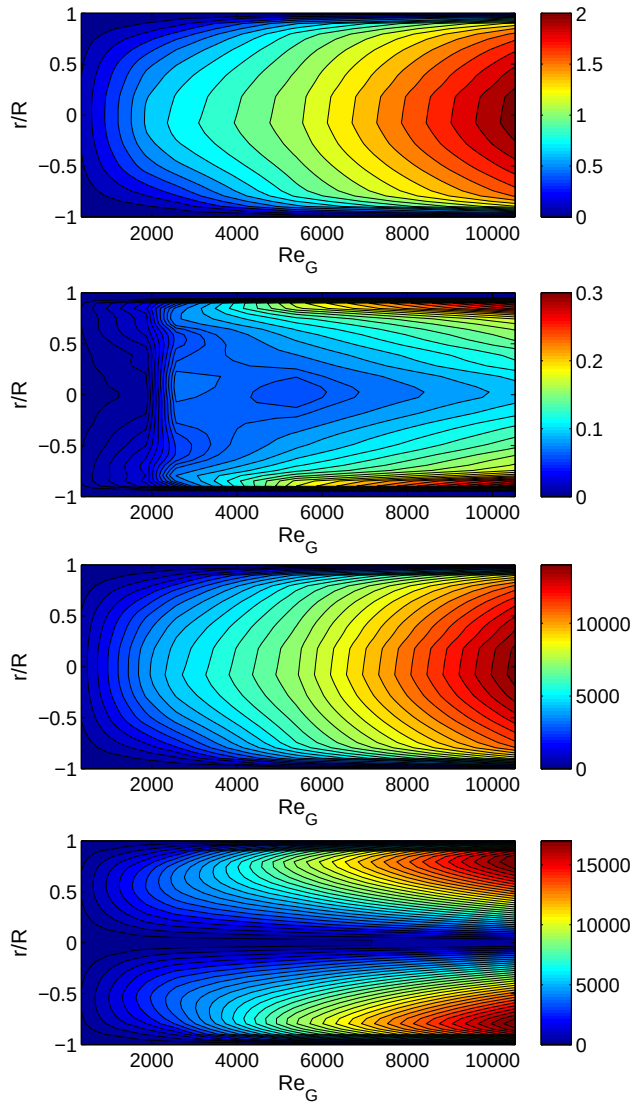

Figure B.28: From top to bottom; (a) Local velocity and (b) Local RMS velocity (c) $Re_{G,l}$ (d) ζ_G profiles for 65% Glycerin.

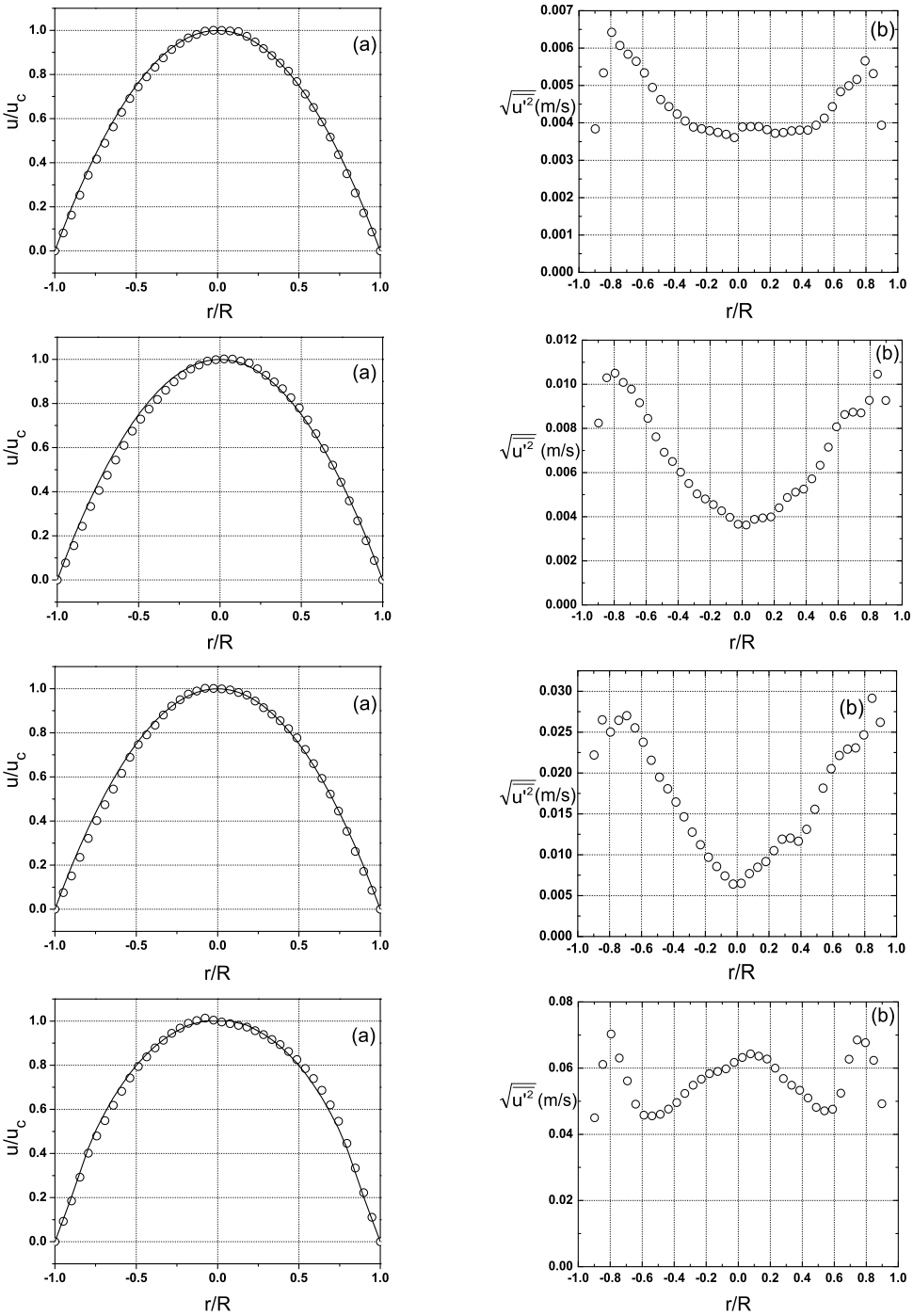

Figure B.29: (a) The time averaged velocity and (b) Local RMS velocity profiles for 65% Glycerin. From top to bottom; Re_G=342, Re_G=633, Re_G=1860 and Re_G=2573

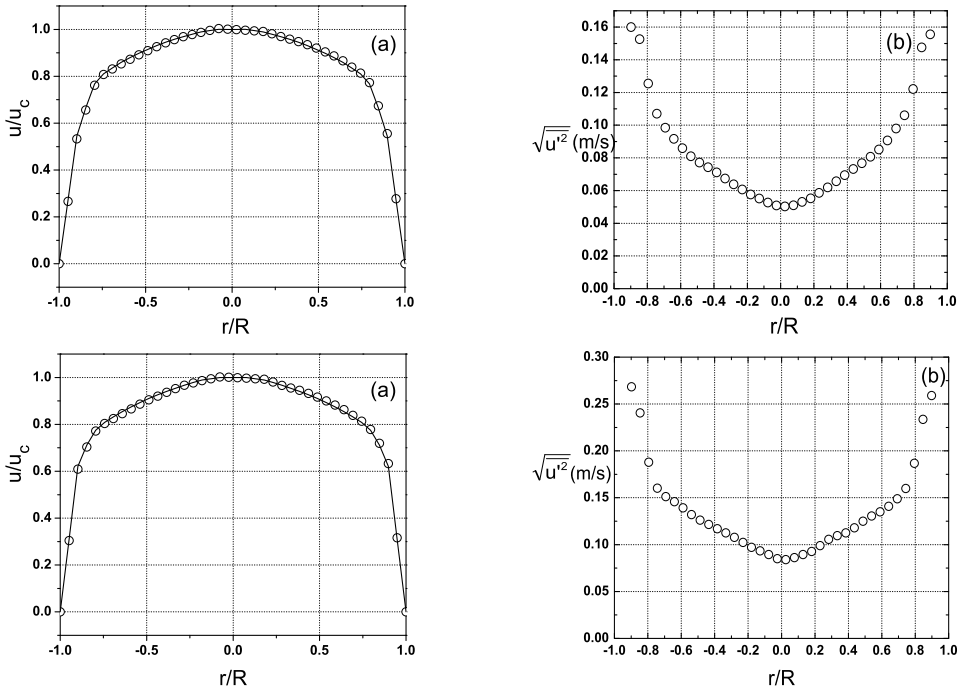

Figure B.30: (a) The time averaged velocity and (b) Local RMS velocity profiles for 65% Glycerin. From top to bottom; Re_G=5393 and Re_G=10531

Table B.29: Velocity readings for 65% Glycerin in Table B.28

	U_b=0.0564, ΔP=0.07		U_b=0.1045, ΔP=0.13		U_b=0.2943, ΔP=0.37		U_b=0.3894, ΔP=0.54	
r/R	$\overline{u}$	u'	$\overline{u}$	u'	$\overline{u}$	u'	$\overline{u}$	u'
-1	0	–	0	–	0	–	0	–
-0.94872	0.00949	–	0.01684	–	0.04601	–	0.06736	–
-0.89744	0.01897	0.00384	0.03368	0.00824	0.09203	0.0222	0.13472	0.04498
-0.84615	0.02943	0.00534	0.05272	0.0103	0.14375	0.0265	0.21278	0.06112
-0.79487	0.04001	0.00642	0.07203	0.01051	0.19617	0.02501	0.29214	0.07029
-0.74359	0.04847	0.00607	0.08787	0.01008	0.24513	0.02645	0.34886	0.06306
-0.69231	0.05687	0.00584	0.10273	0.00978	0.28932	0.02701	0.3993	0.05615
-0.64103	0.06545	0.00565	0.11758	0.00916	0.33211	0.02553	0.44972	0.0491
-0.58974	0.07318	0.00534	0.1319	0.00845	0.37593	0.02376	0.49593	0.0458
-0.53846	0.08039	0.00495	0.14589	0.00762	0.42038	0.02156	0.53957	0.04556
-0.48718	0.0866	0.00462	0.15774	0.00692	0.45559	0.01948	0.57734	0.04605
-0.4359	0.09187	0.00444	0.16756	0.0065	0.48206	0.01807	0.60955	0.04762
-0.38462	0.09698	0.00424	0.17705	0.00602	0.50911	0.01645	0.63895	0.04959
-0.33333	0.10187	0.00405	0.18607	0.00551	0.537	0.01464	0.66423	0.05234
-0.28205	0.10624	0.00389	0.19433	0.00504	0.5618	0.01277	0.68708	0.05484
-0.23077	0.10942	0.00384	0.20083	0.00481	0.57931	0.01123	0.70415	0.05669

Continued on next page

Table B.29 – continued from previous page

r/R	$\overline{u}$	u'	$\overline{u}$	u'	$\overline{u}$	u'	$\overline{u}$	u'
-0.17949	0.11235	0.00379	0.20684	0.00455	0.59508	0.00969	0.71976	0.05833
-0.12821	0.1142	0.00375	0.21078	0.00427	0.60343	0.00857	0.72906	0.05899
-0.07692	0.11594	0.00369	0.21452	0.00397	0.61106	0.00742	0.73706	0.05976
-0.02564	0.1164	0.00361	0.21597	0.00366	0.61062	0.00641	0.73035	0.06173
0.02564	0.1163	0.00389	0.21667	0.00363	0.6091	0.0065	0.72431	0.06324
0.07692	0.11602	0.0039	0.21661	0.00388	0.60651	0.0077	0.71894	0.06431
0.12821	0.11574	0.0039	0.21473	0.00394	0.59941	0.00847	0.71323	0.06361
0.17949	0.11316	0.00382	0.21269	0.00399	0.59192	0.00917	0.70749	0.06276
0.23077	0.11022	0.00372	0.20711	0.0044	0.57569	0.01051	0.69575	0.05998
0.28205	0.10674	0.00374	0.2007	0.00487	0.55743	0.01191	0.68261	0.05682
0.33333	0.10308	0.00379	0.1941	0.00511	0.53943	0.01203	0.6668	0.05483
0.38462	0.09906	0.00381	0.18741	0.00525	0.52155	0.01165	0.64987	0.05331
0.4359	0.09484	0.00381	0.17872	0.00572	0.49918	0.01312	0.62709	0.05098
0.48718	0.08934	0.00394	0.16866	0.00633	0.47376	0.01557	0.60034	0.04814
0.53846	0.08274	0.00413	0.1569	0.00715	0.44166	0.01814	0.57065	0.04708
0.58974	0.0757	0.00443	0.14333	0.00807	0.40253	0.02051	0.53788	0.04759
0.64103	0.06806	0.00484	0.12878	0.00863	0.36179	0.02214	0.49932	0.05243
0.69231	0.06001	0.00499	0.1126	0.00874	0.31844	0.02292	0.45127	0.06268
0.74359	0.05078	0.00516	0.09595	0.0087	0.27167	0.02307	0.39717	0.06851

Continued on next page

Table B.29 – continued from previous page

r/R	$\overline{u}$	u'	$\overline{u}$	u'	$\overline{u}$	u'	$\overline{u}$	u'
0.79487	0.04073	0.00566	0.07765	0.00927	0.21578	0.02466	0.32439	0.06768
0.84615	0.03059	0.00532	0.05802	0.01046	0.16018	0.02915	0.24294	0.06235
0.89744	0.02011	0.00394	0.03842	0.00927	0.10493	0.02619	0.16157	0.04922
0.94872	0.01006	–	0.01921	–	0.05246	–	0.08078	–
1	0	–	0	–	0	–	0	–

Table B.30: Velocity readings for 65% Glycerin in Table B.28

	U_b=0.7791, ΔP=2.55		U_b=1.4489, ΔP=7.42	
r/R	$\overline{u}$	u'	$\overline{u}$	u'
-1	0	–	0	–
-0.94872	0.28528	–	0.59561	–
-0.89744	0.57056	0.16007	1.19121	0.26843
-0.84615	0.70252	0.15259	1.37508	0.24057
-0.79487	0.81589	0.12554	1.50904	0.18795
-0.74359	0.86457	0.10708	1.57161	0.16021
-0.69231	0.88993	0.09849	1.61276	0.15128
-0.64103	0.91327	0.09162	1.65327	0.1458
-0.58974	0.93446	0.08596	1.69325	0.13934
-0.53846	0.95433	0.08101	1.73291	0.1321
-0.48718	0.97348	0.07713	1.76854	0.12616
-0.4359	0.99193	0.07434	1.80037	0.12162
-0.38462	1.00896	0.07113	1.83192	0.11707
-0.33333	1.0239	0.0674	1.86303	0.11264
-0.28205	1.03733	0.06379	1.89072	0.10781
-0.23077	1.0472	0.06068	1.91032	0.10239

Continued on next page

Table B.30 – continued from previous page

r/R	$\overline{u}$	u'	$\overline{u}$	u'
-0.17949	1.05696	0.05763	1.92924	0.0972
-0.12821	1.06626	0.05514	1.94532	0.09343
-0.07692	1.07458	0.05266	1.95988	0.08954
-0.02564	1.07186	0.05088	1.95723	0.08511
0.02564	1.06927	0.05035	1.95381	0.08401
0.07692	1.0668	0.05104	1.94964	0.08622
0.12821	1.06403	0.05311	1.94498	0.08942
0.17949	1.06123	0.05529	1.94029	0.09268
0.23077	1.05051	0.05856	1.91725	0.09892
0.28205	1.03794	0.062	1.88992	0.10565
0.33333	1.02627	0.06572	1.86807	0.10968
0.38462	1.01498	0.0695	1.84852	0.11256
0.4359	1.00104	0.07318	1.82238	0.11798
0.48718	0.98529	0.07673	1.79174	0.12494
0.53846	0.96813	0.08074	1.75959	0.13065
0.58974	0.94949	0.08517	1.72587	0.13508
0.64103	0.92713	0.09072	1.68715	0.1409
0.69231	0.89867	0.09799	1.64023	0.1489
0.74359	0.87087	0.1061	1.59077	0.15988

Continued on next page

Table B.30 – continued from previous page

r/R	$\overline{u}$	u'	$\overline{u}$	u'
0.79487	0.82757	0.1221	1.52172	0.18675
0.84615	0.7215	0.14758	1.40664	0.23362
0.89744	0.59475	0.15555	1.23713	0.25911
0.94872	0.29738	–	0.61856	–
1	0	–	0	–

Appendix C

Codes

Listing C.1: Matlab program that does the image processing analysis for real time thresholding.

```
clf
datadir='C:\DocumentsandSettings\bulent\MyDocuments\
 Experiments\CCDExps\Dec06.07\';
imagini=dir([datadir,'*.jpg']); nrofimages=length(
 imagini);
nrofimages=5680;

level=0.92;
%% to crop images:
left=1;right=504; up=203;down=67;
dhy=(right-left+1)*63.5/(up-down);% dhy=pipe length in
  mm

allqx=zeros(nrofimages,1);allqy=allqx;
% equalize the mean image
meanimage=imread([datadir,strcat('meanimage.jpg')]);
meanimage=meanimage(1:248,1:504);
%meanimage = adapthisteq(meanimage);
jj=0; xtplot=zeros(504,size(meanimage(down:up,left:
 right),1));
xtplot1=zeros(size(meanimage(down:up,left:right),1)
 ,504);
```

```
18 xtplot2=zeros(size(meanimage(down:up,left:right),1)
   ,504);
19 fin=5199;%first image minus 1
20 times=[1:1:nrofimages-fin]*1000*1/400;times=times-
   times(1);%millisecond
21 for i=5200:1:nrofimages
22     a=imread([datadir,strcat('image','    ',num2str(i)
       ,'.jpg')]);
23     a=a(1:248,1:504);
24     %a= adapthisteq(a);
25     figure(1);
26     subplot(3,3,9);
27     imagesc(a);title('unequalized image');drawnow;
28     a=a(down:up,left:right);
29     data=a/max(a(:));
30     meanimage1=meanimage(down:up,left:right);
31     meanimage1=double(meanimage1);
32     subplot(3,3,1);imagesc(a);colormap bone;
33     text(6,22,['t= ','','',num2str(times(i-fin)),'','
       ms'],'FontSize',10,'Color','w','FontWeight','bold
       ');drawnow
34     title(strcat('IMAGE    ',num2str(i)));%colorbar
35     subplot(3,3,2);imagesc(wiener2(im2bw(a,level)));
       colormap bone;drawnow;%colorbar;
36     subplot(3,3,3);imagesc(double(a)-meanimage1);title
       ('background substracted');drawnow;%colorbar;
37     subplot(3,3,4);
38     title(strcat('IMAGE    ',num2str(i)))
39     %imagesc(medfilt2(im2bw(double(a)-meanimage1,1)))
40     imagesc(imfill(medfilt2(im2bw(double(a)-meanimage1
       -2,1)),'holes'))
41     %imagesc(wiener2(im2bw(double(a)-meanimage1,1)))
42     %pause
```

```
43
44      d1=imfill(medfilt2(im2bw(double(a)-meanimage1-2,1)
         ),'holes');
45      %[qx,qy]=find(d1==1);
46      %allqx(i)=mean(qx);allqy(i)=mean(qy);
47      %subplot(3,3,5);plot(allqy(1:i),allqx(1:i),'-ok');
         hold on;
48
49      %subplot(3,3,6);
50      %plot([1:1:i],allqx(1:i),'->b',[1:1:i],allqy(1:i)
         ,'-<g');drawnow
51      subplot(3,3,7);
52      jj=jj+1;
53      aa=double(a)-meanimage1;
54      xtplot(jj,:)=aa(:,250);
55      imagesc(xtplot);title('xt plot');drawnow;
56      subplot(3,3,8);
57      imagesc(imfill(medfilt2(im2bw(xtplot-2,1)),'holes
         '))
58
59      %figure('Position',[100 100 520 148]);drawnow;
60      %imagesc(a);colormap bone;
61      %axis image;
62      %text(7,18,['t = ','','',num2str(times(i-fin))
         ,'','' ms'],'FontSize',18,'Color','w');drawnow;
63      %set(gca,'Visible','off');
64      %set(gca,'Position',[0 0 1 1]);
65      %figure('Position',[150 150 520 148]);drawnow;
66      %imagesc(d1);colormap bone;
67      %axis image;
68      %set(gca,'Visible','off');
69      %set(gca,'Position',[0 0 1 1]);
70
```

```
71      %figure(2);
72      %xtplot1(:,jj)=aa(:,250);
73      %imagesc(xtplot1);colormap bone;drawnow;
74
75      %figure(3);
76      %imagesc(imfill(medfilt2(im2bw(xtplot1-2,1)),'
          holes'));colormap bone;drawnow;
77
78      %figure(4);
79      %xtplot2(:,jj)=d1(:,250);%subplot(3,3,5);
80      %imagesc(xtplot2);colormap bone;drawnow;
81
82      %d(:,:,jj)=aa(:,:);
83      %subplot(3,3,8);plot(mean(allqy),mean(allqx),'og')
          ;draw
84      %now
85
86      %saveas(gcf,num2str(i),'fig');
87      %close(figure(2));
88      pause
89  end
90  hold on;
91  % subplot(3,3,8);plot(mean(allqy),mean(allqx),'og');
     drawnow
92  t=501; dplot=zeros(186,505); for k=1:jj
93  dplot(:,t:t+494)=d(:,10:504,k); t=t-1;
94  subplot(3,3,6);imagesc(dplot);drawnow;
95  end
96  subplot(3,3,5);imagesc(imfill(medfilt2(im2bw(dplot
     -2,1)),'holes'));
```

Listing C.2: Matlab program that computes the correlation functions and pdfs for the real velocity readings.

```
clf; warning off
%%% declare your constants
nrofbins=200; %% nr of bins in the probability
 distribution function

colors=['-r','-g','-b','-k','-m','-c','y','-r','-g','-
 r','-g','-b','-k','-m','-c','-y','-r','-g',...
     '-r','-g','-b','-k','-m','-c','y','-r','-g','-r
      ','-g','-b','-k','-m','-c','-y','-r','-g',...
     '-r','-g','-b','-k','-m','-c','y','-r','-g','-r
      ','-g','-b','-k','-m','-c','-y','-r','-g',...
     '-r','-g','-b','-k','-m','-c','y','-r','-g','-r
      ','-g','-b','-k','-m','-c','-y','-r','-g',...
     '-r','-g','-b','-k','-m','-c','y','-r','-g','-r
      ','-g','-b','-k','-m','-c','-y','-r','-g',...
     '-r','-g','-b','-k','-m','-c','y','-r','-g','-r
      ','-g','-b','-k','-m','-c','-y','-r','-g',...
     '-r','-g','-b','-k','-m','-c','y','-r','-g','-r
      ','-g','-b','-k','-m','-c','-y','-r','-g'
    ];
datadir='C:\Documents and Settings\bulent\My Documents
 \Experiments\LDVExps\Carbopol\06Dec06\rate1\';%% here
 you should have your time series
resdir=[datadir,'Results\']; mkdir(resdir);
pdfdir=[resdir,'PDFs\']; mkdir(pdfdir);

correlationsdir=[resdir,'CORRELATIONS\']; mkdir(
 correlationsdir);

spectradir=[resdir,'SPECTRA\']; mkdir(spectradir);

```

```
21 structuredir=[resdir,'STRUCTURE\']; mkdir(structuredir
   );
22
23 veldiffdir=[resdir,'VELDIFF\']; mkdir(veldiffdir);
24
25 nroffiles=size(dir([datadir,'p*.txt']),1);
26
27 for ii=1:19
28 filename=['p',num2str(ii),'.txt'] data=load(filename);
29 index=ii;
30
31     time=data(:,1);
32     speed=data(:,2);
33
34     %% calculate the pdf's and save them on the disk
35     [probability,bins]=hist(speed,nrofbins);
36     stat=cat(1,bins,probability);stat=stat';
37     [probabilityScaled,binsScaled]=hist((speed-mean(
        speed))/std(speed),nrofbins);
38     statScaled=cat(1,binsScaled,probabilityScaled);
        statScaled=statScaled';
39     %figure(1)
40     subplot(2,3,1)
41     semilogy(bins-mean(speed),probability/max(
        probability),colors(ii));hold on;drawnow
42     title('PDFs of velocity fluctuations')
43     save([pdfdir,'pdfs',num2str(index),'.txt'],'stat
        ','-ASCII')
44     save([pdfdir,'pdfsScaled',num2str(index),'.txt'],'
        statScaled','-ASCII')
45     %% first interpolate the data on a equispaced
        timegrid
```

```
46    timeinterp=[min(time):0.9*mean(diff(time)):max(time
      )];
47    timestep=mean(diff(timeinterp));
48    speedinterp=interp1(time,speed,timeinterp,'cubic');
49    %%%%%%%%
50    [c,lags] = xcorr(speedinterp-mean(speedinterp),'
      coeff');
51    q=find(c==1);
52    %figure(2);
53    subplot(2,3,2)
54    semilogx(timeinterp,c(q:end),colors(ii));hold on;
      drawnow
55    title('Velocity Autocorrelation function')
56    %pause(2)
57    corrfunction=cat(1,timeinterp,c(q:end));
      corrfunction=corrfunction';
58    save([correlationsdir,'corrfunction',num2str(index)
      ,'.txt'],'corrfunction','-ASCII')
59    % calculate the correlations and save them on the
      disk
60    %StructureFunctions
61    veldif=diff(speedinterp)/(timestep*mean(speedinterp
      ));
62    [m,n]=hist((veldif),200);
63    statgrad=cat(1,n,m);statgrad=statgrad';
64    save([pdfdir,'pdfsGRADIENTS',num2str(index),'.txt
      '],'statgrad','-ASCII')
65    %figure(3);
66    subplot(2,3,3)
67    semilogy(n,m/max(m),colors(index));hold on;drawnow
68    velgrad(ii,1)=ii;
69    velgrad(ii,2)=mean(abs(veldif));
70    %%%%
```

```
71      title('PDFs of velocity gradients')
72      subplot(2,3,4)
73      plot(data(:,1),data(:,2),colors(ii));hold on;
         drawnow
74      title(['timeseries for position number ', num2str(
         index),'  across profile'])
75      disp(['I am working on point with index  ',num2str(
         index)])
76
77  end
78          save([veldiffdir,'VelGradients','.txt'],'velgrad
             ','-ASCII')
79  corrtimes=CorrTimes9May1(correlationsdir); subplot
     (2,3,5);
80  qqq=find(corrtimes(:,3)>0);semilogy(corrtimes(qqq,1)',
     corrtimes(qqq,3)','-o');hold
81  on; plot([1:1:length(velgrad(:,1))],velgrad(:,2),'-ok
     ');
82  title('Velocity Autocorrelation times and Mean
     Gradients')
83
84  function corrtimes=CorrTimes9May1(correlationsdir)
85  corrtimes=zeros(size(dir([correlationsdir,'
     corrfunction*.txt'])),1),3);
86  namescorr=dir([correlationsdir,'corrfunction*.txt']);
87
88  for k=1:1:size(dir([correlationsdir,'corrfunction*.txt
     ']),1)
89          namefile=namescorr(k).name;
90          qq=find(namefile=='.');
91          indexcorr=str2num(namefile(13:qq-1));
92          corrfunc=load([correlationsdir,namefile]);
93          timpi=corrfunc(1:end,1);data=corrfunc(1:end,2);
```

```
94      tau=abs(trapz(timpi,timpi.*(data))/trapz(timpi,abs
        (data)));
95      corrtimes(indexcorr,2)=tau;
96      q=find(data<4*10^(-4)&data>-(4*10^(-4)));
97      corrZeroCross=timpi(min(q))
98       corrtimes(indexcorr,3)= corrZeroCross;
99          corrtimes(indexcorr,1)=indexcorr;
100     disp(['I work on Corr Function',num2str(indexcorr)
        ,'Tau===',num2str(tau),...
101         'and ZeroCross==',num2str(corrZeroCross)])
102 end
103      selector=find(corrtimes(:,1)>0);creal=0;
104      creal=corrtimes(selector,:);
105      corrtimes=creal;
106    save([correlationsdir,'CorrelationTimes','.txt'],'
       creal','-ASCII')
```

Listing C.3: Matlab program that computes the structure functions for the real velocity readings.

```
1  datadir='C:\Documents and Settings\bulent\My
2  Documents\Experiments\LDVExps\Carbopol\04May06\rate7\'
3  structuredir='C:\Documents and Settings\bulent\My
4  Documents\Experiments\LDVExps\Carbopol\04May06\rate7\
    Results\STRUCTURE\'
5  clf;
6  nrofsfunctions=5;
7  color=['-<r','->g','-*b','-ok','-<y','->m','-<r','->g
    ','-*b','-ok','-<y','->m'];
8
9  for index=[12 26 42]
10     filename=['p',num2str(index),'.txt']
11     data=load(filename);
12
```

```
13      ti=data(:,1);
14      datai=data(:,2);
15      %%% select here upper time bounds for the
         structure functions
16      q=find(ti<20); %%% build structure functions for
         time differences smaller than 20 seconds
17      tstructure=ti(q);
18      length=length(datai(q));
19      %%%%
20
21      profil=datai;
22      lengthS=length;
23      results=zeros(lengthS,nrofsfunctions+1);
24      results(:,1)=ti(q)';
25      %figure(3)
26      for pp=1:1:(nrofsfunctions)
27      timestructure=0;
28            structurap=zeros(lengthS,1);
29            for k=1:1:(length-1)
30
31              if mod(k,100)==0,
32              disp(['Directory: ',num2str(index),'I AM
                 WORKING ON THE FUNCTION WITH INDEX    ',
                 num2str(pp),' and ',' k= ',num2str(k)]);
33              end
34              Sp=zeros(lengthS,1);
35              for ii=1:1:(length-k)
36
37              Sp(ii)=abs(profil(ii)-profil(ii+k)).^pp;
38              end
39
40             structurap(k)=mean(Sp(:));
41
```

```
42          end
43          results(:,pp+1)=structurap/(std(datai))^pp;
44          loglog(ti(q),structurap/(std(datai))^pp,color(
            pp));hold on;drawnow
45        end
46        clf;
47        loglog(ti(q),results(:,2:end),'o')
48        ti=ti(q)';
49        save([structuredir,'StructureFunctions',num2str(
          index),'.txt'],'results','-ASCII')
50        save([structuredir,'times',num2str(index),'.txt
          '],'ti','-ASCII')
51  end
```